

**Step decoration and growth
at the vicinal Pt(997) surface**

Martial BLANC

Travail soumis au jury pour l'obtention du titre de
Docteur ès Sciences de l'Ecole Polytechnique
Fédérale de Lausanne

Lausanne, août 1998

Version abrégée

L'objectif de cette thèse est de contribuer à une meilleure compréhension de la croissance sur les surfaces vicinales. La densité élevée de marches présente sur ce type de surface influence drastiquement la croissance. La raison en est un nombre accru d'atomes plus proches voisins qui font de la marche un site préférentiel pour l'adsorption.

La première partie de cette thèse traite de la croissance rangée-par-rangée sur la surface vicinale Pt(997). Ce type de croissance, qui procède par attachement successif de rangées complètes au pied des marches, est un phénomène général observé pour les gaz rares (Xe, Kr) aussi bien que pour les métaux (Ag, Co) au cours de l'étape initiale de la croissance sur Pt(997). La méthode TEAS à incidence rasante s'avère être idéale pour l'observation de ce type de croissance, car elle augmente, dans le signal hélium, la contribution du bord de la marche par rapport à celle de la terrasse, donnant ainsi accès à l'ordre à la marche. La thermodynamique de la croissance rangée-par-rangée de Xe sur Pt(997) a été le sujet d'une étude théorique qui est en bon accord avec les observations expérimentales.

La croissance et la thermodynamique de Kr sur Pt(997) ont été étudiées. Une chaleur latente d'adsorption dans la première monocouche de 210 ± 10 meV, ainsi qu'une chaleur latente d'adsorption dans la phase multicouche de 120 ± 20 meV ont été obtenues pour ce système.

La croissance d'Ag sur Pt(997) a été étudiée de manière approfondie. Le mode de croissance multicouche présente un changement avec la température. Au-dessus de 300 K, la croissance se déroule couche-par-couche jusqu'à la troisième couche et un regroupement des marches ("step bunching") est observé pour des recouvrements supérieurs. Au-dessous de 300 K, la croissance se déroule couche-par-couche au moins jusqu'à la cinquième couche et aucun regroupement des marches n'est observé. Ce changement de mode de croissance est attribué à une barrière de diffusion accrue pour descendre la septième rangée de la couche d'Ag. Cette barrière ne peut pas être franchie à basse température avant que la nucléation n'ait lieu sur la couche supérieure.

Au-dessus de la température d'alliage, un recouvrement d'Ag inférieur à la monocouche forme avec la surface de Pt un alliage confiné à la première monocouche. L'alliage est un processus énergétiquement activé qui a lieu à la marche pour des températures supérieures à 500 ± 20 K. De plus, une observation a montré qu'une rangée d'Ag flotte au bord de la

marche de Pt à des températures bien supérieures à la température d'alliage.

La croissance d'Ag sur Pt(997) et Pt(779) ne montre aucune influence du type de marche sur la croissance, tandis qu'une influence a été trouvée sur la température d'alliage de l'Ag dans la première monocouche de Pt. L'alliage sur Pt(779) a lieu au moins 100 K avant l'alliage sur Pt(997). Cette différence est attribuée à la marche moins compacte présente sur Pt(779).

Des sandwichs formés de deux monocouches d'Ag et de Co ont été étudiés en vue d'obtenir des informations sur l'interaction entre ces différents éléments et le substrat. La monocouche d'Ag retarde la diffusion du Co dans le substrat de Pt vers des températures plus élevées, mais n'est pas capable de stabiliser efficacement la couche de Co.

Finalement, une partie de cette thèse a été consacrée à une amélioration technique: la conception et la construction d'un nouveau spectromètre pour l'analyse en énergie des atomes d'hélium. Il est basé sur les propriétés de diffraction des surfaces vicinales (DAS) et est pressenti pour permettre, dans un proche avenir, l'amélioration de la résolution en énergie au-dessous de la limite de $\sim 1\%$ rencontrée par les spectromètres à Temps De Vol ("TOF"). Le nouveau spectromètre sera monté sur le reste de l'installation expérimentale au cours des prochains mois.

Abstract

The objective of this thesis is to contribute to a better understanding of the epitaxial growth on vicinal surfaces. The large density of steps present on this type of surfaces drastically influences the growth, as the increased number of nearest neighbor atoms make the step a preferential site for adsorption.

The first part of this thesis treats the row-by-row growth on the vicinal Pt(997) surface. This type of growth, proceeding by sequential attachment of complete rows at the steps, is a general phenomenon observed for rare gases (Xe, Kr) as well as for metals (Ag, Co) during the initial stage of growth on Pt(997). Grazing incidence TEAS is shown to be well suited for monitoring this type of growth, as it enhances the contribution, in the He intensity, of the step edge with respect to the terrace, giving access to the order at the step. The thermodynamics of the row-by-row growth of Xe on Pt(997) has been studied theoretically and is in good agreement with the experimental observations.

Growth and thermodynamics of Kr on Pt(997) have been studied. A heat of adsorption in the first monolayer of 210 ± 10 meV, and a heat of adsorption in the multilayer of 120 ± 20 meV are obtained for this system.

Ag growth on Pt(997) has been extensively studied. The multilayer growth mode exhibits a change with temperature. Above 300 K, the growth takes place layer-by-layer until the third layer and a step bunching is observed for a larger number of layers. Below 300 K, the growth takes place layer-by-layer at least until five layers and no step bunching is observed. This growth change is attributed to an increased step edge barrier to descend the seventh row of the Ag adlayer, which cannot be overcome at low temperature before nucleation takes place on top of the layer.

Above the alloying temperature, a submonolayer coverage of Ag forms with the Pt surface an alloy confined to the first layer. The alloying is an energy activated process which takes place at the step above 500 ± 20 K. Moreover, evidence has been found that a row floats at the Pt step edge at temperatures well above the alloying temperature.

Ag growth on the Pt(997) and Pt(779) shows no influence of the step type on the growth, whereas an influence on the alloying temperature of Ag in the Pt first layer has been found. Alloying on Pt(779) takes place at least 100 K before the alloying on Pt(997). This difference is attributed to the less densely packed step on Pt(779).

Sandwiches of two monolayers of Ag and Co have been investigated in order to obtain information on the interaction between these elements and the substrate. The Ag monolayer shifts the Co bulk diffusion into the Pt substrate to higher temperature, but is not able to stabilize efficiently the Co layer.

Finally, a part of the thesis has been devoted to a technical improvement: the concept and the construction of a new spectrometer for the energy analysis of the He atoms. It is based on the diffractive properties of the vicinal surfaces and is expected to allow in a near future the improvement of the energy resolution below the limit of $\sim 1\%$ encountered in TOF spectrometers. The new spectrometer will be mounted on the rest of the experimental setup in the next months.

Contents

Version abrégée	i
Abstract	iii
1 Introduction	7
2 Helium scattering: principles and applications	9
2.1 Introduction	9
2.2 Principles of He scattering	10
2.3 Applications	12
2.3.1 Structure determination	12
2.3.2 Growth mode characterization	13
2.3.3 Phase transitions	17
2.3.4 Surface dynamics studies	18
3 Experimental	19
3.1 Principle of the surface scattering spectrometer	19
3.2 The He scattering instrument	21
3.2.1 General Concept	21
3.2.2 The source	24
3.2.3 The scattering chamber	24
3.2.4 The analysis-detection unit	24
3.2.5 Working modes	25
3.3 Substrates	26
3.3.1 Introduction	26
3.3.2 Diffraction pattern of the (997) and (779) surfaces	28
3.3.3 Check of the correct miscut of the vicinal samples: 997 or 779?	33
4 Row-by-row growth at vicinal surfaces	37
4.1 Introduction	37

4.2	Experimental	38
4.3	Results	38
4.3.1	Row-by-row growth	38
4.3.2	Thermodynamics	41
4.4	Summary	45
5	Step sensitivity of grazing incidence He scattering	47
5.1	Introduction	47
5.2	Experimental	49
5.3	Results	49
5.3.1	Ag growth on Pt(997)	49
5.3.2	TEAS step-terrace sensitivity	51
5.3.3	Difference between homo- and heteroepitaxy	53
5.4	Summary	54
6	Xe adsorption on Pt(997): theory and experiment	55
6.1	Introduction	55
6.2	Experiment	56
6.3	Interaction potentials	61
6.3.1	Adsorbate-substrate interactions	61
6.3.2	Adsorbate-adsorbate interactions	63
6.4	Equilibrium configurations for xenon	64
6.4.1	General	64
6.4.2	Results	64
6.5	Structure growth at finite temperature	67
6.5.1	Ideal lattice gas model	68
6.5.2	Mean field Hamiltonian Ising model	69
6.5.3	Numerical results	70
6.6	Discussion	73
6.7	Summary	77
7	Kr adsorption on Pt(997): experiment	79
7.1	Introduction	79
7.2	Experimental	80
7.3	Results	80
7.3.1	Growth mode	80
7.3.2	Structure of the Kr monolayer	82
7.3.3	Thermodynamics	83
7.4	Discussion	86
7.5	Summary	86

8 Ag growth on Pt(997)	89
8.1 Introduction	89
8.2 Theory: Diffraction pattern of an adsorbate covered Pt(997) surface	90
8.3 Experimental	92
8.4 Results	92
8.4.1 Ag growth on Pt(997)	92
8.4.2 Alloying and demixing processes	104
8.5 Summary	108
9 Silver-Cobalt metal sandwiches on Pt(997)	111
9.1 Introduction	111
9.2 Experimental	112
9.3 Results and discussion	113
9.3.1 Reference systems: 1 ML Co on Pt(997) and 1 ML Ag on Pt(997)	113
9.3.2 Multilayer systems	115
9.4 Summary	120
10 Design of a new Diffractive Analysis Spectrometer (DAS)	121
10.1 Introduction	121
10.2 New experimental setup	121
10.3 Operation of the new DAS spectrometer	127
10.3.1 Energy analysis	127
10.3.2 Energy resolution	129
10.3.3 Energy calibration	135
10.4 Summary	136
11 Outlook	137
Appendix A	139
Appendix B	143
Appendix C	145
References	149

Parts of this thesis are based on the following articles:

- Chapter 4 V. Marsico, M. Blanc, K. Kuhnke, and K.Kern,
Phys. Rev. Lett. **78**, 94 (1997).
- Chapter 5 M. Blanc, K. Kuhnke, V. Marsico, and K. Kern,
Surf. Sci., in press.
- Chapter 6 V. Pouthier, C. Ramseyer, C. Girardet, K. Kuhnke, V. Marsico,
M. Blanc, R. Schuster, and K. Kern, Phys. Rev. B **56**, 4211 (1997).
- Chapter 7 M. Blanc, V. Marsico, P. Gambardella, K. Kuhnke,
and K. Kern, in prep.

Chapter 1

Introduction

Surfaces are a fundamental part of matter. Although they represent a negligible amount of the global mass of an object (except for small clusters), surfaces play a central role in many phenomena. In particular, the surface morphology has a major technological importance, which finds an actual illustration in the semiconductor industry, where the performance of devices is crucially linked to the fabrication of flat and sharp interfaces. In recent years, major efforts have been made in surface science to understand and control the morphology of structures on the nanometer scale. Of particular interest is the tailoring of low-dimensional structures (2D and 1D) having desired shapes on the atomic scale. The properties of such structures are of interest in fundamental research related for example to the magnetism of low-dimensional matter [1, 2].

Two different approaches can be used to create nanostructures. The first approach is based on active fabrication. The probably most impressive technique is the manipulation of single atoms with scanning-probe methods, where desired structures are assembled atom by atom [3, 4]. The problem of this technique is the virtual impossibility of covering macroscopic surfaces with the desired structure. Electron-beam lithography is an active technique which allows to overcome this problem with, however, a worse resolution. The second approach to fabricate nanostructures is by self-organization which arises *e.g.* from kinetic limitations during growth [5]. The kinetic limitations may be a property of the perfect surface, as in the case of Cu on Pd(110) [6], or may be due to the presence of defects at the surface. For example, the domain-wall network exhibited by the second Ag layer on Pt(111) can be used as a template to grow islands with a narrow size distribution [7].

Among the different types of defects at surfaces, steps are very efficient nucleation centers playing a crucial role in the growth of epitaxial systems [8]. The reason is an increased number of nearest neighbor atoms at the step, which generally increases the binding energy for an adsorbate. A better understanding of the processes governing the growth at steps is thus necessary in order to improve the growth control in many cases.

The purpose of this thesis is to study in detail the effect of the step on the growth

for physisorbed and chemisorbed systems. The substrates used for these studies, which present a large density of regularly spaced monatomic steps, are the vicinal Pt(997) and Pt(779) surfaces. The step order allows growth investigations by means of an averaging method like Thermal Energy Helium Atom Scattering (TEAS), which is the central method in this work. The principles and main applications of this method for surface studies are presented in chapter 2, and the TEAS apparatus used during this work is described in chapter 3.

The second part of the thesis focuses on the sequential row growth (also called row-by-row growth) which occurs for all the studied adsorbates during the initial stage of growth at the vicinal platinum (997) surface, when their mobility is sufficient. The occurrence of this growth mode and its generality is the subject of chapter 4, the importance of grazing incidence for the observation of this type of growth is treated in chapter 5, and the thermodynamics of the row formation in the case of Xe is studied from a theoretical point of view and then compared to the experimental observations in chapter 6.

In a third part, growth on the Pt(997) surface is treated in a larger coverage range. A thermodynamic and morphologic study of the Kr/Pt(997) system is presented in chapter 7. The growth and alloying of Ag on the Pt(997) and Pt(779) surfaces is the subject of chapter 8. Finally, we report on the temperature dependence of layered Ag and Co structures on Pt(997) in chapter 9.

This thesis ends with a technical part (chapter 10), which treats the concept and the realization of a He atom energy spectrometer based on Diffractive Analysis Spectrometry (DAS), which shall provide a better energy resolution than usual Time Of Flight (TOF) spectrometers. The mounting of this spectrometer will allow in a near future the study of inelastic processes.

Chapter 2

Helium scattering: principles and applications

2.1 Introduction

The investigation methods used in surface physics [9] can be divided into two main families: The direct space and reciprocal space probes. The first family most importantly contains the STM (Scanning Tunneling Microscopy) [10] and AFM (Atomic Force Microscopy) [11] methods. They provide a direct image of a very small area of the surface (0.01 to $1 \mu\text{m}^2$) with atomic resolution ($0.1 \dots 0.01 \text{ \AA}$). The image is generally straightforward to interpret, even if problems may occur. The contrast is indeed a combination of different contributions (topography and electronic density), which are sometimes difficult to separate [12–14]. Other less common direct probes exist, like the FIM (Field Ion Microscopy) [15], that allows a direct monitoring of adatom diffusion on very particular substrates (the sample must be a tip) or the ion scattering techniques [9], which take advantage of the shadow cone cast by a surface atom onto its neighbors to determine the surface structure. The direct methods give information on a microscopic part of a surface and the question of its global properties can only be answered by recording many measurements, in order to obtain a good statistics.

The second family of methods probes the reciprocal space of the surface. These methods use the wave properties of a particle beam, that is diffracted by the surface [9]. The diffracted beams contain the information on the reciprocal space and thus the periodic structure of the surface. The analysis of the inelastically scattered particles provides information on the collective excitations on the surface (phonons, plasmons, excitons, ...). Many particles can be used as probes: electrons, neutrons, photons and atoms. Their energy and wavelength determine their sensitivity for the surface and the kind of inelastic process they can probe. The information obtained by these methods is averaged over a macroscopic region of the surface (depending on the beam size). These methods are

Figure 2.1: He-scattering: scheme of principle.

A wealth of information on the surface can be extracted from the angular distribution as well as from the energy distribution of the scattered beams. The surface structure, the growth mode in an adsorption experiment, phase transitions and surface dynamics are accessible by TEAS. Each of these applications will be treated at least once in the present work. Therefore, they will be introduced in more detail in section 2.3.

TEAS is exclusively sensitive to the topmost atomic layer of the surface. The nature of the interaction taking place between a He atom and the surface is responsible for this particular sensitivity. The electronic cloud of the incoming He atom interacts with the electronic density of the surface. This gives rise to two opposing contributions to the total

potential felt by the He atom: a short-range repulsive potential originating from Pauli's exclusion principle and a much weaker long-range attractive potential due to Van-der-Waals forces [16]. The global effect is dominated by the repulsive part of the potential and leads to the reflection of the He atom about 3–4 Å above the surface atom cores (see figure 2.2). There is thus no penetration and an exclusive surface sensitivity.

The discrete atomic structure of the surface produces periodic modulations of the potential, the so-called surface corrugation. The corrugation is damped with the distance from the surface due to the delocalization of the electrons far from the core levels. A He atom, therefore, only feels a small corrugation of the order of 0.01 Å for a metallic surface [18].

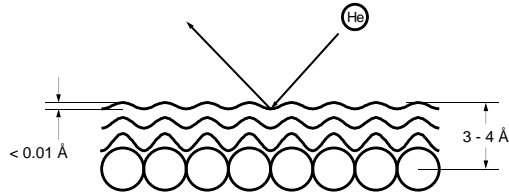


Figure 2.2: Helium atom reflected by the electronic density of the surface. The classical turning point is about 3–4 Å above the surface atoms.

TEAS is a soft surface probe as the energy of the atoms are in the range 10 to 100 meV. These energies are sufficiently small to avoid surface damage. They do not induce desorption even for weakly bound systems like physisorbed rare gases (*e.g.* adsorption energy of Xe on Pt(111) = 277 meV [19]). The range of energies and associated wavelengths accessible to He atoms is shown in figure 2.3 in comparison to electrons, photons and neutrons. The energy–wavelength range of He atoms is well suited for surface physics:

- the wavelength around 1 Å is of the order of the interatomic distances, which allows surface structure studies.
- the wavelength and energy range matches the surface phonon range (dashed area). In addition, there is no need to change the He beam energy to obtain both kinds of information.

Figure 2.3: Energy-wavelength diagram for the typical probe particles in reciprocal space methods: electrons, photons, neutrons and helium. The dashed square area indicates the region of typical reciprocal length scales and energies important in surface phenomena.

2.3 Applications

2.3.1 Structure determination

TEAS is very efficient for surface structure determination [18]. At low temperature, the major part of the He beam is scattered elastically by the periodic potential of a crystalline surface. The matter waves associated with the He atoms interfere afterwards and give rise to the diffraction pattern. This pattern is to some degree the Fourier transform of the direct space, i.e. the image of the surface in reciprocal space. From an angular resolved diffraction pattern, one can extract the periodicity of the surface lattice.

Figure 2.4 shows an example of structure determination extracted from [20]. The Ni(110) surface is represented according to a hard-sphere model in figure 2.4 a, while the corresponding reciprocal lattice is sketched in figure 2.4 b. The measured He diffraction pattern in the [110] direction is given in figure 2.4 c. It corresponds to a cut through the reciprocal lattice intercepting the specular (00) reflection and the two diffraction peaks (01) and (0 $\bar{1}$). From the angular distance between (00) and the diffraction peaks, one can find the reciprocal lattice vectors \mathbf{b}_1 and \mathbf{b}_2 and then the real lattice vectors \mathbf{a}_1 and \mathbf{a}_2 .

The size of a periodic structure that can be resolved by TEAS is not arbitrarily large. In a real instrument characterized by finite beam size and wavelength distribution, a maximum size of the surface region exists, over which the scattered beams interfere coherently and give rise to diffraction. This length on the surface is called the transfer width [21]. If the periodicity of a structure is larger than the transfer width, the beams coming from each cell of the structure add their intensity incoherently and no corresponding diffrac-

Figure 2.4: a) Hard-sphere model of the Ni(110) surface. b) Reciprocal lattice corresponding to a). c) He diffraction pattern in the [110] direction for clean Ni(110).

tion peak occurs. For usual TEAS instruments, the transfer width is of the order of 300-1000 Å.

2.3.2 Growth mode characterization

The intensity in a diffraction peak is a function of different parameters. In particular, it depends on the surface morphology. During an adsorption experiment, the addition of supplementary atoms may change this morphology. Monitoring the intensity of a diffraction peak during the deposition gives thus information on the adlayer growth [22–24].

The high sensitivity of TEAS for growth mode characterization comes mainly from the large cross-section of surface defects (step, kink, adatom, vacancy, . . .) for diffuse scattering [17]. The local perturbation of the smooth periodic potential induced by a defect deflects the He atoms away from the diffraction peaks of the perfect surface. This induces a decrease in the diffraction peaks and an increase of the background He intensity in all directions of space. In figure 2.5, the case of a single adatom on a flat substrate is

Figure 2.5: Diffuse scattering from a single adatom on a flat surface taken from [17]. The solid half-circle represents the range of the repulsive potential of the adatom and the dashed half-circle represents the range of the attractive potential.

Due to the long-range attractive potential (dashed half-circle), the extension of the interaction region is much larger than the atomic size of the defect and is typically of the order of 100\AA^2 [17]. This latter point explains the large sensitivity of TEAS for monitoring defects.

The defect density variation during growth is characteristic of the growth mode and allows its identification. As an example, we will discuss the He signal behavior during the three principal growth modes in epitaxy on flat substrates [25]. The growth modes are presented in figure 2.6.

- a) 2D-growth or layer-by-layer growth or Frank-van der Merwe growth
- b) 3D-growth or Volmer-Weber growth
- c) Stranski-Krastanov growth

In the two-dimensional growth mode, the defect (in this case the step) density varies periodically during the multilayer growth. It is minimal for complete layers and maximal for half layers, and varies monotonically between these coverages. Accordingly, the He

Figure 2.6: The three principal growth modes on flat substrates (see text) and corresponding He signal for ideal: A) 2D-growth, B) 3D-growth and C) Stranski-Krastanov growth. Inset on the right side: example of He signal behavior during a non-ideal 2D-growth.

intensity exhibits oscillations, successively reaching maxima for full layers and minima for half-layers, as shown in figure 2.6 A.

In the case of three-dimensional growth, on the other hand, the defect density increases monotonically during the growth, and the He intensity exhibits an exponential decay (see figure 2.6 B).

During a Stranski-Krastanov growth mode, the growth begins with a 2D-growth and from a critical coverage continues in a 3D-fashion. The He intensity oscillates thus in a first time and decreases monotonically after the onset of the 3D-growth as shown in figure 2.6 C. This case is intermediate between 2D-growth and 3D-growth.

The above discussed growth modes are ideal, which rarely occurs in reality, and the measured He intensities generally exhibit behaviors different from the ones sketched in figure 2.6 A to C. In particular, the He signal often exhibits damped oscillations as shown in the inset of figure 2.6. This behavior may be observed in the case of a non ideal 2D-growth, during which the defect density increases with the increasing number of layers. The damping of the oscillation maxima may also originate from an increasing Debye-Waller factor (see chapter 4) or from flux inhomogeneities as observed for Pt homoepitaxy on Pt(111) [26].

The defect density variation is, however, not the only possible reason for intensity

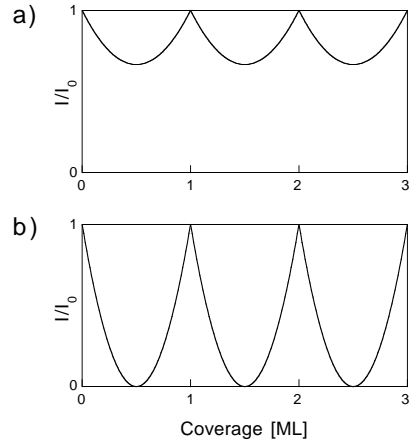


Figure 2.7: Specularly reflected He intensity during a 2D-growth on a flat substrate in: (a) in-phase and (b) anti-phase scattering geometry.

variations during growth. The interference changes, for example resulting from an increase of the number of different levels on the surface or due to deposition of a different element, can also produce intensity variations. Let us look more closely at the case of the ideal 2D-growth mode. During the growth of a layer, two regions with different height are present at the surface. By varying the scattering geometry, one can find two limiting cases: the interference between these two levels can be constructive (in-phase condition), or destructive (anti-phase condition) [17]. These conditions are determined by the path difference between partial He beams coming from adjacent levels. The interference is constructive if the path difference is an integer multiple of the He wavelength and destructive if it is equal to an integer multiple plus half the wavelength. During growth, the amount of material present in the upper level increases monotonically. If the scattering condition is in-phase, the relative population of the different levels does not play a role in the intensity, as all the reflected partial beams from the surface are interfering in-phase. The He intensity variations are then only due to defect density variations (figure 2.7 a). However, if the scattering condition is in anti-phase, the partial beams coming from the different levels interfere destructively. The destruction, again, is minimal (in fact no destructive interference occurs) for a full layer and reaches a maximum for half a monolayer (cf. figure 2.7 b). At this coverage, the intensity is even completely extinct. The interference effect adds thus to the effect of the defect density.

The interpretation is, however, slightly more complicated when the substrate is not flat or in case of heteroepitaxy. Shifts in the extrema positions may occur, but the oscillations in a 2D-growth are still observed. This will be discussed in detail in chapter 8.

2.3.3 Phase transitions

Phase transitions encountered at surfaces are often accompanied by structural modifications. This is the case for the commensurate-incommensurate transitions of solid rare gas adlayers (*e.g.* 1ML Xe/Pt(111) [27]) or the surface reconstruction (*e.g.* W(100) [28]). In the case of the roughening transition [29], the density of steps or kinks (*i.e.* defects) suddenly increases at the transition temperature. TEAS is thus well suited to study these phase transitions, as the diffracted He intensity is very sensitive to surface morphology and order.

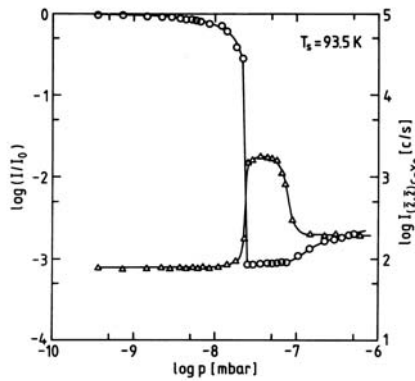


Figure 2.8: Adsorption isotherm of Xe on Pt(111) from [19]. The circles (\circ) give the specularly reflected intensity and the triangles (Δ) give the diffracted intensity in the commensurable $(\bar{2}, \bar{2})_{Xe}$ peak, as a function of Xe-pressure.

As an example, let us consider the behavior of the specularly reflected He intensity during isothermal adsorption of Xe on the Pt(111) surface extracted from [19]. The normalized He intensity is a function of the Xe pressure in the chamber (open circles in figure 2.8). For low enough pressures, the intensity decreases slightly with increasing pressure. The phase present on the surface is a 2D-gas phase. Then, the intensity drops suddenly. This corresponds to the first order transition from a 2D-gas phase to a 2D-

solid phase. The transition is also observable in other diffraction peaks. This is shown for the $(\bar{2}, \bar{2})$ peak of the commensurate Xe solid phase (open triangles), which appears after the transition. Another intensity change for still higher Xe pressures is related to a commensurate-incommensurate phase transition. From a series of such measurements at different temperatures, it is possible to construct the (p,T) phase diagram of the system. This will for example be done in chapter 7 for the Kr/Pt(997) system.

2.3.4 Surface dynamics studies

As mentioned in section 2.1, the energy-wavelength range available by TEAS is adequate for studying surface phonons [30]. To measure a phonon dispersion curve $\hbar\omega(\vec{Q})$, where $\hbar\omega$ is the energy of the phonon and \vec{Q} is its wave vector parallel to the surface, the energy of the scattered He atoms has to be analyzed for various scattering geometries, in such a manner to scan all the possible wave vectors \vec{Q} . The intensity is observed only for certain energies reflecting the discrete structure of branches in the phonon dispersion curve. The difference between the measured energies and the energy of the incident beam (E_i) gives then in a straightforward manner the energy of the created or annihilated phonon. For in-plane scattering (i.e. $\omega_i = \omega_f$ in figure 2.1), the relation between $\hbar\omega$ and \vec{Q} is obtained by conservation of energy and of momentum parallel to the surface. It is given by:

$$\hbar\omega = E_i \left[\left(\frac{\sin\theta_i + Q/k_i}{\sin\theta_f} \right)^2 - 1 \right] \quad (2.1)$$

where θ_i is the incidence angle and θ_f is the angle of the outgoing beam with respect to the surface normal. These angles are defined in figure 2.1. The technique of energy analysis in He surface scattering will be treated in the next chapter.

Chapter 3

Experimental

3.1 Principle of the surface scattering spectrometer

All the He surface scattering spectrometers have the same basis structure, which comprises:

- a He nozzle source,
- a sample chamber,
- a detection unit containing optionally an energy analysis unit.

The function of these three groups is easy to describe: the He beam is created in the source, from where it is directed onto the sample; the He atoms scattered by the surface are energy analyzed and detected in the analysis-detection unit. The realization of an instrument is however more complicated.

A supersonic expansion nozzle [31, 32] provides the He beam. Both intensity and monochromaticity are simultaneously enhanced by orders of magnitude with respect to effusive beams.

For detectors, the situation is less favorable [33]. Due to its properties (which in fact constitute its advantage as a soft surface probe), helium is very difficult to detect. Helium is chemically inert and the most effective way to detect it is to ionize it by electron bombardment. A mass selection is then necessary to separate the He ions from the other ionized species. Even working under UHV conditions, the contribution coming from the background pressure in the detector chamber is important. To achieve the selection, a quadrupole mass analyzer (QMA) or a magnetic sector field can be used. Finally, the He ions are detected with a good efficiency by a secondary electron multiplier (channeltron). The weak point of the detection resides in the ionisation process, while the other processes

Figure 3.1: Schematic experimental setup for (a) TOF and (b) DAS spectrometers.

A promising alternative method proposed by Kuhnke and coworkers [38] for energy analysis is the DAS (Diffractive Analysis Spectrometry) method. Its principle is sketched in figure. 3.1 b). Atoms with different wavelengths are separated spatially by diffraction from a vicinal surface, which acts as an echelette diffraction grating. By rotating the analyzer crystal, different wavelengths may be successively selected to enter the detector. One can deduce the absolute selected wavelength from the absolute determination of the incidence and scattering angles (θ_i^a and θ_f^a). The DAS method may allow a substantial improvement of the analyzers intrinsic energy resolution to under 1%, until the limiting factor of the total energy resolution becomes the monochromaticity of the primary beam.

A monochromator working also with a diffraction grating can then be added to improve further the resolution. The DAS method for energy analysis will be discussed in more detail in chapter 10.

3.2 The He scattering instrument

The experimental instrument (shown in side-view in figure 3.2 and in top-view in figure 3.3) used during this work has been designed and built by V.E. Marsico and H. Schief during their PhD thesis [39, 40]. It exhibits two main differences with respect to conventional TEAS instruments:

- the incidence and scattering angles can be varied independently over a wide range, even to very grazing angles. The total scattering angle $\chi = \theta_i + \theta_f$ covers the range of 59° to 181° , where θ_i and θ_f are defined in figure 2.1.
- the energy analysis system is not based on the TOF method, but on DAS spectrometry.

The very large accessible angular range and high angular resolution are major advantages of this instrument. In particular, the possibility to measure the intensity of the direct beam ($\chi = 180^\circ$) allows the determination of absolute surface reflectivities. In addition, it gives the possibility to calibrate absolutely and with a high precision the angular position of the installation. The wide angular range as well as the possibility to change the scattering angle independently from the incidence angle are useful for phonon dispersion measurements. They allow to choose ΔK_{\parallel} and ΔK_z independently. Moreover, the DAS energy analysis method (chapter 10) offers the possibility for constant ΔE and ΔK scans.

In the next section, the general concept of the instrument will be introduced, while details will be given in the following sections.

3.2.1 General Concept

The instrument is a UHV chamber system composed of three principle modules separated by valves able to withstand atmospheric pressure. This allows to vent one module for repairs or modifications while keeping the UHV in the rest of the installation. The modules are linked to each other by means of bellows that follow the relative movements of the modules in such a manner that the beam path is never blocked. The modules are:

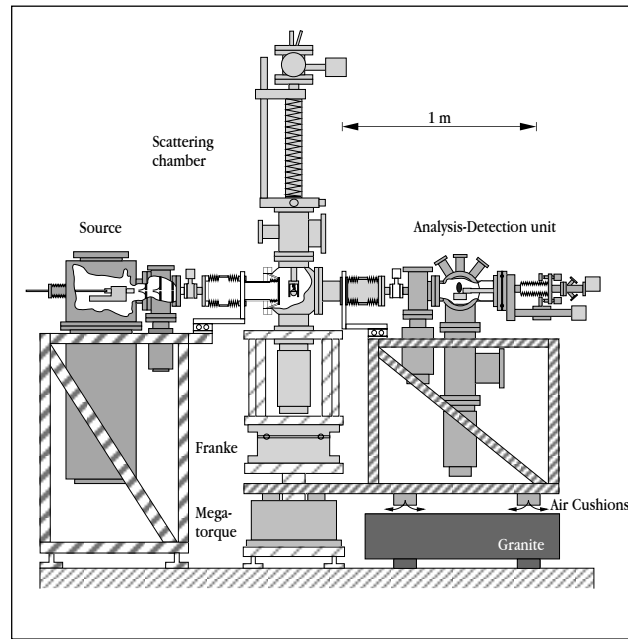


Figure 3.2: side-view of the TEAS experimental instrument.

- the He source (chambers I-III)
- the scattering chamber (IV)
- the analysis-detection unit (chambers V-VIII)

The scattering chamber is the central part of the instrument. It is mounted on a motorized rotary table (Franke) with a movement precision better than 0.01° , whose

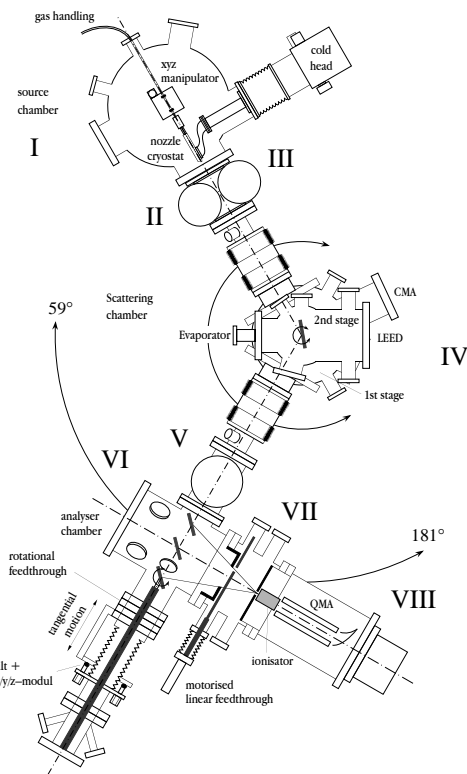


Figure 3.3: top-view of the TEAS experimental instrument.

rotation axis defines the main axis of the instrument. According to the bellows flexibility, the rotation range of the scattering chamber is $\pm 30.5^\circ$. The sample is placed on the main axis by means of a manipulator with six degrees of freedom (x , y , z , tilt, polar, azimuth).

The source is attached on one side of the scattering chamber and is stationary. It produces the monochromatic He beam.

On the other side of the scattering chamber, the analysis-detection unit is mounted on air cushions and glides over a micropolished granite plate. It moves on a circle, the

center of which is the main axis of the instrument, by means of a robotronic rotary table (Megatorque motor). This table is mounted coaxially under the Franke table, and the movement is transmitted to the module via an extremely rigid swivel arm. The absolute angular position of the unit is held by the Megatorque motor with a precision of better than 0.001° . The rotation range of the analysis-detection unit is $\pm 30.5^\circ$.

3.2.2 The source

The source is a standard He nozzle source [34, 41]. The beam is created by supersonic expansion through a nozzle into the vacuum. The nozzle is $10\ \mu\text{m}$ in diameter. It is usually cooled by a helium cold head, and the nozzle temperature can be selected between 50 and 350 K by PID temperature stabilization of a resistance heating. The stagnation pressure inside the nozzle is set to 100-300 bar, depending on the nozzle temperature. The limiting factor is the pumping rate inside the nozzle chamber (I). The lower the temperature of the nozzle, the larger is the load of helium in this chamber, for constant pressure. The chamber surrounding the nozzle is pumped by a diffusion pump with a pumping speed of 6000 l/s coupled to a roots pump with a good pumping efficiency for helium. The nozzle beam is collimated by 2 skimmers (ϕ 0.28 and 0.20 mm) and a diaphragm (ϕ 0.23 mm). Its divergence is determined by this diaphragm and is equal to 0.07° . The divergence can be reduced by introducing a smaller diaphragm mounted on a micrometer screw. The available wavelength range of the beam is 0.5 to 1.5 Å (80–10 meV in terms of energy), and the relative kinetic energy broadening $\Delta E/E$ is typically equal to 1.5%.

After its creation, the beam passes through 2 differential pumping chambers (II and III) and reaches the sample surface in the scattering chamber (IV).

3.2.3 The scattering chamber

The scattering chamber (IV) is equipped with all the standard surface preparation and characterization tools (ion sputter gun, metal evaporators, LEED (Low Energy Electron Diffraction), AES (Auger Electron Spectroscopy)).

3.2.4 The analysis-detection unit

The beams scattered from the surface are then collected in the analysis-detection unit (chambers V to VIII). A differential pumping stage (V) separates the scattering chamber from the chamber containing the analyzer crystal (the so-called “analyzer chamber”) (VI). Its purpose is to decrease the He partial pressure in the detector in order to decrease the background counting rate, and mostly to mutually protect the sample and analyzer crystals against contamination during gas treatments. The analyzer crystal is maintained

in a 5×10^{-9} mbar O_2 + 5×10^{-7} mbar H_2 atmosphere to keep it clean over periods of several weeks [40], which is necessary for an atom optical device.

A precision sample manipulator [40] allows a linear displacement (precision $\pm 5 \mu\text{m}$) as well as a rotation (precision $\pm 0.005^\circ$) of the analyzer crystal (*e.g.* Pt(997)). With these two movements, it is possible to select the wavelength transmitted into the ionisation detector and thus make an energy analysis of the scattered beam (see chapter 10).

Another differential pumping stage (VII) separates the analyzer and detection chambers (VIII) to decrease He background in the detector and thus improve the measurement dynamics. The background counting rate in the detector with the He source off is typically 30 counts/s. This value is five orders of magnitude smaller than the direct He beam counting rate (4 Mcounts/s). The diaphragm between the analyzer chamber and the differential pumping stage is mounted on a motorized linear feedthrough to follow the linear movement of the analyzer crystal, so that the diffracted beam always reaches the detector.

The detection of the He beam is achieved by a standard ionisation detector as for TOF applications [33]. The He beam is ionized by electron bombardment. The ions are then extracted by electrostatic lenses and mass selected by a quadrupole mass analyzer (QMA). They are counted by a secondary electrons multiplier (channeltron). The efficiency of the detector is typically $5 \cdot 10^{-6}$.

3.2.5 Working modes

All movements are synchronized and controlled by computer. An interactive Veetest program, written by V.E. Marsico, allows an easy use of the instrument, releasing the experimentalist from technical concerns. For more details, the reader can refer to [39]. Different types of scans are available with this instrument, the important ones of which are:

- Constant θ_i /variable θ_f scans.
- Constant θ_f /variable θ_i scans.
- Variable θ_i /variable θ_f scans.
- For a fixed geometry, He intensity as a function of time or temperature.
- For a fixed geometry, energy analysis of the scattered beam.

As far as the energy analysis is concerned, it has unfortunately not been possible to perform measurements with the original instrument, because the sample holder of the analyzer crystal suffers from mechanical stability problems. Moreover, only two degrees of freedom of the analyzer crystal are motorized (linear movement z , polar rotation). The

four other degrees of freedom must be adjusted manually. It is therefore impossible to follow exactly the beam during the linear motion over a wide range of wavelength. It hinders reliable quantitative measurements as the movements of the beam on the sample may induce intensity variations due to unavoidable inhomogeneities of the surface quality. For all measurements in this thesis, the analyzer crystal has been replaced by a Pt(111) surface, which offers a good reflectivity for helium (typically 50%). This surface has been placed at a 45° incidence angle in the He beam, deflecting it specularly into the detector. The improvement of this part is the subject of chapter 10.

3.3 Substrates

3.3.1 Introduction

In this thesis, the adlayer growth is studied on two vicinal platinum surfaces, the (997) [42] and the (779) [43] surfaces (see figure 3.4). Both surfaces exhibit regularly spaced terraces separated by monatomic steps of $h = 2.27 \text{ \AA}$ height. The miscut with respect to the (111) direction is slightly different: $\alpha = 6.45^\circ$ for (997) and 7.01° for (779). The average periodicity d is therefore slightly different as well: 20.2 \AA for (997) and 18.6 \AA for (779). These are however minor differences. The main difference is in the step structure, resulting from the different cutting directions. The (997) surface exhibits (111)-microfacet steps, while the (779) surface exhibits (100)-microfacet steps. This difference may have an effect on the adlayer growth and constitutes the reason for the comparative study of these two surfaces (see chapter 8). In figure 3.5, the STM-image of a well prepared Pt(997) surface is shown, which illustrates the almost perfect periodicity of this surface. A statistical study performed by Hahn *et al.* [44] gave as a result a gaussian distribution of the terrace widths with a root mean square deviation of about one atomic row. The almost perfect terrace periodicity is attributed to a repulsive interaction between the steps [44–46]. The similar widths of the He diffraction peaks for both Pt(997) and Pt(779) has shown that the (779) surface is at least as ordered as the Pt(997) surface. The preparation of the surfaces is done according to the usual procedure [44, 47], by repeated Ar ion sputtering cycles at 750 K sample temperature, followed by sample annealing at 900 K. For a freshly cut crystal, annealing is done in an oxygen (10^{-6} mbar) atmosphere to efficiently remove carbon segregating from the bulk.

Figure 3.5: STM-image of a well prepared Pt(997) surface.

Figure 3.6: Schematic diffraction geometry on a Pt(997) surface.

(normal to the macroscopic surface) and ϕ_i and ϕ_f are defined with respect to the [111] direction (normal to the microscopic terraces). These angles are linked by the miscut α : $(\theta_i, \theta_f) = (\phi_i + \alpha, \phi_f - \alpha)$. Note, in figure 3.6, that $\chi = \phi_i + \phi_f = \theta_i + \theta_f$ is the total scattering angle. It will be often referred to this angle in this work.

The diffraction pattern of a Pt(997) surface will be described in terms of the position, intensity and shape of the diffraction peaks.

A) Position of the diffraction peaks

The position of the diffraction peaks is determined by the periodicity of the steps. Their position is given by the one-dimensional Bragg equation [47]:

$$\sin(\theta_f) - \sin(\theta_i) = \frac{n\lambda}{d} \quad (3.1)$$

where λ is the He wavelength and n is the diffraction order. In the case of a vicinal surface, d is equal to $h/\sin\alpha$. d and h are defined in figure 3.4.

Independently of the structure, periodicity and corrugation on the terraces, the intensity in the diffraction pattern is distributed in these peaks. Exceptions may occur in special cases like the selective adsorption [48]. This phenomenon occurs when the

He atoms are diffracted at the surface in such a manner that they are trapped in the attractive potential well of the surface. These bound states are metastable and after a certain time the trapped He atoms undergo another diffraction process and can leave the surface. This gives rise to sharp intensity minima and maxima in the diffraction pattern, corresponding to the channels of trapping and reemission of the He atoms. However, we have not observed such a process on Pt(997).

B) Intensity of the diffraction peaks

The intensity of the diffraction peaks defined by eq. 3.1 is determined by the form factor, i.e. the diffraction pattern of a single terrace. The intensity of a diffraction peak is proportional to the size of the form factor at its position.

It is possible to give an approximation of the form factor (A^2) by considering the terrace as being flat [47]. The form factor is then identical to the diffraction pattern of a single slit, which is expressed in the case of an incident plane wave by:

$$A^2 = \frac{\sin(\Psi/2)^2}{(\Psi/2)^2} \quad (3.2)$$

$$\text{with } \Psi = \frac{2\pi}{\lambda} \tilde{D} (\sin(\phi_i) - \sin(\phi_f)) \quad (3.3)$$

where $\tilde{D} = h \cdot (\frac{1}{\tan\alpha} - \tan\phi_i)$ is the reflecting part of the terrace. This correction has been introduced by Comsa *et al.* [47] and comes from the shadowing effect of the step. The illuminated part is smaller if the incidence angle ϕ_i is more grazing. The width of the form factor is roughly inversely proportional to \tilde{D} and broadens thus with increasing incidence angle.

This expression assumes that there is no corrugation on the terrace. This is reasonable as the metallic (111) surfaces exhibit a very smooth electronic density variation due to electron delocalization. Most of the global He intensity is thus found in this form factor. However, a weak corrugation on the terraces exists and gives rise to other less intense form factors. Their position is given, for in-plane scattering ($\omega_i = \omega_f = 0$ in figure 2.1), by the 1D-Bragg equation:

$$\sin\phi_f - \sin\phi_i = \frac{m\lambda}{a} \quad (3.4)$$

where m is the order of the form factor and a is the periodicity of the corrugation on the terrace parallel to the scattering plane.

The shape of the form factors can still be approximated by the expression 3.2 and their size is determined by the amplitude of the corrugation. The main $m = 0$ form factor is in fact the one determined by the approximation described above assuming no terrace

corrugation. In the following discussions, it will be referred to the $m = 0$ case simply as form factor and the $m \neq 0$ form factors will be explicitly mentioned.

The effectively observed diffraction spectra are fairly well reproduced by the approximation 3.2, as long as the incidence angle is not too grazing. At very grazing incidence angles, a shift of the form factor towards smaller scattering angles occurs as was already observed by Comsa *et al.* [47]. This can be seen by comparing the form factor calculated according to eq. 3.2 and the measured diffraction pattern in figure 3.7. Assuming that the real form factor has the same shape as given by eq. 3.2 and that it is only shifted by an angle σ towards smaller angles, it can be fitted from the integrated intensity of the diffraction peaks. In the case of figure 3.7, for $\phi_i = 66.4^\circ$ a shift of 4.5° is obtained. The shift increases dramatically with the incidence angle. The origin of this shift is a refraction effect of the attractive potential [49] and a bending of the terrace part near to the step [47], as will be discussed below.

The intensity of the diffraction peaks depends on the temperature via the Debye-Waller factor [50, 51]. It takes into account the inelastic scattering of the He atoms by surface phonons. With increasing temperature the phonon excitation is enhanced and the probability for a He atom to interact with a phonon increases. The global effect of these inelastic processes is an intensity decrease in the elastic diffraction channels without change of the peak shape. In the Debye-Waller formalism, the intensity of a diffraction peak is well described [52, 53] by:

$$I(T) = I_0 e^{-2W(T)} \quad (3.5)$$

where $2W(T)$ is the Debye-Waller factor, which can be approximated for usual scattering geometries [54] by:

$$2W = \frac{3T(\hbar^2 \Delta k_z^2 + 8mD)}{Mk_b \Theta_D^2} \quad (3.6)$$

where Δk_z is the perpendicular scattering wave vector transfer. D denotes the effective attractive potential well depth of the surface for He and Θ_D is an effective surface Debye-temperature. M and m are the masses of the surface atom and He-atom respectively.

C) Shape of the diffraction peaks

The shape of the diffraction peaks is determined mainly by the finite terrace width distribution. If the grating was perfectly periodic, the diffraction peaks would be Dirac peaks. However, as the terrace width distribution is finite, the peaks are broadened [40, 55]. They are the more broadened, the more the distance from the terrace specularity ($\phi_i = \phi_f$) is increased. As the same total intensity is smeared out in a broader peak, the peak height is decreased in comparison with the value given by the form factor. Another effect of the

broadening is to shift the position of the peaks which are in the slope of the form factor towards the inner part of it. This effect is however small and the position of the peaks is reasonably well approximated by eq. 3.1.

The width of a diffraction peak n reaches a minimal value when it fulfills a 3D-Bragg condition, i.e. when $\phi_i = \phi_f$. In this condition, all the points of the surface interfere coherently and the width of the diffraction peak is equal to the width of the direct beam if we neglect the energy distribution of the beam. By convention, this condition is called the “ideal condition” [39,40]. For each n (λ given), there is only one set of (θ_i, θ_f) such as the peak is in ideal condition. This condition is obtained by introducing the $\phi_i = \phi_f$ condition in eq. 3.1 and is given by:

$$\cos(\Phi) = \frac{n\lambda}{2h} \quad , \quad \text{where } \Phi = \phi_i = \phi_f. \quad (3.7)$$

Most of the deposition measurements of this work have been performed in these ideal conditions. They avoid the interpretation problems linked to the terrace distribution and provide intense peaks important for a good measurement dynamics. An important exception is the case of the $n = 0$ diffraction order. It is characterized by $\theta_i = \theta_f$ which is incompatible with the ideal condition $\phi_i = \phi_f$. However this peak is very useful for probing the surface step edges, because it allows more grazing geometries than the $n < 0$ orders. The sensitivity of the $n = 0$ peak with respect to the scattering geometry is treated in chapter 5.

Depending on the geometry and the surface temperature, the intensity in an ideal peak may collect up to 20% of the primary beam intensity [40]. The echelette structure of the vicinal surfaces is responsible for this as it allows only a few peaks to receive significant intensity. This is an advantage of the vicinal surfaces for a use as energy analyzer (see chapter 10).

D) Example of a He diffraction pattern for Pt(997)

An example of a measured diffraction pattern for clean Pt(997) is shown in figure 3.7. It illustrates the different points developed above.

The incidence angle ϕ_i has been chosen so that the $n = -2$ diffraction peak is in ideal condition. Its width is 0.12° , which is equal to the width of the direct beam. Its position does not correspond to the maximum of the effective form factor (dashed line). A shift of 4.5° towards smaller scattering angles is found between the center of gravity of the effective form factor and the specular direction $\phi_i = \phi_f$ marked by the ideal $n = -2$ peak.

The last point is very interesting: the position and width of the diffraction peaks seem to be uncoupled from the form factor position. Only their relative intensities are determined by the form factor. It addresses the question concerning the origin of the shift of the form factor maximum:

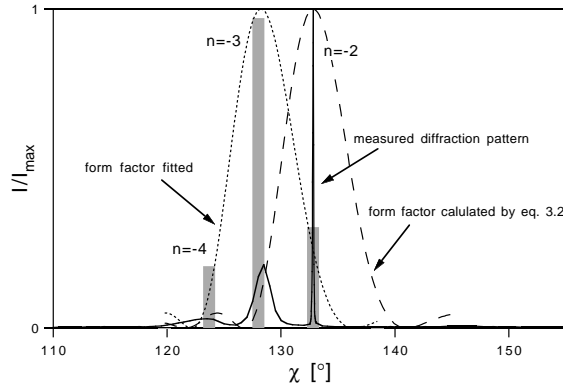


Figure 3.7: He diffraction pattern of Pt(997). short dash: form factor fitted from the integrated intensity (vertical bars). long dash: form factor calculated by eq. 3.2. $\phi_i = 66.4^\circ$, $\lambda = 0.91 \text{ \AA}$. *N.B.:* the scale for the He diffraction pattern is different from the scale for the bar plot and the form factors.

in a simple approach, Harris *et al.* [49] explain the shift by assuming that the attractive equipotentials are parallel to the macroscopic surface. When a He-atom penetrates the attractive potential region, it is accelerated towards the surface, which is equivalent to a refraction process between the vacuum, with a refractive index equal to unity, and a medium with a larger refractive index. The attractive potential introduces thus an additional phase difference in the partial He beams reflected by the surface, with respect to the free plane wave approximation assumed above. This approach is able to reproduce the shift of the form factor maximum. However, if the attractive equipotentials were parallel to the macroscopic surface, the induced phase difference would be different for partial He beams originating from different points on the terrace and the 3D-Bragg condition would not be fulfilled for $\phi_i = \phi_f$. This approach should thus equally lead to substantial peak shifts and width changes, which are not observed. In particular, the peak in ideal condition is within the precision of the instrument exactly found at the position given by eq. 3.7, whatever the incidence angle is.

The observed diffraction patterns could more satisfactorily be explained by a step-bending within Comsa's approach [47]. This approach is compatible with the fact that the ideal condition is independent of the form factor maximum, as the attractive equipotentials are implicitly assumed parallel to the microscopic surface. However, this explanation encounters other physical problems, because it appears to be contrary to the

Figure 3.8: Schematic setup of a X-ray backscattering Laue diffraction experiment.

The schematic setup of a backscattering Laue diffraction experiment is represented in figure 3.8. A collimated white beam of X-rays is produced in the source. The polychromaticity of the source guarantees that a wide range of diffraction peaks are in Bragg condition, which allows then an accurate characterization of the sample structure. The X-ray beam passes perpendicularly through a photographic plate, where it leaves a reference spot, and then hits the sample. The sample is mounted on a triple axis goniometer which allows a precise adjustment of its orientation. By means of a telescope, the macroscopic surface is aligned as well as possible parallel to the photographic plane (precision $\sim 0.5^\circ$). The backscattered diffraction beams are then recorded on the photographic film. If the distance between the sample and the photographic plate is known, it is possible to index the diffraction spots and determine the sample bulk orientation [58]. Moreover, as the surface is parallel to the film, the orientation of the surface is also included in the photography: its normal corresponds to the direction of the reference spot of the incident beam. All the information is thus contained in the photography of the diffraction pattern. The indexing procedure has been carried out for (997) and (779) platinum surfaces and is presented in figure 3.9.

This method does not allow to determine the angle between the [111] and the surface directions with an accuracy better than about 0.5° . The exact value of the surface Miller's indices is thus not certain. However, it constitutes an easy and important check to distinguish between the samples, when the sample supplier confuses the miscut directions.

Figure 3.9: Backscattering Laue diffraction pattern for (a) Pt(997) and (b) Pt(779), according to the procedure described in the text. Insets on the right side: indexes of the vertical branches. Insets at the bottom: sample orientation illustrated for the two vicinal surfaces.

Chapter 4

Row-by-row growth at vicinal surfaces

4.1 Introduction

Manipulating the morphology of epitaxial films through detailed control of the growth kinetics has attracted much interest recently. A primary goal is the layer-by-layer growth of smooth films with abrupt interfaces. The most widely used techniques for monitoring the growth mode are diffraction techniques [22,24,59,60], where the occurrence of intensity oscillations provides unique evidence for the desired two-dimensional (2D) growth. These oscillations in the diffracted or specularly reflected intensity reflect the periodically varying step density of homogeneously nucleating and successively coalescing 2D islands.

The presence of substrate steps can suppress the homogeneous nucleation on terraces in favor of heterogeneous step nucleation still permitting smooth two-dimensional growth. Binding energies for adatoms at step sites are in general larger than on terrace sites due to the increased coordination. As a consequence 2D islands preferentially nucleate at steps if the average adatom diffusion length is larger than the terrace width [61–63]. In the submonolayer range this can be exploited to grow quasi one-dimensional systems like quantum wires using substrate step arrays as a template [64,65]. Similar to the growth mode classification in thin film epitaxy different step decoration modes can be distinguished, the occurrence of which depend on the detailed interaction of the adsorbate with the substrate step [66].

In this chapter we demonstrate that the step decoration modes can be studied by specular thermal energy He scattering at grazing incidence. For a regularly stepped Pt(997) surface we find during the adsorption of rare gases and during the deposition of metals in the sub-monolayer range oscillations in the reflected helium intensity. These intensity oscillations reflect the sequential growth of rows at the steps (named here discrete row growth or row-by-row growth) during deposition.

4.2 Experimental

The vicinal Pt(997) surface has been chosen as a substrate because it exhibits a regular step-terrace ordering with a narrow terrace width distribution (see chapter 3). The initial growth of the rare gas Xe and the metal Ag on this surface has been studied by He-TEAS in grazing incidence scattering geometry. The preparation of the surface is done according to the usual procedure (see section 3.3), by repeated argon ion sputtering cycles at 750 K, followed by annealing at 900 K. While the rare gases are adsorbed on the Pt(997) surface from the ambient gas phase, Ag is deposited with a molecular beam effusion cell.

4.3 Results

4.3.1 Row-by-row growth

Xe films on Pt(997) grow in a 2D growth mode. This can be seen from the oscillations in the specularly reflected He intensity shown in figure 4.1 (note that the scattering geometry is far from grazing incidence and specular to the (111) terraces). As explained in section 2.3.2, each intensity maximum corresponds to the completion of a Xe layer. The damping of the oscillations is mainly due to the large Debye-Waller factor of Xe-multilayers. The measurement in figure 4.1 can be used to calibrate the coverage by the maxima of the layer-by-layer oscillations. The Xe monolayer (ML) is found to correspond to a coverage of $\Theta \approx 0.33$ [67].

At grazing incidence intensity oscillations are observed already in the sub-monolayer range. This is shown in figure 4.2 for Xe adsorption at 40 K. As will be discussed below, these oscillations result from a row-by-row attachment of adsorbates at the steps. A second system which exhibits oscillations due to discrete row growth is the Ag/Pt(997) system as is demonstrated by the second curve in figure 4.2. This metal on metal system has different physical and chemical properties than the physisorption system discussed above. It exhibits pseudomorphic growth with an adatom density equal to the substrate atom density [68]. At 350 K we observe again the characteristic He intensity oscillations with a pronounced maximum at a coverage of approximately one eighth of a monolayer and a shoulder at approximately two eighths, corresponding to the sequential growth of two rows. Note that due to the (1×1) pseudomorphic structure the atom density in the Ag row is three times as large as in the Xe row. The submonolayer He reflectivity oscillations are most pronounced at grazing incidence close to 90° , diminish upon decreasing the incidence angle and finally disappear at around 70° (see chapter 5). The intensity of the individual peaks depends strongly on the scattering geometry. For Xe/Pt(997) in figure 4.2 the geometry was chosen to maximize the intensity in the second row peak.

Discrete row growth is the only plausible explanation for the oscillations. First, the

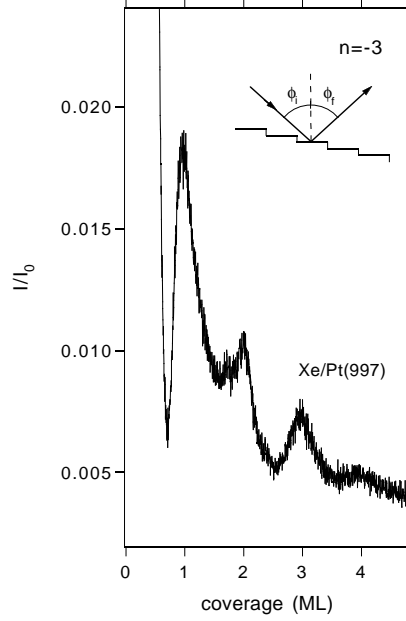


Figure 4.1: He scattering intensity normalized to the intensity at zero coverage as a function of Xe coverage at non-grazing angles. Incidence angle of the He beam with respect to the surface normal $\theta_i = 53.9^\circ$, exit angle $\theta_f = 41.0^\circ$. The geometry corresponds to specular reflection with respect to substrate terraces, $\phi_i = \phi_f$, and a diffraction order $n = -3$ with respect to terrace periodicity. Xe ambient pressure 1.7×10^{-8} mbar, surface temperature $T=34$ K, He beam wavelength $\lambda_{He}=1.03$ Å.

two discussed systems are known to exhibit step decoration. Island formation on the narrow terraces can be excluded at the temperatures of the experiments. Thus preferential adsorption at the step will occur. Second, the observed oscillations are no interference effects because the coverage value at the maxima is found to be independent of geometry.

The new observation of discrete row growth is specific for vicinal surfaces. Its clear observation depends on the presence of a sufficiently high step density and a regular step-terrace ordering as will be discussed below. At appropriate surface temperatures the adatom mobility is high enough on the terraces to allow migration to the steps. Once attached to the steps the mobility is reduced. Due to the random nucleation of 1D nuclei

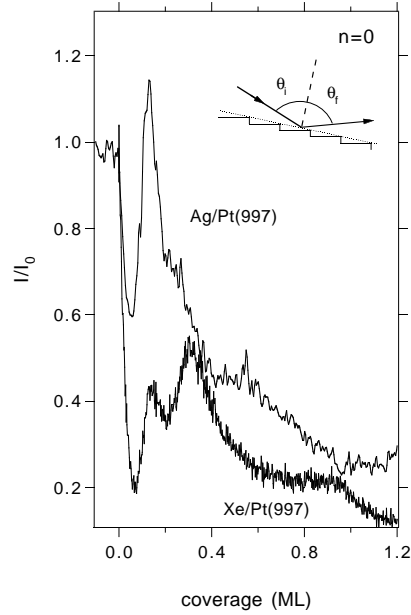


Figure 4.2: Specular He scattering intensity at grazing angles as a function of Ag coverage (top) and Xe coverage (bottom). Ag: surface temperature $T=350$ K, $\theta_i = \theta_f = 85.0^\circ$, $\lambda_{He}=0.97\text{\AA}$. Xe: surface temperature $T=40$ K, $\theta_i = \theta_f = 76.2^\circ$, $\lambda_{He}=1.14\text{\AA}$. Note that in the grazing scattering geometry the incident and reflected He beams are specular to the macroscopic surface normal (i.e. diffraction order $n = 0$).

the defect (kink) density increases in the beginning of the step decoration resulting in a decrease of reflected He intensity. During further attachment of atoms to the step the 1D nuclei grow laterally and finally coalesce to form a row with decreasing defect density. For a completed row the defect density reaches a minimum resulting in an intensity maximum.

The similarity of the oscillations exhibited for the two systems -Xe and Ag on Pt(997)- suggests similar step edge decoration in the two cases. It is known that in the case of Ag the attachment occurs exclusively at the bottom of steps [63]. Recent STM studies of Xe adsorption on Pt(111) have suggested that Xe might preferentially bind at upper edges of isolated steps [69]. We found that this is not the case for Xe growth at the vicinal Pt(997) surface. A detailed diffraction study for one and two complete Xe rows shows a

shift of the diffraction intensity form factor towards larger diffraction angles with respect to the clean surface (see section 6.2). This indicates a reduction of terrace bending [47] only consistent with Xe decoration of the lower step edges.

Due to the increased coordination of the adsorbate at the lower step edge, the adsorption energy is higher at the step than on the terrace. After the formation of a complete row adsorption can continue by the attachment of further rows depending on the adsorbate - adsorbate interaction potential and the range of the adsorbate - step interaction potential. The result is a more or less complete row-by-row growth resulting in a sequence of He intensity oscillations. The row oscillations for the two systems presented here disappear after two rows (figure 4.2). The main reason is the decreasing adsorbate-step interaction strength. In the physisorption system Xe/Pt(997) for example one can assume that the difference in binding energy for an atom in row n and in row $n+1$ decreases with increasing n . As a result, at a given temperature the row-by-row growth will become less strict. Thermodynamically, discrete row growth is favored with decreasing temperature [66]. At too low temperature, however, the decreased mobility of the adatoms and the finite adsorbate flux will finally obstruct any row-by-row growth. It can be concluded that row-by-row growth will be observable for a given row number n only over a limited temperature range. The fact that the same growth mode is observed for two qualitatively different adsorbate systems in different temperature ranges underlines the generality of the growth mechanism.

The oscillations will only be perfectly observable for substrate surfaces with equidistant steps. For a homogeneous deposition rate the uptake of adsorbates is higher on longer terraces than it is on shorter ones and the first and further rows will be completed on longer terraces earlier than on shorter ones. As a result the intensity maxima will smear out with increasing coverage because the terrace lengths exhibit a distribution function of finite width. For a coverage of more than half a monolayer, however, the peak broadening will reduce again and - apart from statistical fluctuations in the adsorption - the monolayer coverage is reached on all terraces at the same time. Thus for real surfaces the visibility of discrete row growth is best just above and below integer layer coverages (see also chapter 8).

4.3.2 Thermodynamics

We have further studied row-by-row growth with respect to its thermodynamic properties. Figure 4.3. shows adsorption measurements for a Xe gas pressure of 3×10^{-8} mbar at different surface temperatures. At this pressure Xe multilayer adsorption occurs below 57 K and monolayer adsorption below 91 K [39]. It can be seen from figure 4.3. that at 100 K adsorption ends exactly on the first peak. When the first row is complete, equilibrium with the gas phase is attained and no further adsorption takes place. A

similar control of second row formation would require a precise temperature adjustment because of the small difference in binding energy between the second and further rows.

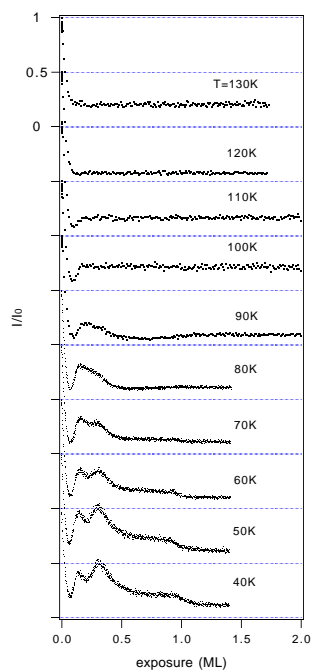


Figure 4.3: Normalized specular He intensity in grazing incidence geometry $\theta_i = \theta_f = 76.2^\circ$ ($n = 0$) as a function of Xe exposure to Pt(997) at different surface temperatures. In the range of Xe monolayer adsorption, $T < 90.9$ K, the exposure scale is identical to coverage. Ambient Xe pressure 3×10^{-8} mbar, $\lambda_{He} = 1.03 \text{ \AA}$.

In order to estimate step binding energies for the Xe/Pt(997) system we first deposited a certain number of Xe rows. The exact dosing was controlled by the intensity variations in the reflected He beam. By temperature variation a controlled desorption of adsorbate atoms from the step onto the terrace and a re-condensation at the step is then performed. The process can be followed by specular He scattering under grazing incidence due to the change in diffuse scattering of the He beam. Figure 4.4 (a) and (b) show repeated heating/cooling ramps for an initial coverage of one and two rows, respectively. For the

second row a reversible variation of reflected He intensity is observed (figure 4.4b). The first row, however, is more strongly bound to the step and atoms do not detach from the step below the temperature where also desorption from the surface occurs. As a result, no change in reflected He intensity can be observed (figure 4.4a) below Xe desorption temperature.

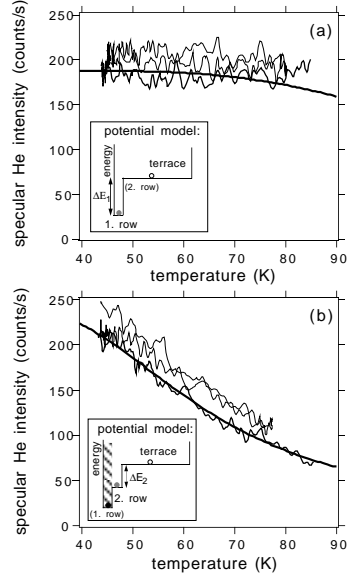


Figure 4.4: Specular reflected He intensity at grazing incidence geometry during temperature sweeps after adsorption of one row (a) and two rows (b) of Xe. The jagged lines represent the measurements, the thickest lines are fits according to the model described in the text. The temperature range was chosen to avoid adsorbate desorption. The equilibrium situation and the absence of desorption are demonstrated by the reproducibility of the behavior in the successive upward-downward-upward temperature ramps coded by increasing line thickness. Insets: potential schemes employed for fitting (see text).

The experiment can be interpreted quantitatively within the frame of a simplified potential model. Assuming that the intensity in the $n = 0$ order comes exclusively from a reflective stripe at the step edge, an adsorbate atom leaving a complete row produces a vacancy which reduces the reflectivity of the row. We call σ the linear cross section

for diffuse scattering of a vacancy in the row. The vacancy density in the row is inferred from statistical thermodynamics and is calculated by minimizing the free energy of the system for a Xe coverage of 1 row. In the calculation, an increased binding energy ΔE_n in the row n is assumed with respect to the terrace sites. The intensity in the $n = 0$ order is then obtained by subtracting the unreflective contribution of the vacancies from the intensity of a defect free row (I_0). Effects due to the interaction between adsorbate atoms are neglected. With the two free parameters σ and ΔE_n the specularly reflected He intensity (*i.e.* in $n = 0$) as a function of temperature is obtained as:

$$I(T) = I_0 \left[1 - \frac{-(n_s + n_t) + \sqrt{4 \left(e^{\frac{\Delta E}{kT}} - 1 \right) n_s n_t + (n_s + n_t)^2}}{2n_s \left(e^{\frac{\Delta E}{kT}} - 1 \right)} \right]^{\frac{a}{\sigma}} \quad (4.1)$$

where n_t is the number of terrace adsorption sites, n_s is the number of row sites in an arbitrary surface area (assuming a reasonable hollow adsorption site of the Xe atoms (see chapter 6) $n_t/n_s = 21$ for the first row and 18 for the second one), and a is the lattice constant in the Xe row, which is 4.1 Å as will be discussed in chapter 6). A detailed derivation of this equation is given in Appendix A.

In a first step we fit function 4.1 to the measurement for two rows coverage (thick line in figure 4.4b) assuming that the first row stays completely occupied and that the third to eighth row are degenerate in energy (inset figure 4.4b). We obtain the best fit parameters $\Delta E_2 = 22 \text{ meV}$ and $\sigma = 3.5 \text{ \AA}$. σ is of the order of magnitude of the Xe interatomic distance in the row. It is small in comparison to usual diffuse scattering cross section of adsorbates on flat surfaces, which exhibit values significantly larger than the atomic extension of the defect (typically $\Sigma = 100\text{\AA}^2$, *i.e.* $\sim 11\text{\AA}$ in diameter, for rare gas atoms [17]). This small value of σ indicates that the intensity in the $n = 0$ order originates from the repulsive potential at the step edge and is not influenced by the attractive potential, which is responsible for the large values of Σ . In the next step, we utilize the value for σ in order to fit the behavior in the case of one adsorbed row. Assuming that the second to eighth row are degenerate (inset figure 4.4a), we obtain a lower limit for the excess binding energy $\Delta E_1 > 55 \text{ meV}$. With respect to the terrace adsorption energy in the first layer of Xe/Pt(111) of 277 meV [67], the first and second row thus exhibit a relative excess binding energy of >20% and 8%, respectively. These values are comparable to estimates from isosteric heat measurements for Xe adsorption on vicinal Pd surfaces [70]. A more detailed interpretation of discrete row growth requires a more sophisticated model for adsorbate-substrate interaction. Such a detailed study is the subject of chapter 6.

4.4 Summary

In conclusion, we demonstrated a novel experimental approach for the in-situ study of step decoration. The observed discrete row growth and its real time monitoring with grazing incidence He scattering opens up the way for the fabrication of 1D superlattices with atomic scale periodicity.

Chapter 5

Step sensitivity of grazing incidence He scattering

5.1 Introduction

Steps are the most abundant defects at crystalline surfaces and are known to strongly influence surface processes such as sticking, chemical reaction, epitaxial growth and many more. The eminent importance of steps for crystal growth has already been recognized by Kossel 70 years ago [8]. Binding energies for adatoms are in general larger at steps (and in particular at kink sites in the steps) than on terrace sites due to the increased coordination. As a consequence a new crystal layer is built by adding atoms to the step sites if the average adatom diffusion length is larger than the terrace width [61–63]. Today, this growth mode is usually called step-flow-growth. It is the dominant growth scenario at high substrate temperature and low supersaturation, where thermodynamics dominates kinetics. Step decoration in heteroepitaxial systems can be exploited to grow quasi one-dimensional structures like quantum wires. Here the substrate step arrays act as a template [64, 65].

Indirect demonstrations of preferential adsorption at step sites have been obtained by thermal desorption spectroscopy [71] or photoelectron spectroscopy [70]. The in-situ observation of step decoration, however, is a challenging experimental task. The technique to be employed has to be at the same time sensitive to minute amounts of coverage and selective to the population of step sites. The most powerful tool to study defects at surfaces is certainly the scanning tunneling microscope. It provides direct, real-space images of the surface topography on the atomic scale. In some cases (in particular close packed metal surfaces) it is however not easy to obtain atomic resolution in the immediate vicinity of steps. Among the available scattering techniques, TEAS is particularly sensitive to the presence of adatoms and defects due to its very large cross section for diffuse scattering [17]. This unusual sensitivity has been largely exploited to study the lateral

Figure 5.1: Side view of the bare vicinal (997) Pt surface (miscut angle $\alpha = 6.45^\circ$) and employed experimental scattering geometries: the $n = 0$ order reflection is specular to the (997) macroscopic surface ($\theta_i = \theta_f$). The higher diffraction orders (*e.g.* $n = -3$) are always chosen to be specular to the (111) terraces ($\phi_i = \phi_f$). This implies that only $n = 0$ is accessible even in extremely grazing geometry.

In this chapter, we study as a model system the growth of Ag on Pt(997) in the sub-monolayer range in order to characterize the strength of the experimental method. We determine the variation of step sensitivity with incidence angle and compare the observation of the heteroepitaxial system with results for the homoepitaxial Pt/Pt(997) system. The vicinal Pt(997) surface (figure 5.1) has been described in section 3.3. The surface is characterized by a regular step-terrace ordering and acts essentially as an echelette grating for He matter waves [47, 73]. The position of the He-diffraction peaks for such a grating is given by the one-dimensional Bragg-law (see section 3.3.2):

$$n\lambda = (h/\sin\alpha)(\sin\theta_f - \sin\theta_i), \quad n \text{ integer} \quad (5.1)$$

where θ_f and θ_i are the angle of incidence and the scattering angle with respect to the macroscopic surface normal, $h = 2.27\text{\AA}$ is the step height and α is the angle between the (111) and (997) direction. Note that, in order to achieve maximum sensitivity to steps, the measurements were made in step-down incidence, as shown in figure 5.1. All $n < 0$ measurements are made under in-phase scattering conditions for which (5.1) must hold as well as $\theta_i - \alpha = \theta_f - \alpha$. This particular scattering geometry avoids interpretation problems associated with the finite terrace width distribution of the substrate. However, it defines for a given He wavelength both angles θ_f and θ_i and thus allows no variation of geometry. The $n = 0$ diffraction peak cannot be observed in this so-called "ideal" condition because specular reflection with respect to the macroscopic (997) surface (i.e. $\theta_i - \alpha = \theta_f - \alpha$) is not compatible with an in-phase condition with respect to the terraces.

5.2 Experimental

In order to study the Ag nucleation and growth at the vicinal platinum surface, and in particular the decoration of the steps, we monitor the intensity of the different diffraction peaks during deposition. The intensity variation during deposition provides direct information on the ordering and thus on the growth at the vicinal surface. The experiments were made at a He wavelength of $\lambda = 0.92\text{\AA}$. The Pt(997) crystal has been prepared and cleaned in the usual way (see section 3.3). Ag was evaporated with an MBE-Knudsen-cell with typical deposition rates of a few 3×10^{-3} ML/s.

5.3 Results

5.3.1 Ag growth on Pt(997)

From STM studies on Ag/Pt(111) it is known that the first Ag layer grows pseudomorphically and its growth mode is of the Stranski-Krastanov type [68]. Around room temperature up to 6 monolayers grow in a layer-by-layer fashion before 3D-growth sets in. In figure 5.2a we show the intensity variation of the $n = -3$ He diffraction peak as a function of Ag coverage. This scattering geometry is far from grazing incidence and specular to the (111) terraces, probing the defect density of the Ag adlayer on the terraces. The observed intensity oscillations demonstrate the layer-by-layer growth for Ag on Pt(997) at 350K up to 3 monolayers. The oscillations reflect the periodically varying step density of nucleating and successively coalescing islands. The first maximum is employed

to calibrate the ML coverage. It can be noticed that this growth is imperfect indicated by the continuously decreasing intensity of the reflectivity maxima and their increasing shift with respect to integer coverages. For more detail, see chapter 8.

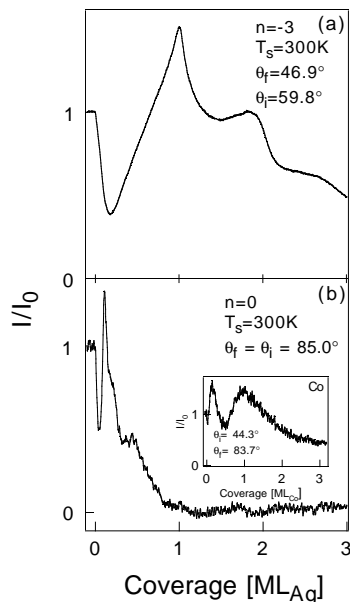


Figure 5.2: Normalized He reflectivity as a function of Ag coverage in the $n = -3$ diffraction order (a) and in grazing scattering geometry $n = 0$ (b). Inset: Reflectivity for Co adsorption on Pt(997) at less grazing incidence and grazing exit.

For the zero order diffraction beam in grazing incidence, the behavior of the reflected He intensity is quite different. Pronounced intensity oscillations are already observed in the submonolayer range, whereas the intensity maxima accompanying the completion of the mono- and bilayer are not clearly visible anymore (figure 5.2b). The first and most pronounced peak is situated at about $1/8$ of a monolayer, and can be assigned to the formation of a complete Ag-row at the bottom of the Pt-steps (see chapter 4), which is consistent with the facts that the (111) terraces on the Pt(997) surface have on the average 8 rows of atoms and that the first layer of Ag grows pseudomorphic. The position of the peak does not change with scattering geometry and can thus be attributed to a

structure occurring at a defined coverage. The presence of this peak can be explained - by analogy with the oscillations in layer-by-layer growth - by the variation of the defect density at the steps during row formation. When the defect density is at its minimum, which corresponds to row completion, the scattered intensity reaches its maximum. We thus find that for grazing ($\theta_i = 85^\circ$) incidence the reflectivity becomes very sensitive to the ordering at the step. The fact that the intensity of the first row peak maximum is higher than the initial intensity does not necessarily indicate that the ordering at the step is better after decoration with a Ag row. More probably, it is the consequence of the "electronic contrast" between Ag and Pt which results from the change of the potential felt by the He-atoms near the steps.

In the measurement (figure 5.2b), the formation of the second row is not well marked and appears only as a shoulder of the first row peak. The origin of this low intensity could be (1) a changing interference in the diffraction from the terrace, to which the $n=0$ reflection is sensitive, (2) a smearing-out of the maximum due to the loss of growth coherence between different terraces or (3) a transition to a structure with increased roughness similar to a two-dimensional Stranski-Krastanov growth mode. A calculation presented in chapter 8 will show that the second effect is probably the dominating one for the observation of row completion: the terrace width distribution of Pt(997) is too large to allow the observation of the possible completion of the third row.

5.3.2 TEAS step-terrace sensitivity

Two contributions can be responsible for the high sensitivity for row-growth demonstrated in figure 5.2b. They correspond to contributions from which step sensitivity arises and which were already discussed in the early literature of He scattering from stepped surfaces [47, 74]. First, for increasing incidence angle the terrace moves more and more into the shadow cast by the step. Second, measurements in the zeroth diffraction order of a vicinal surface are by themselves sensitive to the step edge. This is due to the fact that the intensity form factor for reflection from a flat terrace provides only little intensity in the zeroth diffraction order. The main intensity comes from the bending of the repulsive He-surface potential at the step. Experiments done on row growth under less grazing incidence and grazing exit angle have also shown a substantial step sensitivity as illustrated by the inset in figure 5.2b showing Co adsorption. We can thus conclude that the grazing exit angle is essential for the step sensitivity while the grazing incidence improves the illumination of the steps by the He beam. The $n = 0$ condition takes advantage of both contributions.

In order to demonstrate this latter dependence we performed reflectivity measurements in $n = 0$ diffraction order for different angles of incidence. In figure 5.3 the reflectivity is plotted as a function of Ag coverage for angles of incidence varying from 72.8° to

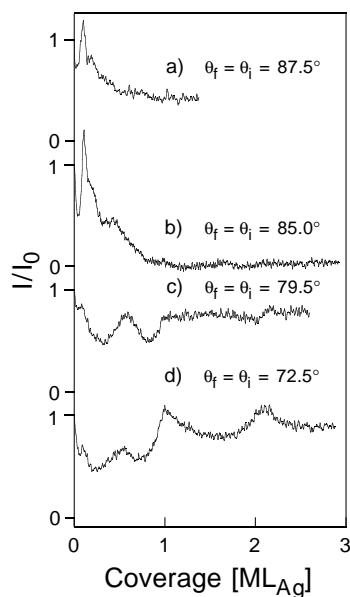


Figure 5.3: Normalized He reflectivity in $n = 0$ diffraction order as a function of Ag coverage for different exit angles. Note the transition from step-sensitivity for grazing geometry (a and b) to terrace-sensitivity for more normal geometry (c and d).

87.5° . We can clearly see the transition from the rather terrace sensitive more normal incidence (curves d and c) to the step-sensitive grazing incidence (curves a and b). The relative intensity of the first row peak decreases slowly with the angle of incidence, while the monolayer peak becomes more prominent. It should also be noticed that the second row peak, which was only a shoulder in figure 5.2b, can be well resolved at extremely grazing incidence (87.5°). This series of measurements demonstrates nicely the crucial importance of the scattering geometry on the step sensitivity. In addition to the choice of the diffraction order it is the grazing scattering geometry which contributes to the extreme step sensitivity. While this general rule holds, we remark that for certain systems a first row maximum can be observed even in higher ($n \neq 0$) order reflections. These maxima (or shoulders) are, however, broad and by far not as well defined as in the zeroth diffraction order.

Similar results have been obtained for a variety of adsorbates on Pt(997) including the

rare gases Xe (see also chapter 4 and 6) and Kr (chapter 7) and the metals Cu and Co. In the case of Xe, a row-by-row growth until the second row is observed, whereas only the first row is observed for Kr, as for the metals Co and Cu. These results demonstrate that the initial row growth of adsorbates at steps is a widespread phenomenon. TEAS in grazing incidence geometry is a method well adapted to study this special type of step decoration and holds promising perspectives for studying order-disorder phenomena at steps in general.

5.3.3 Difference between homo- and heteroepitaxy

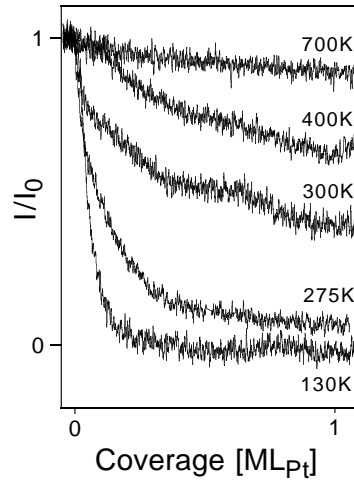


Figure 5.4: Normalized He reflectivity in $n = 0$ diffraction order ($\theta_f = \theta_i = 80^\circ$) as a function of Pt coverage for different adsorption temperatures.

At the end, we would like to shed some light on the growth mode from a different point of view. Even though row growth is widespread we found this growth mode so far only for heteroepitaxial systems. The adsorption of Pt on Pt(997) does not show intensity oscillations (figure 5.4). In the temperature range between 130 K and 700K we find a continuous transition from an exponential decay of He reflectivity to a constant reflectivity. This behavior has to be interpreted as a transition between a steadily increasing defect density (growth of rough steps) to a growth mode with constant defect density (“kink flow”). At intermediate temperature the reflectivity decreases initially but

appears to approach an equilibrium value which depends on the adsorption temperature. We may speculate that the transition from 1D to 2D growth is governed by changes in the diffusivity at step-edges. We emphasize that there is no temperature range for which row-growth is observed in this homoepitaxial case. One may ask whether this result has to be attributed to a missing 'chemical contrast' for He scattering or whether it indicates a different growth mechanism. In the case of a substantial 'chemical contrast' a kink flow in heteroepitaxy would lead to an initial change of reflectivity because a substrate kink remains a diffuse scatterer even if adsorbate atoms attach to the kink and continue the growth of the row. If the diffusion of an adsorbate atom along the substrate step is fast the defect density is expected to stay constant during the completion of the row. The oscillating intensity observed in heteroepitaxy, in contrast, indicates that the defect density reaches a sharp maximum at about half row coverage. This strongly suggests that in Pt/Pt(997) homoepitaxy and Ag/Pt(997) heteroepitaxy actually different growth modes prevail.

5.4 Summary

In conclusion, we have shown that grazing incidence thermal He reflection allows to study defect densities at steps and thus accesses step decoration modes. It opens the possibility to study in detail structures and phase transitions in one dimension. The method can be used for any surface with sufficiently high step density and is essentially based on the geometric enhancement of the step contribution to the reflected He intensity.

Chapter 6

Xe adsorption on Pt(997): theory and experiment

6.1 Introduction

Multilayer adsorption, has been widely studied [75,76] and the influence of defects [77] has been shown to be important for the wetting/non wetting transitions which generally occur in adsorbed phases. Indeed, it is since long known that substrate steps are preferential nucleation sites for adsorbates [61,62] due to the increased coordination at step sites. The observation of desorption peaks at increased temperatures and of supplementary UPS peaks [70,71] for small amounts of adsorbates compared to the monolayer behavior has established step decoration of Xe atoms on vicinal Pt and Pd surfaces. For a sufficiently strong interaction of the adsorbate with an already wetted step a continued attachment of a second row and further rows at the step can be expected. This behavior which we call discrete row growth or row-by-row growth is defined equivalently to layer-by-layer growth. This means that, with increasing coverage, the sub-monolayer film forms a sequence of stable uniform rows with each row being completed before the successive one nucleates. Although its possibility was discussed in literature [66], this growth mode remained speculative until recently because of the lack of experimental evidence, on one hand, and the lack of realistic interaction potentials, on the other hand. A detailed theoretical analysis of row-by-row growth requires the modeling of a real system exhibiting this phenomenon.

In the preceding chapter, we demonstrated the sensitivity of grazing incidence TEAS to the order in rows adsorbed at steps. Row completion is observed by maxima in the scattered He intensity. Discrete row growth is observed for the systems Xe, Ag and Kr on Pt(997). In this chapter, we focus on the Xe/Pt(997) system which is a model system for physisorption. The terrace structure relates this system to the Xe/Pt(111) system which has been studied in great detail [67,78].

The aim of this chapter is to model discrete row-by-row growth using the best available potential form in the literature. We selected the one which appears to be the most appropriate when surface steps are considered for describing the interactions between Xe atoms and the Pt substrate, and the Xe-Xe lateral interactions. Two semi-analytical approaches are developed which describe the statistical distribution of the Xe atoms in the adsorption sites of a confined terrace. The ideal lattice gas model does not take into account the lateral interactions in the adsorbate but it is expected to give qualitatively the main part of the experimental features. In the mean field Ising model, the influence of the lateral interactions is considered, and it is believed to be accurate enough to quantitatively interpret the experiments. We focus here on the physical process which is involved to favor this row-by-row growth; we thus calculate the mean coverage of a row in terms of a truncated series expansion with respect to the lateral potential in order to keep analytical simplicity to the model. To get better accuracy would require the use of more accurate potentials and of involved numerical methods [66] such as transfer matrix procedures which would, however, not provide additional fundamental understanding of the growth phenomenon.

6.2 Experiment

The Xe/Pt(997) adsorbate system is studied experimentally by TEAS. This method allows the in-situ determination of the growth mode in thin film epitaxy [79]. Moreover, employing grazing incidence geometry, the method becomes very sensitive to the one-dimensional growth of rows attached to steps, as was shown in chapter 5. This sensitivity has been attributed to He reflectivity changes between complete and incomplete adsorbate rows at step edges.

Figure 6.1 shows measurements of the specularly reflected He intensity as a function of coverage at different temperatures in grazing incidence geometry. Xe is adsorbed on the Pt(997) surface by backfilling the sample chamber with Xe at 3×10^{-8} mbar. The temperature dependence will be discussed in detail in section 6.4. Here we focus on the bottom curve of Figure 6.1 ($T=40$ K) and find that the intensity shows a rapid decrease of reflected intensity during build-up of coverages below 0.07 ML. During further adsorption the reflected intensity exhibits maxima at $\theta = 0.14 \pm 0.02$ ML and $\theta = 0.30 \pm 0.03$ ML. The appearance of maxima upon row completion is explained similarly to oscillations in layer-by-layer growth by the presence of a minimum of defects (i.e. kink sites in this case). The maxima are not due to mere interference effects because for different scattering geometries the peaks appear always at the same coverage. It is known that Xe on Pt(111) exhibits step decoration. Ordered structures are formed when adsorbate rows are completed. The peaks are found to broaden with increasing coverage. This is due to the variation of terrace width because larger terraces have a larger uptake of Xe atoms

than smaller terraces have. In the following we will show that the coverage values can be well explained by the formation of complete rows.

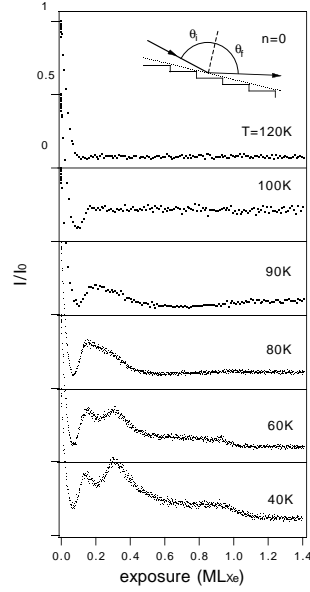


Figure 6.1: Specular reflected He intensity at grazing angles ($\theta_i = \theta_f = 76.2^\circ$) as a function of Xe coverage on Pt(997). The measurements were made at the indicated surface temperatures. For the employed Xe background pressure of 3×10^{-8} mbar the exposure scale corresponds to a coverage scale for surface temperatures $T \leq 90$ K, $\lambda_{He} = 1.03$ Å. The Xe monolayer coverage (ML_{Xe}) is defined as the coverage corresponding to a complete adlayer.

The structure of Xe on Pt(997) at monolayer and sub-monolayer coverages has not yet been fully established. On a Pt(111) surface, Xe is known to form a commensurate $(\sqrt{3} \times \sqrt{3})R30^\circ$ superstructure over a wide temperature and coverage range [11] with an average distance between nearest neighbor atoms equal to 4.8 Å. If this structure was also the most stable on Pt(997) terraces, an average (997) terrace could thus accommodate 7 or 8 Xe rows parallel to the step edge. In order to determine the structure on the vicinal surface we measured He diffraction spectra. In figure 6.2a a diffraction scan in $\langle 11\bar{2} \rangle$ direction from a Xe monolayer is shown for fixed incidence angle. The two intense diffraction peaks on the left hand side are peaks due to specular scattering from the

terraces (i.e. form factor $m=0$ (see section 3.3.2)). The peak splitting corresponds to the 20 Å periodicity of the surface. In this geometry diffraction peaks from the Pt row distance of 2.40 Å will not be visible as their total scattering angle χ exceeds 180° . The three peaks to the right of the specular peaks are due to diffraction from a Xe structure with a row distance which must be increased with respect to the substrate. The peak positions and the maximum of their intensity form factor ($m=1$) contain the information on the Xe row distance. The peak spacing reflects again the surface periodicity. From an analysis of these peaks and peaks of diffraction scans in different geometries a Xe row distance of 3.87 Å is inferred. The difficulty to extract this value will be treated in more detail in chapter 7 in the similar case of Kr on Pt(997). In a diffraction scan parallel to the $\langle\bar{1}10\rangle$ direction, i.e. along the steps (figure 6.2b) a specular peak and a first order diffraction peak are observed. The distance of 4.1 Å derived from these measurements corresponds to the nearest neighbor distance in the Xe rows. The results of the diffraction measurements are attributed to a quasi-hexagonal structure with an average distance between nearest neighbor Xe atoms equal to 4.3 Å. In this geometry, five close-packed Xe rows parallel to the steps cover a terrace. The structure is close to the one observed [71] by LEED for Xe/Pt(332) a surface similar to Pt(997) but with a shorter terrace length. However, the He diffraction peaks become weaker for lower coverages and they cannot be observed below about 0.4 ML. A recent LEED study of Xe/Pt(997) [80] found a Xe-Xe distance of 5.5 Å parallel to the steps for a coverage corresponding to a one-dimensional row of Xe atoms; this means that the Xe-Xe distance parallel to the steps should reduce from 5.5 Å for a single row to 4.1 Å for a complete monolayer.

The fact that the He reflectivity peaks appear at the coverages $\theta = 0.14$ and $\theta = 0.30$ and not at $\theta = 0.20$ and $\theta = 0.40$, respectively, as expected for a five closed-packed adsorbate rows parallel to the step, can have two reasons. First, the sticking probability may decrease with increasing coverage. This assumption can, however, not explain the large discrepancy because the maxima of the layer-by-layer oscillations observed in non-grazing incidence appear at equal dosage intervals [39] allowing changes in sticking coefficient of only a few percent. Second, a structural change may occur between row and layer coverage. In fact, a conclusive explanation of the intensity maxima can be given on the basis of the structural change discussed above. In the first row the atom density for Xe is 1.81 atoms per nm step length while at monolayer coverage the atom density increases to 2.58 atoms per nm in each row corresponding to a total of 12.90 atoms per nm for five rows. The coverage of the first row with respect to a complete monolayer is thus $\theta = 1.81/12.90 = 0.140$ in excellent agreement with the experimental result $\theta = 0.14$. Based on this model the position of the peak ascribed to the second row indicates that the density in the second row is equal to the one of the first row. Taking into account the observation that the diffraction peaks of the monolayer appear at about 0.4 ML coverage the structural change may start after the completion of the second row.

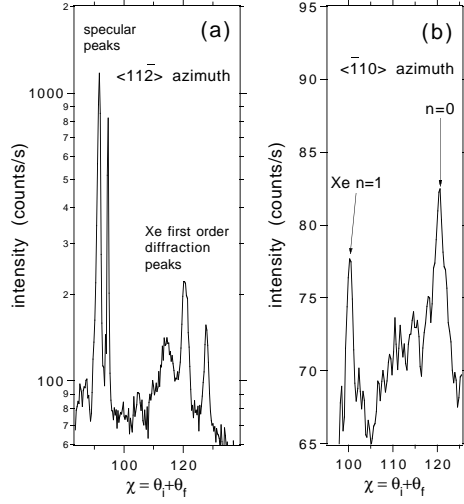


Figure 6.2: Helium diffraction patterns for Xe monolayer coverage on Pt(997) at 45 K surface temperature, $\lambda_{He} = 0.93 \text{ \AA}$. (a) Scan for incidence angle $\theta_i = 59.3^\circ$ and scattering plane perpendicular to the steps. From the evaluation of the three first order diffraction peaks and their form factor, a periodicity and thus a row-to-row distance of 3.87 \AA is obtained. (b) Scan for incidence angle $\theta_i = 60.25^\circ$ and scattering plane parallel to the steps. From the positions of the specular ($n = 0$) and first order ($n = 1$) peaks the Xe-Xe distance parallel to the step of 4.1 \AA is calculated.

Discrete row growth at vicinal surfaces is expected to be a general phenomenon due to the increased binding energy of the adsorbate at step sites with respect to terrace sites. This is related to the increased coordination, which is particularly high at the bottom of the step, where in the case of Pt(997) the adsorbate has a minimum of 5 substrate atom neighbors instead of 3 on the terrace. It was, however, recently argued that Xe might prefer adsorption at low coordination sites and an STM study [69] suggests that already at low coverages Xe atom chains form at the top of isolated steps on Pt(111).

Our study strongly suggests that, in the case of Xe/Pt(997), the rows observed by He scattering adsorb at the lower step edge. First, the decrease of intensity due to complete row adsorption is small at grazing incidence indicating that the terrace which contributes also to the macroscopic specular reflection is not completely blocked. In certain geometries the first row peak is even more intense than the reflection from the clean surface.

Second, if the first row would be adsorbed on top of the step the row would cast a shadow which will not allow the observation of the repulsive part of the Xe-He potential of the second row at the bottom of the step. It is the strong corrugation of the repulsive potential and not a much weaker corrugation of the attractive part of the potential which determines the detectability of ordering in the rows.

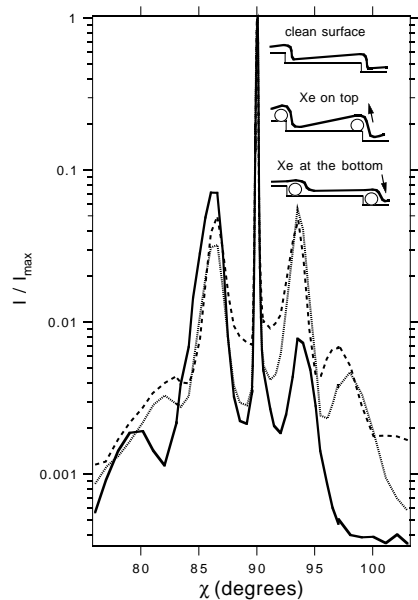


Figure 6.3: Diffraction peaks of orders $n = -5$ (left) to $n = -1$ (right) for the clean Pt(997) surface (solid line), and for a surface on which one row (dashed line), and two rows (dotted line) of Xe were adsorbed at 45 K. Row completion was determined from the intensity maxima obtained in measurements like figure 6.1. For an incident angle of $\theta_i = 51.5^\circ$ the total scattering angle $\chi = \theta_i + \theta_f$ was varied. With $\lambda_{He} = 1.07 \text{ \AA}$ the center peak at diffraction order $n = -3$ is sharp. Inset: Shift of the effective terrace plane seen by the beam for the three indicated cases.

Third, the analysis of diffraction intensities allows to obtain information on the position of adsorption. The clean Pt(997) surface exhibits a diffraction pattern which is described by a lattice function times an form factor function (see section 3.3.2). The first is determined by the surface periodicity leading to Dirac peaks of different diffraction orders. With increasing distance from the Bragg conditions of the three-dimensional

Pt crystal lattice these peaks broaden due to the finite terrace width distribution. The integral intensity of different diffraction peaks is determined by the form factor function which is in the simplest case approximated by the Fourier transform of a single plain terrace. Figure 6.3 shows the diffraction intensities for a clean surface and for a surface after adsorption of one and two rows. It is evident from these measurements that the form factors for the completed rows are similar and that in comparison to the clean surface both are shifted towards larger scattering angles. In this non-grazing incidence geometry the second row becomes visible even if the first row would be adsorbed on top. The small difference between the form factors for one and two Xe rows thus suggests that the second row adsorbs in a similar geometry as the first row. The shift of these form factors with respect to the clean surface reflects a tilting of the effective repulsive potential towards the terrace plane. As shown in the insets in figure 6.3, this behavior also supports adsorption at the bottom of the step. For adsorption on top of the step the repulsive part of the Xe-He potential will increase backscattering towards lower exit angles while in addition the He beam refraction leads to increased terrace bending which still increases the shift. In contrast, the adsorption at the bottom of the step may reduce the terrace bending and can explain an increased scattering towards larger exit angles.

Fourth, the STM study indicating decoration on top of isolated steps [81] demonstrates that the Xe atoms form rather discontinuous nuclei. Specifically the STM image taken after Xe adsorption at higher temperature (30 K) which corresponds rather to our adsorption conditions (> 40 K) indicates the formation of quite incomplete “pearl-chains”. The observation of He intensity maxima, however, requires the growth of dense and continuous rows.

In the following sections (Sections 6.3, 6.4 and 6.5) a detailed theoretical analysis of the sub-monolayer growth of Xe/Pt(997) is presented. In Section 6.6 the discussion of experimental results will be resumed in comparison with the results obtained for the model.

6.3 Interaction potentials

6.3.1 Adsorbate-substrate interactions

As far as the interaction of rare gases with metal surfaces is concerned, difficulties are usually encountered in finding simple additive potentials which lead to results consistent with experimental data. For the Xe-Pt(111) system, a lot of gas-surface potentials [82–89] have been used to test the accuracy of calculated quantities when compared to the available data including thermodynamic measurements, equilibrium and dynamic properties of adsorption, thermal desorption, trapping probabilities, and scattering measurements. Black and coworkers [86] used a number of different Pt/Xe corrugations without finding

a Xe-Pt pair potential which simultaneously fits the experimental corrugations and the binding vibration frequency of xenon. Tully and coworkers [82] studied also the accuracy of various pairwise potential forms (Lennard-Jones or Morse expressions) to describe the trapping dynamics of Xe on the Pt(111) surface. Their flexibility was a required condition to recover the experimental corrugation and Xe-Pt(111) surface binding energy. Bethune, Barker and Rettner [88] constructed a Xe-Pt potential from atom-atom sums which reproduces quite well the available experimental data but they had to attribute a surprisingly small radius to the Xe atom.

Gottlieb and Bruch [83] proposed an effective interaction model for the system Xe/Pt(111) which reproduces the observed structural properties of the uniaxial incommensurate solid phase below 60 K. It consists of a Fourier amplitude representation for the lateral variation of the holding potential and a Lennard-Jones pair potential for the Xe-Xe interactions. The sign of the Fourier amplitude V_g discriminates the adsorption sites corresponding to atop and hollow Xe positions, but the barrier to lateral Xe motion was much smaller than the value inferred by experiments [67, 78]. The distinction between atop and hollow adsorption sites has been investigated and local density functional theory applied to Xe adsorbed on small Pt clusters [90] showed that the equilibrium site would correspond to the atop position. Barker, Rettner and Bethune [89] then defined the Xe/Pt(111) interactions in terms of an empirical potential energy function represented as a sum of non-spherical pairwise additive contributions with an additional contribution which describes the interaction with the delocalized conduction electrons in the metal. This potential was consistent with a wide range of dynamic and equilibrium experimental data and it led moreover to atop adsorption sites for Xe and to a Xe-surface distance about 3.3 Å, reasonably close to the values calculated from *ab initio* [90] or estimated from experiments [85].

While the second species of potentials seem to be more accurate than the pair potentials for a comparison with most of the experimental data, they contain a non local contribution schematized either by the Fourier amplitude describing the metal corrugation or by an exponential term function of the position of the local average surface which mimics the interaction with the delocalized metal conduction electrons. However, close to the step, such a contribution becomes invalid due to the singularity the defect creates at the surface. Therefore, either we can built a potential form containing a non local parameterized contribution which accounts for the presence of the step or we go back to pairwise potentials which do not display such a drawback. A detailed experimental information on the Xe adsorption close to the step is clearly lacking and prevents a multiparameter fit of the non local contribution. Here, we thus consider the potential form discussed by Bethune et al. [88] because these authors calculate the adsorption energy of Xe in the vicinity of a close-packed step edge and test its adequacy to predict desorption rates. The interaction Xe/Pt surface is derived from a Xe-Pt pair potential with param-

eters adjusted to fit the experimental values of the perpendicular vibrational frequency of Xe above the surface, the surface corrugation and the adsorption well depth. These three latter quantities will play a dominant role in the calculations developed here. We will discuss the consequences of our potential choice on the interpretation of results in Section 6.5.

The adsorbate-substrate potential is thus written as

$$V_{AS} = \sum_i \left(A e^{-\alpha R_i} - \frac{C_6 F(R_i)}{R_i^6} \right) \quad (6.1)$$

where R_i defines the distance between the adatom and the i th substrate atom. The first term represents the repulsion and the second contribution characterizes a damped dispersion interaction. The damping function $F(R)$ has the form used by Aziz and Slamann [91] for the Xe-Xe potential

$$F(R) = \begin{cases} 1 & \text{for } R \geq R_C \\ e^{-\left(\frac{R_C}{R} - 1\right)^2} & \text{for } R < R_C \end{cases} \quad (6.2)$$

For the parameters occurring in Eqs. (6.1) and (6.2), Bethune et al. [88] used $A=55.64$ eV, $C_6 = 45.98$ eV \AA^6 , $\alpha=3.5$ \AA^{-1} with the cutoff distance $R_C = 5.36$ \AA . These values give a potential depth, a corrugation and a perpendicular frequency which are fairly consistent with the experimental results of Kern et al. [67, 78].

6.3.2 Adsorbate-adsorbate interactions

The interaction potential within the adsorbate is represented by a sum of pairwise atom-atom Lennard-Jones potentials

$$V_{AA} = 4\varepsilon \sum_{k=6,12} \sum_{ij} \frac{(-1)^{k/2} \sigma^k}{R_{ij}^k} \quad (6.3)$$

where R_{ij} characterizes the instantaneous distance between the i th and j th adatoms. The values of the parameters ε and σ are equal to 24.9 meV and 3.885 \AA , respectively [92]. Note that other contributions should be added to Eq. (6.3) in order to account for non additive three body contributions, substrate mediated interactions and induction phenomena [83]. These contributions could provide corrections to the interaction potential; indeed it was shown [93, 94] that slight differences between the calculated and experimental lateral energies can arise from consideration of these additional interactions. However, the single potential given by Eq. (6.3) reproduces well the dynamic properties of the Xe adlayer adsorbed on other metal such as Cu [95], and we thus disregard the influence of these small contributions for which accuracy remains questionable.

6.4 Equilibrium configurations for xenon

6.4.1 General

The first step in our investigation is the determination of the stable adsorption sites for the Xe atoms on the Pt(997) surface at 0 K. Let N be the number of such adatoms on a terrace, a gradient minimization procedure is used to calculate the equilibrium potential energy $V_{AS} + V_{AA}$ as a function of the $3N$ degrees of freedom of the adsorbate. When we consider a single Xe atom adsorbed on the vicinal surface, we get information on the holding potential V_{AS} in the stable adsorption site and the potential map $V_{AS}(X, Y)$ parallel to the surface. This information is then used to define the best strategy for studying the Xe growth, i.e. to determine whether xenon forms two dimensional islands or three dimensional aggregates on the Pt(997) terrace. While computation times are reasonably small for values of $N \leq 10$, it becomes necessary to limit the number of degrees of freedom for larger N values, using symmetry arguments and informations provided by the potential map $V_{AS}(X, Y)$.

6.4.2 Results

Single Xe adatom

Figure 6.4a represents the minimum potential energy map experienced by a single Xe atom above the (997) Pt surface. The main characteristics determined here are close to those obtained by Bethune [88] for the perfect surface. On a terrace, the most stable Xe site is the hollow site, i.e. when the rare gas atom lies above the center of the regular triangle formed by three nearest neighbor Pt atoms. The rare gas atom lies 1.8 \AA above the surface with a corresponding bonding energy of -255 meV . This surprisingly low value for the equilibrium height has been already discussed [88]. The average corrugation is 27 meV , a value which is consistent to the experimental one (30 meV) found by Kern et al. [67, 78]. The saddle point of the potential surface is the bridge position between adjacent Pt atoms.

Near a step, the Xe adsorption is modified since the potential valley perpendicular to the step direction exhibits a barrier on the upper terrace preventing the atom diffusion downstairs, and on the lower terrace a trapping well deeper than the well obtained in the middle of a terrace. The minimum energy in the trapping site is equal to -352 meV . This value is 1.4 times larger than for the adsorption on the terrace as a result of the increased coordination number of the adatom (roughly 5 for an atom close to the step instead of 3 on the terrace) which enhances the potential by a factor of about $5/3$. In contrast, the Xe atom at the top of the step experiences a maximum potential energy equal to -130 meV . The influence of the step on the potential valley (trapping or chasing)

Figure 6.4: (a) Equilibrium potential energy surface $V_{AS}(X,Y)$ (in meV) experienced by a single Xe atom adsorbed on both sides of a step; (b) Diffusion valley for a Xe atom moving perpendicular to the step. The mean potential increment due to the influence of the step is drawn using dotted lines.

extends over about two interatomic Pt-Pt distances, i.e. two rows of atoms parallel to the step. At the bottom ($Y \leq 0$), we clearly discriminate two different adsorption wells; one which characterizes the first row of equilibrium sites parallel to the step ($Y = -\frac{\sqrt{3}}{2}a$) at -352 meV while the sites in the second row ($Y = -\sqrt{3}a$) are less stable with an energy value of -260 meV. Beyond the second row, one finds still a small increment of the energy (figure 6.4b) superimposed to the oscillations which characterize the corrugation of the terrace. Analogously, at the top of the step ($Y \geq 0$) two different adsorption sites close to the step have higher energies than perfect terrace sites with the corresponding values -226 and -250 meV for the first and second rows, respectively. Beyond this distance, the energy increment becomes vanishingly small.

Xe growth on a terrace.

The minimization calculations at 0 K for several adatoms show that the lateral potential remains in general weak when compared to the corrugation characterizing the holding

Figure 6.5: Equilibrium geometry of Xe atoms adsorbed at various coverages on a confined terrace of Pt(997). Upper terrace along the X axis and lower terrace along X' . The hatched circles schematize the Xe atoms ; (a) ordering in the first row ; (b) two rows geometry ; (c) layer completion on the confined terrace with the $(\sqrt{3} \times \sqrt{3})R30^\circ$ geometry.

At this stage, let us call $\{(l, m)\}$ the set of available adsorption sites. Each (l, m)

couple characterizes the m th site belonging to the l th line parallel to the step direction. A terrace is thus defined by the row number $l = 1, \dots, 8$ and the intrarow site number $m = 1, \dots, \infty$, since there are 8 rows parallel to the step which each contain an infinity of sites. The holding energy of each site (l, m) is labeled V_{lm} which reduces to V_l since we have shown that each site in a given line has the same energy, namely, $V_1 = -352$, $V_2 = -260$, $V_{i=3,6} = -255$, $V_7 = -250$ and $V_8 = -226$ meV. The lateral energy γ between two nearest neighbor Xe atoms is significantly smaller and equal to -22 meV.

For a coverage less than the completion, the adatoms do not adsorb at the top of the step because the Xe-Xe interactions cannot compensate the holding energy difference in this configuration, when compared to the adsorption on the lower terrace. Moreover, the nearest neighbor distance between two Xe atoms belonging respectively to the upper and lower terraces is larger than the Xe-Xe distance ($a\sqrt{3}$) on a terrace. As a consequence, we can neglect the interactions between Xe atoms belonging to adjacent steps and assume that the adsorption phenomena on a terrace is independent of what happens on another terrace.

To end this paragraph, we will make two main comments on these results. First, the occurrence of the commensurate $(\sqrt{3} \times \sqrt{3})R30^\circ$ Xe geometry is the consequence of the form of the selected potential for V_{MS} . Indeed, the rather large corrugation it gives is consistent with the existence of commensurate rather than incommensurate structures. Decreasing arbitrarily the surface corrugation would favor the incommensurate structure. Second, the large row number on the Pt(997) terrace (eight with the commensurate structure) is the result of the small Xe-step distance (2.4 Å) displayed by this potential, a drawback already discussed for the value of the height of Xe above the surface. Increasing reasonably the Xe step distance would decrease the row number to 7. Therefore, to be consistent with our potential choice, we will study the Xe growth at finite temperature within the scheme of the commensurate $\sqrt{3} \times \sqrt{3}$ geometry. Nevertheless, we will discuss how the model is quantitatively (but not fundamentally) modified by changing the corrugation and the Xe-step distance.

6.5 Structure growth at finite temperature

Using information on the equilibrium arrangement of the Xe adatoms, we consider now the influence of temperature on the adsorption process. More precisely, we study the coverage change with the chemical potential $\mu(p, T)$ of the Xe gas phase; p and T are the gas pressure and temperature, respectively. We use a grand-canonical distribution to describe the thermodynamic properties of the Xe system which accounts for the exchange of Xe atoms between the gas state and the adsorbate state. The metal is assumed to be rigid and undeformed.

6.5.1 Ideal lattice gas model

As the lateral potential remains weak when compared to the holding contribution, we first assume a ideal lattice gas model to describe the adsorbate/substrate system. Within this approach, we associate to each adsorption site a probability 0 or 1 to be occupied by a Xe atom. We then use results of Section 6.4.2 and define an exclusion surface S_e for each site equal to $S_e = 3\pi a^2$, since the nearest neighbor distance between sites is $a\sqrt{3}$. Note that we do not take into account the singularity of the first row growth. Indeed, we have seen in the previous section that at 0K the atoms inside the first row are spaced by a distance $2a$ instead of $3a$ in the other rows. As a consequence, the density inside the first row would be different from the others. But, at finite temperature, we are more concerned by a kinetic problem than a static one and it thus appears more realistic to assume that all the atoms are equally average spaced.

The grand partition function $\Xi(\mu, T)$ is written as a simple product of the partition functions associated to any site, as

$$\Xi = \prod_{l,m} \left[1 + e^{-\beta(V_{l,m}-\mu)} \right] \quad (6.4)$$

The grand potential $J = -\beta^{-1} \ln \Xi$ allows us to express the mean number $\bar{N}_{l,m}$ of Xe atoms which occupy the (l, m) th site as a fermion-like occupation function

$$\bar{N}_{l,m} = \frac{1}{\left[1 + e^{\beta(V_{l,m}-\mu)} \right]} \quad (6.5)$$

The mean coverage θ of a terrace, defined as the ratio of $\bar{N}_{l,m}$ and of the available adsorption site number N_S , is thus given as

$$\theta(\mu, T) = \frac{1}{L} \sum_{l=1}^L \theta_l(\mu, T) = \frac{1}{L} \sum_{l=1}^L \frac{1}{1 + e^{\beta(V_l-\mu)}} \quad (6.6)$$

where L is the number of Xe rows on the terrace and $V_{l,m} = V_l$ whatever m (Section 6.4). θ appears as a sum of the coverages $\theta_l(\mu, T)$ per row.

The behavior of the adsorption isotherms $\theta_T(\mu)$ for various temperatures leads to information on the Xe growth process on a confined terrace. The shape of $\theta_T(\mu)$ is formed by successive steps which are more or less apparent, depending on the line number l and on temperature. Each step corresponds to the growth of a row while each terrace represents the stability range of a completed row.

Let us then define the isothermal compressibility K_T of the adsorbate as

$$K_T = -\frac{1}{A} \left(\frac{\partial A}{\partial \phi} \right)_T \quad (6.7)$$

where ϕ is the adsorbate spreading pressure and $A = N_S S_e \theta$ characterizes the adsorbate surface. After straightforward manipulations, we can write

$$K_T = N_S S_e \chi(\mu, T) = N_S S_e \left(\frac{\partial \theta}{\partial \mu} \right)_T \quad (6.8)$$

and find the expression for $\chi(\mu, T)$ using Eq. (6.6) as

$$\chi(\mu, T) = \frac{\beta}{4L} \sum_l \frac{1}{\cosh^2\left(\beta \frac{V_l - \mu}{2}\right)} \quad (6.9)$$

The function $\chi(\mu)$ appears as a set of Dirac peaks located at the values $\mu = V_l$ ($l = 1, 2, \dots, 8$) for $T=0$ K. These peaks broaden at finite temperature with a full width at half height equal to $\Delta = 4 \arg \cosh(\sqrt{2}) k_B T \simeq 3.52 k_B T$. The condition for peak resolution indicating row-by-row growth leads us to define a criterion for temperature which can be written as

$$T_{r_l} = \frac{|V_{l+1} - V_l|}{3.52 k_B} \quad (6.10)$$

where T_{r_l} characterizes the maximum temperature required to observe the occurrence of the l th Xe row. In other words, for $T \leq T_{r_l}$, we can distinguish the ordering of the l th row with respect to the $l+1$ th one. Beyond this value, $T > T_{r_l}$ every adsorption site on the l th or $l+1$ th row is equivalent for Xe atoms.

6.5.2 Mean field Hamiltonian Ising model

To improve the previous model which is valid within the assumption of vanishing lateral interactions between Xe atoms, we use a conventional two dimensional Ising model with an Hamiltonian H defined as

$$H = \sum_{l,m} V_l \sigma_{l,m} + \gamma \sum_{l,m,l',m'} \sigma_{l,m} \sigma_{l',m'} \quad (6.11)$$

where $\sigma_{l,m}$ characterizes the atom number occupying the (l, m) th adsorption site and γ is the lateral interaction between two Xe atoms adsorbed in nearest neighbor sites. Let us then define an effective mean potential experienced by a Xe atom trapped in the (l, m) th site as

$$\bar{V}_{l,m}^* = V_l + \gamma \sum_{l',m'} \bar{\sigma}_{l',m'} \quad (6.12)$$

The sum is restricted to the coordination number associated to a given site (l, m) and $\bar{\sigma}_{l',m'}$ describes the mean occupation of the (l', m') site. The grand partition function Ξ

Figure 6.6: Coverage θ vs chemical potential μ for three characteristic temperatures $T = 10$ (a), 30 (b) and 60 K (c). Note the stepwise behavior of the growth and the progressive disappearance of this feature when T increases.

In figure 6.6, we give the behavior of the coverage as a function of the chemical potential μ for three characteristic temperatures (Eq. (6.13)). At low temperature ($T=10$ K),

figure 6.6a exhibits the striking discrete stepwise behavior of the coverage, already mentioned in the lattice gas model. There are six significant θ values defining slope breakings in the curve at $\frac{l}{8}$ with $l = 1, 2, 3, 4, 7$ and 8 . These particular values of the coverage correspond to the completion of a given row. This means that we can distinguish independently the growth of these rows. By contrast, for the intermediate rows of the terrace ($l = 5, 6$ and 7), the adsorption sites are equally probable and the site occupation is random, irrespective of the row number. At intermediate temperature ($T=30$ K), the number of distinct slope breakings for the curve $\theta(\mu)$ decreases and only the rows with $l = 1, 2, 3, 7$ and 8 can be distinguished (figure 6.6b). At higher temperature ($T=60$ K), the discrete growth can occur only for the first two rows close to the step where the potential increment is significantly large. For the other sites, the coverage increases quasi-continuously with μ (figure 6.6c) indicating randomization. At $T=100$ K, only the first row growth process can be observed in the curve (not drawn).

To interpret the occurrence of the two types of growth processes on the confined terrace: the discrete row-by-row growth and the random growth, one may note that the resulting behavior of the coverage as a function of the chemical potential appears to be similar in the two approaches (Sections 6.5.1 and 6.5.2). Thus, though the lateral interactions play a significant role in these processes, they do not alter the main features. The competition between the potential increment due to the upper and lower steps as experienced by the Xe adatoms confined on the terrace and the thermal energy β^{-1} is responsible for this phenomenon. Indeed, when the potential increment $|V_{l+1} - V_l|$ is significantly larger than β^{-1} , the energy that a Xe atom gains (or loses) by adsorbing on sites of a given row tends to favor the inter-row competition and thus the discrete row growth. In contrast, when $|V_{l+1} - V_l|$ is vanishingly small, the adsorption sites become equiprobable and the growth is random.

There are two main differences between the ideal lattice gas model and the mean field approach. Firstly, as seen in figure 6.6, the chemical potential μ_l connected to the occurrence of the l th row, is not equal to V_l , as it is in the lattice gas approach. Secondly, the temperatures T_r listed in Table I for which the discrete row growth can be distinguished, are significantly different for the two models. These two features are closely related although it is not straightforward to understand their origin since only a numerical procedure can allow us to solve this problem. From Eq. (6.13), μ_l satisfies the equation

$$\frac{\mu_l - V_l}{2\gamma} = \frac{1}{2} \sum_{i=l-2}^{l+2} \frac{1}{1 + e^{\beta(V_i - \mu_l)}} + \frac{1}{2} \sum_{i=l-1}^{l+1} \frac{1}{1 + e^{\beta(V_i - \mu_l)}} - \frac{1}{1 + e^{\beta(V_l - \mu_l)}} \quad (6.14)$$

and it thus depends on the relative magnitudes of the potentials $\gamma, \Delta V_1 = V_l - V_{l-1}$ and $\Delta V_2 = V_l - V_{l-2}$ and of the thermal energy β^{-1} . For instance, we present in figure 6.7, the situations occurring for the 3rd and 5th rows. The straight line with negative slope

Figure 6.7: Graphical resolution of Eq. (6.14) showing the dependence of the critical chemical potential μ_l vs temperature. (a) For a well resolved plateau corresponding to the third row completion. (b) For a very limited plateau corresponding to the fifth row (see the text).

$\frac{1}{2\gamma}$ ($\gamma \leq 0$ means attractive lateral interactions between Xe atoms) intersects the curve defined by the right part of Eq. (6.14) and gives the root μ_l of Eq. (6.14). For the 3rd row (figure 6.7a), we see that the chemical potential is almost independent of T within the range of temperature considered here. Indeed, the straight line intersects a plateau of the curve leading to the situation for which $\Delta V_1 \leq |\gamma| \leq \Delta V_2$; μ_3 is then approximately equal to $V_3 + \gamma$. By contrast, for the 5th row (figure 6.6b), one has $|\gamma| \geq \Delta V_1$ and $|\gamma| \geq \Delta V_2$ and μ_l depends drastically on the temperature since the straight line intersects a nearly vertical line connecting two plateaus. No analytical solution can be determined in this case. For the other rows, the analysis is still more intricate since it depends on the length of the plateau, but the solutions μ_l are always lower than the V_l values determined in the ideal lattice gas model. Note that even if the lateral interaction characterized by $|\gamma|$ is small when compared to the holding potential, it propagates the step effect to all the rows. At zero temperature, we therefore see the growth of all the rows, with the mean field Hamiltonian Ising approach while it is not the case in the ideal lattice gas model for which the rows $l = 3$ to 6 have the same holding potential.

Table I : Temperatures T_r (K) indicating a row-by-row Xe growth

row	lattice gas model		Ising model	
	$\sqrt{3} \times \sqrt{3}$	$\sqrt{3} \times \sqrt{3}$	$\sqrt{3} \times \sqrt{3}$	Incommensurate
1	296		130	155
2	23		90	90
3	0		45	5
4	0		20	5
5	0		2	-
6	16		5	
7	79		85	
8	-		-	

As a consequence of the negative shift of the μ_l roots of Eq. (6.14) with respect to V_l , the temperatures T_r obtained in the Ising approach are significantly different from those obtained in the lattice gas model (Table I). More specially we see that the third, fourth and fifth rows can be distinguished below temperatures equal to 45, 20 and 2 K, respectively whereas they are not discriminated in the ideal lattice gas approach. The temperatures T_r can be greater or smaller than those obtained by the lattice gas depending on the relative values of γ , T , ΔV_1 and ΔV_2 . The first row can be distinguished up to 130 K while the second row occurs for T less than 90 K. The 6th row disappears for a temperature higher than 5 K. The last row ($l = 8$) corresponds to the completion of the terrace which is obtained when the 7th row is filled; this is observed for T less than 85 K. The mean field model discussed so far describes the probability of finding an atom in each row for a given total coverage. However, the lateral interaction in the adsorbate can give rise to different characteristic structures of the adsorbate step edge which we will briefly sketch. Preliminary Monte-Carlo simulations with potentials similar to one given in Section 6.3 demonstrate that at coverages corresponding to less than four complete rows the adsorbate step edge rowing becomes random with increasing temperature. At higher coverages, the adsorbate begins to exhibit a zig-zag step edge with straight sections parallel to close packed directions in the $(\sqrt{3} \times \sqrt{3})R30^\circ$ structure. The formation of close packed adsorbate step edges may thus drive thermally induced faceting of the growing front.

6.6 Discussion

In this section we compare the measurements and the results for the potential model presented in the previous sections. As already discussed in the experimental section the coverage dependent reflected He intensity exhibits at 40 K surface temperature two maxima which correspond to the first and the second completed rows (figure 6.1). For the

potential used in the theoretical part, preferential Xe adsorption is obtained at the lower step edge in agreement with the experimental result discussed in Section 6.2. The model predicts a Xe-Xe distance in the first row of 5.5 Å. This value was found experimentally in a LEED study by P. Trischberger and coworkers [80]. The quasi-hexagonal incommensurate structure with 5 rows in a monolayer could not be reproduced by the calculation. The difference between calculation and experimental results indicates that the Xe-Xe interaction (leading to an incommensurate structure) and the step-Xe interaction (which leads to the formation of close packed Xe rows parallel to the steps) are more important than the corrugation of the Pt-Xe potential on the terrace.

The temperature dependence of the growth process was studied experimentally for a series of surface temperatures above 40 K shown in figure 6.1 (see also chapter 4). From these measurements, lower limits of the critical temperatures for the discrete row growth can be obtained. At a gas pressure of 3×10^{-8} mbar, Xe exhibits multilayer growth below a substrate temperature of 57 K. Below 91 K equilibrium with the gas phase occurs only after the completion of a full monolayer [39]. Here, ordered rows are formed only in a transitory state during continuing adsorption. The first row peak in figure 6.1 is visible up to 90 K. At 100 K the intensity reaches this peak and then stays constant indicating that the equilibrium between the complete first row and the gas phase is reached. The second peak becomes smeared out above 80 K. Although up to 100 K adsorption continues after the formation of the first row the second row does not appear as a distinct peak and thus is not completed before the third row begins to grow. Discrete second row formation is thus observed up to 80 K.

The experimental estimates of these characteristic temperatures T_c and the results for the Ising model (Table I) agree nicely. As a general trend, the experimental values are lower indicating that only lower limits for discrete row growth are obtained. One has to bear in mind that in the experiment the three-dimensional Xe pressure is constant and coverage increases as a function of time. The experiments were not performed in equilibrium between gas phase and adsorbate which would correspond to constant chemical potential conditions. Specifically in the case of the first row where the difference between experimental value (100 K) and model (130 K) is large, an ordered row may still form at higher temperature if an increased ambient pressure provides a sufficiently high coverage. A second aspect is important for the comparison between experiment and model: in an experiment discrete rows may not form even though they correspond to equilibrium states because the kinetics of the growth process will play a role e.g. at low temperature or high deposition rate. Taking into account the difference in the monolayer structure between calculation and experiment the agreement in the thermodynamic data is fairly good. The structural details do not appear to be essential in determining the thermodynamics of growth in this system.

Our calculations for the Xe/Pt(997) system can also be compared to numerical calcula-

tions performed by Merikoski *et al.* [66]. In their paper, they consider a linear dependence of the potential energy increment due to the step as a function of the distance with respect to the step. They also assume that the lateral interaction (γ parameter) is larger than the holding potential. At low temperature, they obtain a discrete growth for all the rows of the terrace because the step potential value is different for each row. But, due to the linear dependence of the holding potential, they determine a single characteristic temperature T_r . Our model differs fundamentally from this linear model since (1) the lateral interactions are weak when compared to the holding energies -this is a specificity of the Xe adsorption on Pt- and (2) the energy increment is rather exponential than linear, as shown in figure 6.4b. The first condition leads us to take advantage of the mean field approach which should not be valid for large γ values, i.e. for other adsorbates and/or substrates. The second situation appears clearly much more physical since non-linear behavior is responsible for the occurrence of several critical temperatures, as verified from the comparison with experiments.

Improvements of the calculations could be done on the accuracy of the values of the T_r temperatures by using a transfer-matrix method [66] to solve the self consistent equation (Eq. (6.13)). The mean coverage would be determined by overcoming the approximations tied to the mean field Hamiltonian in the Ising model. But the main point of discussion is the influence of the potential choice on the model developed here to interpret the row-by-row growth of Xe/Pt(997). The Xe-Pt potential can account for the observed geometry of the first row with a mean Xe-Xe distance along the step equal to 5.54 Å. If the corrugation was arbitrarily decreased down to zero on the terrace, we would obtain a mean distance inside the first row considerably smaller ($\simeq 4.4$ Å) imposed by the lateral interactions in the incommensurate phase. The present potential with the large corrugation leads to the stable $(\sqrt{3} \times \sqrt{3})$ commensurate structure which is experimentally observed on larger terraces and at temperature higher than 60 K. Moreover, STM measurements [96] on Xe/Pt(111) have evidenced a 30° rotated structure attached to the steps. This structure - most probably the $(\sqrt{3} \times \sqrt{3})R30^\circ$ structure - is observed in regions where the step is rough or the step direction deviates sufficiently from the $(11\bar{1})$ direction. The mean Xe-Xe distance in this structure is slightly larger (4.8 Å) than for the incommensurate phase inferred from TEAS experiments with an intra-row Xe distance of 4.1 Å and an inter-row distance of 3.87 Å, leading to an average Xe-Xe distance equal to 4.3 Å. A type of such a quasihexagonal structure for which the (997) terrace could accommodate 5 Xe rows is shown in figure 6.8a. The potential increment, due to the step and counterstep, experienced by an adatom on a terrace without corrugation is presented in figure 6.8b. The equilibrium distance between the first Xe row and the step is equal to 2.4 Å. At this distance, the step influence is maximum, then it decreases quickly to vanish around 8 Å while the influence of the counterstep becomes significant above 14 Å. According to the model presented in Section 6.5.2, modified to account for the number of nearest neighbor

Figure 6.8: (a) Quasihexagonal geometry inferred from experiments : five Xe rows with an average Xe-Xe distance equal to 4.3 Å; (b) Potential increment experienced by a Xe atom and due to the step and counterstep vs the distance with respect to the step.

Previously, we mentioned that the potential used here gives furthermore a Xe-Pt distance on the terrace which is small. This latter drawback is also present to lesser extent for the Xe-step distance equal to 2.4 Å. The equilibrium site at the step, with the distance value of 2.4 Å, corresponds to a stable site for the $(\sqrt{3} \times \sqrt{3})$ commensurate phase and for the substrate without corrugation. If we expected larger distances from the step, the next hollow site would be at 4.0 Å; this value appears to be too large when compared to the inferred values from calculations and experiments, within the range 3.0 to 3.5 Å. Thus changing the potential form would result in equilibrium sites at distances ranging between 3.2 Å from the step for atop positions and 4.0 Å for the next hollow positions, which would lead firstly to a geometry change of the confined layer and secondly to a change of the number of rows.

However, we must keep in mind that the major phenomenon which is considered from a theoretical point of view is the thermodynamic description of the Xe ordering during the growth on a confined terrace. We have seen that two main parameters determine the behavior of the row-by-row ordering: the value of the lateral pairwise interaction γ and

the increment of the atom-surface potential ΔV_l as a function of the Xe distance with respect to the step. The first parameter γ is not very sensitive to the Xe-Xe distance within a reasonable range of values: γ takes the values 19, 25 and 22 meV when the Xe-Xe distance changes from 4.1 to 4.4 and 4.8 Å, respectively. The influence of the second parameter ΔV_l appears more difficult to evaluate since the form of the holding potential defines both the slope and the magnitude of the increment ΔV_l ($l = 1, 2, \dots$). What can be said is that the slope is mainly connected to the long range part of the potential which should not be very different for the various potential forms. If the potential well depth at the equilibrium site close to the step is calibrated with the same value, for Xe-step distances equal to 2.4 Å and 3.2 Å for instance, the increment magnitude is also expected not to change in a dramatic way, being only a scale translation on the distance. As a consequence, the calculated row-by-row temperatures T_r should not be fundamentally modified. Note however that if the Xe-step distance increases, the number of rows on the confined terrace should decrease.

6.7 Summary

The discrete row growth of Xe/Pt(997) which was observed by grazing incidence He scattering was modeled for realistic adsorbate-substrate and adsorbate-adsorbate interaction potentials. A discrepancy is found for the Xe monolayer structure which is obtained to be commensurate in the calculation while He diffraction measurements rather indicate an incommensurate structure. The discrepancy is probably due to an overestimated value of the corrugation given by the selected potential. In theory and experiment the attachment of the rows takes place at the bottom of the steps and both agree in the Xe-Xe distance value inside the first row adsorbed at the step. The temperatures of complete row formation are in nice agreement with the experimental results, thus indicating that the potential corrugation is not the dominant parameter involved in the row formation process. In fact, it is shown that the major effect is the shape of the potential increment due to the step and counterstep.

Chapter 7

Kr adsorption on Pt(997): experiment

7.1 Introduction

Fundamental interest in two-dimensional systems has motivated investigations of physisorbed rare gas adlayers [97]. They are two-dimensional model systems due to weak adsorbate-substrate interaction. A wide range of experimental [98–101] and theoretical [102–106] studies have been performed on the rare gas adlayers. Most of them have been interested in the structural phase transitions driven by temperature and coverage. The transitions arise from the subtle competition between the adatom-adatom and adatom-substrate interactions. Depending on the dominating effect, the structure can be commensurate or incommensurate [107]. If both interactions are of comparable magnitude, the structural phase transition can be induced by temperature or coverage changes. The real structure is difficult to predict *a priori*, as the adsorbate-substrate and the lateral adsorbate interaction potentials are not exactly known. Chapter 6 has given an illustration of this difficulty in showing the discrepancy between the experimental and theoretical structures of the Xe monolayer on Pt(997).

In this chapter, we present a thermodynamic and structural study of the Kr adsorption on the vicinal Pt(997) surface. The study treats the submonolayer range up to multilayer coverages. The presence of a large step density on this substrate makes the surface an ideal substrate for the investigation of the influence of the steps on growth and morphology of the Kr monolayer, as well as on the adsorption energies of Kr atoms in the 2D-solid and 3D-bulk phases (row, monolayer; multilayer). The Kr/Pt(997) results are compared with Kr adsorption on the “step free” Pt(111) surface [108–111] and with Xe/Pt(997) [39].

7.2 Experimental

The Kr/Pt(997) system is well suited for a TEAS investigation and the present study calls on most of the applications presented in chapter 2:

- The position of the diffraction peaks is employed to determine the periodicity of the top-most surface layer.
- The intensity changes in the diffraction peaks during adsorption and temperature ramps are employed to monitor the ordering at the surface. They allow to determine the growth mode and the phase transitions of the adlayer.

As explained in chapter 4, the step-sensitive $n = 0$ diffraction peak is employed to monitor the order at the step in the submonolayer range and the terrace-sensitive $n \neq 0$ diffraction peaks are employed to monitor the order on the terrace in the monolayer and multilayer range.

The Pt(997) surface is prepared according to the usual procedure (see section 3.3). The obtained surface is clean within the Auger spectrometer sensitivity. Kr is adsorbed on the Pt(997) surface by backfilling the sample chamber with Kr at pressures between 3×10^{-9} and 5×10^{-5} mbar.

7.3 Results

7.3.1 Growth mode

The first information that can be obtained from the TEAS data is the growth mode of the Kr adlayer. It is determined by monitoring the intensity of the substrate diffraction peaks during adsorption. By choosing either a more grazing or a less grazing geometry, it is possible to select the origin of the changes giving rise to the signal variations: steps or terraces.

Figure 7.1 a, which is obtained in the $n = -3$ terrace-sensitive non grazing geometry, exhibits layer-by-layer growth of Kr/Pt(997) until at least the 7th layer. The oscillations are damped mainly due to the large Debye-Waller factor of Kr multilayers. The equidistance of the oscillation maxima even for a large number of layers indicates that the sticking coefficient is constant during the adsorption and allows a precise calibration of the coverage. The maximum corresponding to the first layer is not well marked. It appears only as a shoulder in the initial decay. This is probably due to the large difference in reflectivity between the Kr layer and the Pt substrate (the reflectivity of 1 ML Kr is $\simeq 1\%$ of the reflectivity of the clean Pt(997) surface in $n = -3$), which masks the layer completion.

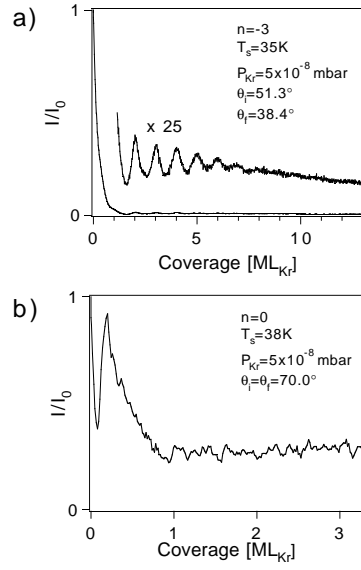


Figure 7.1: Typical adsorption measurements with $\lambda = 0.93 \text{ \AA}$. (a) has been measured in the $n = -3$ diffraction peak and is terrace sensitive. (b) has been measured in the $n = 0$ diffraction peak and is step sensitive.

Figure 7.1 b, which is obtained in the $n = 0$ step-sensitive grazing geometry, shows row-by-row growth for the first row. The reason for the absence of additional row formation during the growth, marked by the absence of additional oscillations in the submonolayer range is twofold:

1. The lower temperature limit of the instrument of about 30 K is probably too high to allow the growth of the next rows to be ordered. Such a disordered growth is theoretically predicted in chapter 6 for Xe and should occur for Kr as well.
2. The finite terrace width distribution induces a desynchronization of the row completion on terraces with different widths. This intrinsically damps the signal oscillations corresponding to the row completion, as will be discussed in section 8.4.

Evaluation of the coverage at the first row peak maximum in several measurements gives a value of $\Theta = \frac{1}{5.2}$ of a monolayer. This is in good agreement with the structure

Figure 7.2: He diffraction patterns of one Kr monolayer at 40 K with $\lambda = 0.93 \text{ \AA}$. (a) is taken in step-down incidence with $\theta_i = 53.8^\circ$. From the first order diffraction peaks, a Kr row periodicity of 3.5 \AA is deduced (see text). (b) is taken with an incidence parallel to the steps and $\theta_i = 59.3^\circ$. An interatomic distance in the rows of 4.0 \AA is deduced. c) possible model of the Kr monolayer structure.

The second information that can be obtained is the monolayer structure. Diffraction patterns taken in two azimuthal directions perpendicular to each other (see figure 7.2 a and b) give the periodicity of the monolayer in these two directions. While the periodicity (a) along the rows is easy to infer from the diffraction pattern with the 1D-Bragg equation ($\sin(\theta_f) - \sin(\theta_i) = n \cdot \lambda/a$), the periodicity perpendicular to the steps is more difficult to extract. In principle, the periodicity is given by the position of the maximum of the form factor, which envelopes the Kr first order diffraction peaks. It can be fitted using the integrated intensity of the diffraction peaks as in section 3.3.2 and the periodicity can be inferred from eq. 3.4. However, the problem comes from the form factor shift discussed

in chapter 3, which introduces an uncertainty in the form factor position. To account for this effect, we have fitted the $m = 0$ form factor, for the left peaks in figure 7.2 a, and corrected the first order form factor position by the shift obtained from $m = 0$. The correction is however only a coarse approximation, as the $m = 0$ form factor maximum is less grazing and thus less shifted than the Kr $m = 1$ form factor maximum. The value of $3.5 \pm 0.05 \text{ \AA}$ obtained in this way thus probably slightly overestimates the distance between the rows. From these results, a quasi-hexagonal structure can be proposed, where the Kr atoms are arranged on the terraces in rows separated by $3.5 \pm 0.05 \text{ \AA}$ with an interatomic distance in the rows of $4.0 \pm 0.05 \text{ \AA}$. The number of Kr rows per average terrace is thus equal to 5.7. Compared to the coverage corresponding to row completion ($\Theta = \frac{1}{5.2} \text{ ML}$), this indicates that the row condenses from the beginning in the structure of the final monolayer. This is different from Xe, where the first two rows grow on Pt(997) in a structure less compact than the completed monolayer (see chapter 6). Figure 7.2 c proposes a model for the Kr monolayer structure on a Pt(997) terrace. The monolayer structure is incommensurate.

7.3.3 Thermodynamics

To determine the phase diagram (figure 7.3 a) of the Kr layer on the Pt(997) surface, we monitored the He intensity in different diffraction peaks as a function of temperature, while the base Kr pressure in the chamber was kept constant. For most pressure values, only the $n = -3$ diffraction order was studied. This peak provides a large intensity, which is necessary for a good measurement statistics as the Kr layer is only weakly reflective. A phase transition is generally marked by a steep intensity change at the transition temperature. An example of a corresponding measurement is given in figure 7.3 b. The monolayer condensation is marked by a steep decrease of the intensity around 72 K, while the multilayer condensation is marked by a steep decrease around 53 K.

The transition temperatures T for various pressures p_{Kr} , allow the construction of the (p_{Kr}, T) phase diagram of figure 7.3 a. However, the definition of the transition temperatures is not obvious. In an idealized theory, a first order transition takes place in an infinitely small temperature range [112] and the He intensity should exhibit an infinite slope at the phase transition. For a vicinal surface, this is not the case: the reason is that, due to the steps, the adsorption energy for the Kr atoms is not constant over a terrace (see chapter 6 and [70]). The phase transition thus takes place by successive temperature steps and the He intensity varies over a finite temperature range. This behavior is particularly important for the monolayer condensation, for which the adsorption energies in the different surface sites exhibit large differences. To obtain reliable results from the He measurements, it is necessary that for each pressure the system exhibits the same coverage and structure at the measured transition temperature. It is possible to assure

Figure 7.3: a) Phase diagram for Kr/Pt(997). I: 2D-gas phase. II: first row condensed + 2D-gas phase. III: 2D-solid phase. IV: 3D-solid phase. b) Example of isobaric He intensity vs temperature measurement. $p_{Kr} = 2.5 \times 10^{-6}$ mbar (see text).

this precondition by measuring the transition temperature always at the same position in the He intensity curves. In two different isobaric He intensity curves, the “same position” is defined as the same relative He intensity with respect to the He intensity obtained with the clean surface [17]. The heat of adsorption that will then be deduced from the slope of a phase boundary is thus an isosteric adsorption heat related to the coverage at the selected position of the curve. The positions employed in this study are defined by arrows in figure 7.3 b for the monolayer and multilayer transitions. The choice has been made to measure the temperature at the bottom of the steep decrease for the monolayer transition and in the middle of the decrease for the multilayer. For the monolayer transition, it corresponds to a coverage slightly below one complete monolayer (~ 85 %) and for the multilayer transition, it corresponds to a coverage larger than 2 monolayers. These coverage estimates are made by comparison of the He intensity at the transition temperature with the He intensity during adsorption measurements of the same type as in figure 7.1 a.

One can distinguish in the phase diagram of figure 7.3 four regions corresponding to four different phases of the system. Phase I is the 2D-gas phase on the surface in equilibrium with the 3D gas phase in the chamber. Phase II corresponds to the decoration of the steps by one Kr row while the 2D-gas phase remains on the terraces. Crossing the limit between phase II and III, the first Kr monolayer condenses (i.e. 2D-solid phase). Finally, the multilayer adsorption is reached in the region IV (i.e. 3D-solid phase).

From the slopes of the phase boundaries, one can deduce the isosteric heat of adsorp-

tion of the Kr adlayers in the different phases, using the Clausius-Clapeyron equation:

$$q_{st} = -k_B \left. \frac{\partial \ln p}{\partial (1/T)} \right|_e \quad (7.1)$$

From a fit we obtain heats of adsorption of 210 ± 10 meV in the first monolayer and 120 ± 20 meV for multilayer adsorption. A few measurements have allowed to determine the transition temperature of the first row condensation (I-II boundary). However, as in the $n = -3$ diffraction peak this transition is only present as an inflection point, it is difficult to define the precise position reliably. This leads to the large error bars on the derived adsorption energy in the first row of 190 ± 60 meV. This value should indeed be larger than the heat of adsorption in the first monolayer, because the adsorption energy at the step is larger than on the terrace sites.

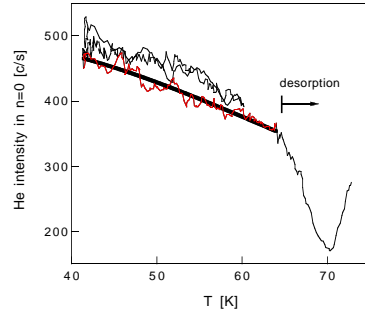


Figure 7.4: reflected He intensity in the macroscopic specular diffraction peak ($n = 0$) as a function of temperature for a coverage of 1 row. Thick line: fit (see text).

The adsorption energy in the first row can be independently determined by another measurement. The excess binding energy in the first row compared to the rest of the terrace can be deduced from the behavior of the He intensity in the grazing incidence $n = 0$ diffraction order. The experiment is performed as described in section 4.3. Again, care had to be taken to avoid desorption which occurs above 65 K indicated by the intensity drop in figure 7.4. Assuming a two energy levels model with an adsorption energy equal to zero on the terrace and ΔE in the row, the intensity behavior can be modeled as discussed in chapter 4. The fit of the data with eq. 4.1 is not very sensitive to the choice of σ . For a reasonable value of σ equal to 5 Å, we obtain a value ΔE equal to 30 ± 5 meV.

7.4 Discussion

The growth of Kr on Pt(997) is similar to the growth of Xe on Pt(997) (see chapter 6) with an overall shift towards lower temperatures.

The structure of the Kr monolayer on Pt(997) is incommensurate and different from the (5×5) R0° HOC structure observed at high coverage on Pt(111) [111]. The nearest neighbor distance of 4.0 Å is comparable to the HOC structure, but the orientations differs by 30°. This is probably induced by the presence of the step, which pins the Kr layer orientation. As evidence for the first row growth is given in figure 7.1, we may reasonably exclude the blocking of the step sites by impurities (H, CO) to explain this rotation as discussed in [110].

The thermodynamic parameters of the Kr phases exhibit a strong difference to the results on Pt(111). The heat of adsorption of the first Kr monolayer on Pt(997) is obtained as 210 ± 10 meV. This value must be compared to the Kr adsorption energy on Pt(111) of 158 ± 5 meV [108], which is substantially lower. As the interatomic distances in the first Kr monolayer on Pt(997) are comparable to the ones on Pt(111), the difference is unlikely to be due to a dramatic increase of the adsorbate-adsorbate attractive interaction. It is more likely that the adsorption heat increase relates from an increased adsorbate-substrate interaction. The origin of this excess binding energy can however hardly be attributed to the attraction of the step, as calculations for Xe (see chapter 6) show that the excess attraction of the step fades away after two rows. No final explanation is available for the moment, all the more since the adsorption energy difference is not as large for Xe on Pt(997) [39]. The global effect of the different contributions must lead in a subtle manner to the observed structure and adsorption energy for the different species.

A heat of adsorption in the multilayer phase of 120 ± 20 meV has been measured for Kr on Pt(997), which is in good agreement with the heat of adsorption of bulk Kr (120 meV at a mean temperature of 63.2 K) [113].

7.5 Summary

Kr on Pt(997) grows row-by-row until the first row in the submonolayer range and layer-by-layer for a large number of layers in the multilayer range. The Kr monolayer exhibits an incommensurate probably quasi-hexagonal structure with a nearest neighbor distance of 4.0 ± 0.05 Å, which seems to be pinned by the step. The heats of adsorption of the Kr atoms in the different phases have been obtained: 210 ± 10 meV in the monolayer and 120 ± 20 meV in the multilayer. The excess binding energy in the first row has been obtained to 30 ± 5 meV. The structural and thermodynamic results of this study show the strong influence of the substrate on the morphology and thermodynamic properties of the first Kr monolayer. In particular, the adsorption heat in the first monolayer is

significantly larger than for Kr on Pt(111). The origin of this effect is not yet explained. However, it has to be linked to a modified adsorbate-substrate interaction with respect to Pt(111), as the difference disappears for multilayer adsorption.

Chapter 8

Ag growth on Pt(997)

8.1 Introduction

Growth of metal on metal substrate attracts much interest for technological applications. The adsorbate-adsorbate and adsorbate-substrate interaction energies are much larger than for the rare gas systems studied in chapter 6 and 7, and growth is therefore expected to exhibit different features. In order to study the influence of steps on the growth for such a system, Ag on Pt(997) is a good candidate, as Ag is known to grow phase separated on Pt(111) up to 550 K [114]. No alloying occurs below this temperature. The complete first layer is known to be pseudomorphic to the Pt-substrate, and the diffusion processes have been studied quantitatively [7, 115]. Above 550 K, a Ag-Pt surface alloy forms for submonolayer Ag coverages, which is confined in the first layer until Ag desorption at about 900 K [116]. At monolayer completion, the alloy demixes and a phase separated monolayer forms again.

In this chapter, we present a study on the growth of Ag on Pt(997) in a coverage range from submonolayers to multilayers at the temperature range from 200 to 700 K. This study is performed by TEAS, which is extremely sensitive for this kind of investigations. Even small morphology changes on the surface give rise to significant changes in the He intensity. The lack of realistic models for the interaction between He-atoms and vicinal surfaces, shortly discussed in chapter 3, does, however, not allow to extract more than qualitative results from the observations. However, interesting phenomena can be related to the presence of steps.

After a short introduction to the effects responsible for an intensity variation of an ideal diffraction peak during deposition, the growth behavior of Ag/Pt(997) below the alloying temperature is discussed and compared to the growth on Pt(779) in section 8.4.1. The Ag-Pt surface alloying and demixing processes on Pt(997) and Pt(779) are discussed in section 8.4.2.

8.2 Theory: Diffraction pattern of an adsorbate covered Pt(997) surface

During an adsorption experiment, the morphology and the chemical composition of the terrace undergo important changes. This strongly influences the intensity in the diffraction peaks. Their position is rather unchanged if the surface periodicity is not modified. The purpose of this section is to discuss the different effects that may induce intensity changes of the diffraction peaks in ideal condition during deposition. The scattered beams coming from different terraces interfere coherently in these peaks and therefore provide a valuable tool to study the ordering on the terraces. As the $n = 0$ peak cannot be in ideal condition, the arguments do not hold for this diffraction order. The properties of the $n = 0$ diffraction peak have already been discussed in chapter 5.

The first effect to consider is interference. In ideal condition and without adsorbate, all the points of the surface are scattering in-phase and the partial beams originating from the surface interfere coherently. When adding an adsorbate with a different height, the in-phase condition between the points of the surface is no more satisfied and the intensity decreases. The slope of the decay depends on the reflectivity of the adsorbate with respect to the substrate. In case of destructive interference, the more reflective the adsorbate is, the steeper is the slope of the decay. After having reached a minimum, the intensity increases again when the adsorbate partial contribution overtakes the one of the substrate and finally reaches a maximum for a full layer. The last assertion is valid only for 2D-growth, which is *e.g.* observed for Ag on Pt(997).

In relation to the interference effect, the Debye-Waller factor also influences the He intensity during adsorption: it is different for each species and determines the relative reflectivities between substrate and adsorbate.

The second effect is linked to the position of the form factor maximum with respect to the monitored peak. For clean Pt(997), a shift is observed between the form factor maximum and the ideal condition $\phi_i = \phi_f$, calculated from eq. 3.7 (see section 3.3.2). This shift is linked to the potential (attractive or repulsive part) felt by the He atoms near the surface. As this potential is different for each species, the adsorption of atoms with a different electronic structure may change the shift. This is observed *e.g.* for Ag on Pt(997) as can be seen in figure 8.1. In this figure, the diffraction pattern of clean Pt(997) is compared to the pattern obtained for a Ag monolayer in the case where $n = -2$ is in ideal condition. It shows that the diffraction pattern with a Ag monolayer is shifted towards larger scattering angles ($n = -1$ appears, while $n = -4$ decreases) compared to the diffraction pattern for clean Pt. In the inset of figure 8.1, the form factors of both cases have been fitted on the basis of the integrated intensity in the diffraction peaks. For the Ag covered surface, the shift is reduced by about 2° , with respect to the shift of clean Pt(997), which is about equal to 4.5° . This countershift becomes more important

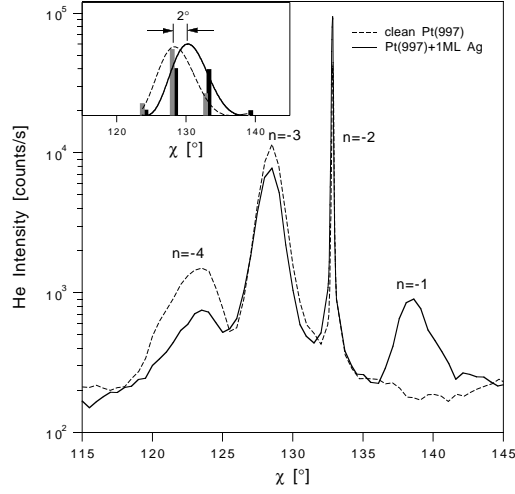


Figure 8.1: He diffraction patterns for: clean Pt(997) (dashed line, grey histogram) and Pt(997)+1ML Ag (solid line, black histogram). $\lambda = 0.910 \text{ \AA}$, $\phi_i = 66.4^\circ$. $n = -2$ is in ideal condition. Inset: integrated intensity of the diffraction peaks (histograms) and fitted form factors (lines) showing the countershift of 2° .

if the incidence is more grazing. As the ideal peak is always observed on the right side of the form factor maximum, the effect of the form factor countershift is an intensity gain, which can be important for very grazing geometry as for $n = -1$ ideal.

The third effect responsible for intensity variations during an adsorption experiment has already been treated in section 2.3.2. This is the defect density variation during the adsorption. The defects act as diffuse scatterers and decrease the intensity in all diffraction peaks.

These three effects are the principal ones. We do not take into account other possibilities here like a different selective adsorption for the covered surface, as there has been no evidence for such a phenomenon for Ag on Pt(997) until now. Selective adsorption gives rise to only sharp peaks and had no influence on the positions where we measured.

8.3 Experimental

The Pt(997) and Pt(779) surfaces are prepared according to the usual procedure (see section 3.3), by repeated cycles of Ar ion sputtering at 750 K and annealing at 900 K. The obtained surfaces are clean within the Auger spectrometer sensitivity. Ag is deposited from a UHV-evaporator with a typical flux of 3×10^{-3} ML/s. This flux is chosen to optimize measuring time as well as counting statistics.

The coverage calibration is performed via monitoring deposition in the $n = -3$ diffraction peak. This peak is in ideal condition far from grazing scattering geometry and its intensity is therefore most sensitive to the order on the terrace. During deposition, the intensity of this peak exhibits oscillations attributed to a layer-by-layer growth (see section 2.3.2). The position of the first maximum at a temperature of 300 K is defined as the monolayer coverage.

8.4 Results

8.4.1 Ag growth on Pt(997)

In this section, we will discuss the Ag growth on Pt(997) in the multilayer and sub-monolayer range, in the temperature range below the alloying temperature, estimated to ~ 500 K on Pt(997). Alloying will be discussed in section 8.4.2. The results obtained for Pt(997) will be compared to the ones obtained for Pt(779).

A) From step bunching to 2D-pillar growth

Figure 8.2 shows a series of deposition measurements monitored with the $n = -1, -2$ and -3 diffraction peaks at various temperatures between 200 and 700 K.

In the temperature range discussed here ($T < 500$ K), we distinguish two ranges: the intermediate temperature range ($300 \leq T < 500$ K) and the low temperature range ($T < 300$ K), as the growth exhibits different behaviors in these two ranges.

Intermediate temperature: $300 \text{ K} \leq T \leq 450 \text{ K}$. The deposition curves do not present a significant dependence on the temperature. The growth is probably dominated by thermodynamics and not kinetically hindered. We can thus discuss all important effects on the measurements at 300 K.

The intensity of the diffraction peaks during deposition exhibits oscillations. The coverages corresponding to the multilayer oscillation maxima are independent of the diffraction order, within the flux reproducibility of $\pm 5\%$. The case $n = -2$ differs much from $n = -1$ and -3 . It is characterized by a strong asymmetry and less peaked maxima, which make the determination of the monolayer completion less precise. The reason of

Figure 8.2: Intensity variation of the $n = -1, -2$ and -3 ideal diffraction peaks during Ag deposition as a function of temperature. $\lambda = 0.90\text{\AA}$. Ag flux = 3×10^{-3} ML/s.

this particular shape is not yet explained but its advantages will be exploited in section 8.4.2.

In figure 8.3, the He intensity variation during Ag deposition at 300 K in the $n = -1$ to -3 orders is presented. The observed oscillations demonstrate an initial 2D-growth mode up to the third layer. The origin of the oscillations can be explained by a common effect of the interference between the substrate and adsorbate layers on a terrace, the countershift of the form factor due to Ag deposition and the defect density variations. In the following, we will analyze the intensity changes in more detail.

During the first monolayer formation, the signal oscillation is mainly due to the interference. The defect density does not play a significant role, at least at the beginning of the growth, as grazing incidence measurements in $n = 0$ (see chapter 5) have shown that the first two rows grow ordered. There is thus no significant defect density increase during the initial stage of deposition. The effect of the form factor countershift induced by Ag (see section 8.2) results in an increase of the intensity in the diffraction peaks. Its effect becomes more important if the incidence angle is more grazing. This explains the large intensity gain (7 times I_0) for the first monolayer completion in $n = -1$. On the con-

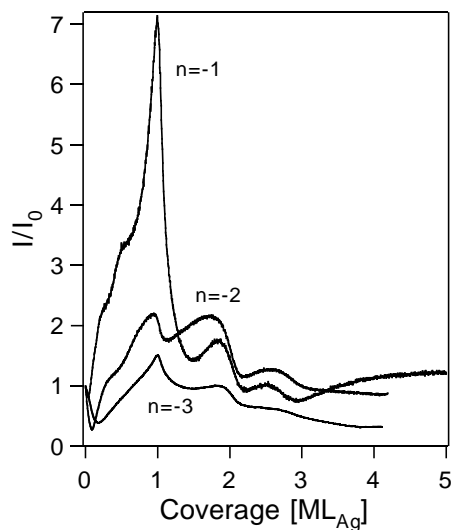


Figure 8.3: Intensity variation of the $n = -1, -2$ and -3 ideal diffraction peaks during Ag deposition at 300 K. $\lambda = 0.90\text{\AA}$. Ag flux = 3×10^{-3} ML/s.

trary, $n = -3$ is not much influenced by the form factor: its intensity gain for a complete monolayer corresponds about to the total reflectivity enhancement of the surface. The He signal oscillations during the formation of the second and further monolayers seems to be principally due to the interference and the defect density variations.

The Ag growth in this temperature range is not regular as the coverage between the successive oscillation maxima decreases with increasing coverage. The first layer is pseudomorphic to the substrate, as it is suggested by a statistical analysis of the deposition curves which infers an average number of about 8 rows in the first Ag monolayer compatible with the number of Pt rows, while the other layers tend to recover the larger Ag bulk lattice constant.

After the third monolayer completion, no more oscillations are visible. The intensity of the diffraction peaks reaches a constant level. Figure 8.4 shows a diffraction pattern measured after deposition of 20 Ag monolayers at 450 K. It exhibits a pronounced additional peak in the specular direction with respect to the (111) terraces on the left side of the $n = -3$ peak. This peak is due to the specular reflection of the He beam by (111) terraces larger than the original terraces of Pt(997). It indicates that an important mass trans-

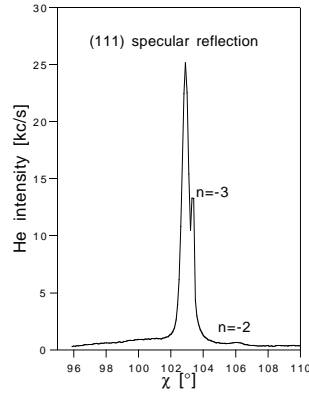


Figure 8.4: Diffraction pattern of Pt(997) + 20 ML Ag deposited at 450 K. $\phi_i = 51.5^\circ$, $\lambda = 0.92 \text{ \AA}$. Note that the $n = -3$ diffraction peak is not quite in ideal condition.

port has occurred during the growth leading to a step bunching of the Ag steps and the formation of large Ag facets. We tend to exclude a Pt substrate step bunching reconstruction. The deposition temperature seems indeed too low to induce such a reconstruction. Moreover, step bunching does not take place for a single Ag monolayer (see figure 8.1), which should be, however, sufficient to initiate the reconstruction. After 3 monolayers, the step bunching has probably already occurred and further Ag deposition takes place following a step-flow process, which could explain the absence of additional oscillations. The remaining presence of the $n = -3$ peak as well as the $n = -2$ (at $\chi = 106^\circ$) suggests that the surface still exhibits regions with the original (997) structure. These are probably regions where the Pt terrace is only covered by one or two Ag monolayers.

Low temperature: $T < 300\text{K}$. At lower temperature, the layer-by-layer growth takes place for a larger number of layers. At least five oscillations are observable in figure 8.2 at 200 K, suggesting that the step bunching does not take place at lower temperature. To control this assertion, the diffraction patterns of about 5 Ag monolayers grown on Pt(779) at intermediate and low temperature have been measured. As will be discussed below, the step structure does not seem to have a significant effect on the growth of Ag on these vicinal surfaces. Therefore, the results obtained for this surface are supposed to be valid for Pt(997) as well. Figure 8.5 shows the diffraction patterns obtained after deposition of 5 ML Ag at low (200 K) and intermediate (400 K) temperatures on Pt(779). At intermediate temperature, a shoulder appears on the left side of the $n = -3$ diffraction peak.

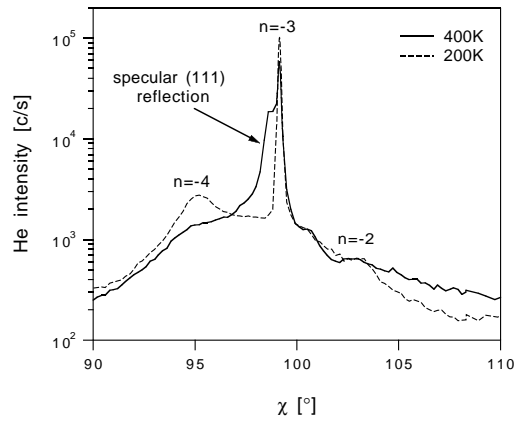


Figure 8.5: Diffraction patterns for Pt(779) + 5 ML Ag deposited: at 400 K (solid line) and at 200 K (dashed line). $\phi_i = 49.6^\circ$, $\lambda = 0.98 \text{ \AA}$.

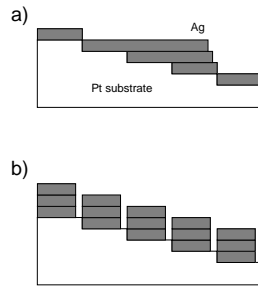


Figure 8.6: Schematic representation of the proposed Ag growth modes on Pt(997) and Pt(779) at: a) intermediate temperature: step bunching and b) low temperature: 2D-pillar growth.

This peak corresponds to the specular reflection of (111) facets. At lower temperature, this peak does not occur, demonstrating that step bunching is hindered.

We suggest that the origin of this phenomenon is an enhanced step-edge barrier [117–119] near the first monolayer completion. To grow the eighth and last row of the

monolayer, Ag atoms have to overcome this barrier, which is possible at sufficiently high temperature. At low temperature, growth can proceed on the second layer before the first one is completed and further deposition does not result in a filling of the missing row. This interpretation is corroborated by the deposition measurements. At 200 K, the first monolayer maximum corresponds to about 90 % of the coverage necessary to complete the first monolayer at 300 K. The consequence of this missing row is probably to hinder mass transport between adjacent terraces and the growth proceeds on each terrace separately. Because of the small terrace size, the growth is then 2-dimensional [26] and oscillations are visible in the He intensity during deposition. Figure 8.6 shows a scheme of the probable growth modes of Ag on Pt(997) at intermediate (step bunching) and lower temperature (2D-pillar growth).

B) Ag growth: comparison between Pt(997) and Pt(779)

Pt(997) and Pt(779) are very similar surfaces as both have (111) terraces of almost identical mean size. The interest to compare them comes from the different type of step structure (see section 3.3). The structure of the step might for example influence the growth via different mobilities along the step edge [120, 121] and different step edge barriers [122].

This section discusses the restricted set of measurements performed up to now on Pt(779). It concentrates on the first monolayer growth.

Ag deposition measurements have been performed in the same diffraction peaks as for Pt(997), i.e. $n = 0$ and $n = -1, -2, -3$ in ideal condition. The obtained curves at 300 K are shown in figure 8.7. They are similar to the ones obtained on Pt(997) (figure 8.3) indicating that the growth takes place in a similar way. However, a slight difference with respect to Pt(997) occurs near monolayer completion. A shift is observed between the first He intensity maximum in $n = -3$ and $n = -1$, which was not observed for Pt(997). A look at the deposition curves in $n = 0$ shows that a maximum occurs for the same coverage as for $n = -1$. The coverage at which the maxima occur correspond to 7 rows ($\pm 5\%$) for $n = 0$ and $n = -1$, and to about 8 rows for $n = -3$, as inferred from a statistics performed over several deposition curves. Related to the average width of a Pt(779) terrace of 7.7 rows, this suggests that the 7th row is completed with a high order, which gives rise to a peak in the step sensitive diffraction orders $n = 0$ and $n = -1$, while in the terrace sensitive $n = -3$ order, however, the intensity maximum is reached when the 8th and last row is deposited. The reduced space for the 8th row growth is probably responsible for its worse order, which hinders its observation in $n = 0$ and $n = -1$. This interpretation is reasonable if one considers the slope change at the right side of the $n = -1$ peak, which corresponds to the occurrence of the maximum in $n = -3$. The additional terrace sensitivity of $n = -1$ can explain this feature.

The absence of a shift of the monolayer maxima between the diffraction orders on

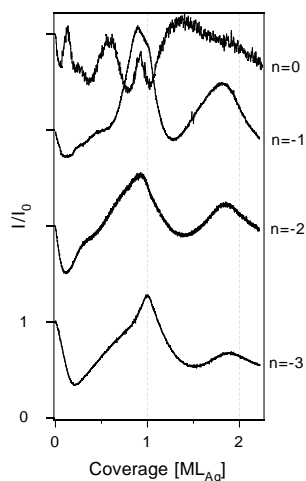


Figure 8.7: Deposition curves of Ag on Pt(779) at 300 K. a) $n = 0$: $\theta_i = \theta_f = 80^\circ$. $n = -1$ ideal: $\phi_i = \phi_f = 77.5^\circ$. $n = -2$ ideal: $\phi_i = \phi_f = 64.4^\circ$. $n = -3$ ideal: $\phi_i = \phi_f = 49.55^\circ$. $\lambda = 0.98 \text{ \AA}$. Ag flux = $2 \times 10^{-3} \text{ ML/s}$.

Pt(997) can be explained by its larger terrace mean width of 8.33 rows. It can more easily accommodate 8 Ag rows, as the 8th has enough space to grow, but the growth of the 9th is probably excluded. The most ordered row at the end of the monolayer deposition is thus the 8th one, which also corresponds to the coverage of the monolayer completion. The maxima occur thus for the same coverage in the different diffraction orders.

The effect of the step structure on the growth is not evident. In $n = 0$ diffraction order, completion of the first two rows is observed while further row completion is smeared out due to desynchronization (see below). As diffusion is expected to be faster along the (100)-facet steps of Pt(779) [120] favoring thus the row-by-row growth, the observation of the same signal for the row completion suggests that row-by-row growth may proceed for a larger number than two rows on Pt(997) as well as on Pt(779). Similar growth on both substrates indicates that the mobility along the steps is always high enough to provide an equilibrium configuration, at least in the flux regime which we have employed.

In conclusion, as far as growth is concerned, an effect due to the different terrace lengths is seen, but no evidence for a different property due to the different step structure is found. We will see in section 8.4.2 that it plays however a role in the alloying and demixing processes.

C) Row-by-row growth

In figure 8.2, deposition measurements of Ag on Pt(997) in the $n \neq 0$ diffraction peaks exhibit intensity variations already in the submonolayer range. However, except at low temperature, these variations are not resolved. This is not the case in the $n = 0$ diffraction peak which exhibits well resolved maxima in the submonolayer range and is therefore the best candidate to study this stage of deposition. The essential observations have been already discussed in chapters 4 and 5. We focus here on additional points.

Desynchronization of the row completion. Like Xe and Kr, Ag exhibits a row-by-row growth. This point has already been shown in chapter 4. It is deduced from the intensity oscillations of the $n = 0$ diffraction peak during deposition. The row-by-row growth is observed for the first two rows. It is however premature to conclude from this absence that the third row does not form in an ordered way. The terrace width distribution is responsible for the impossibility to observe the further row completion. This is demonstrated in figure 8.8, the result of a simulation (Computer code: see Appendix B) of the intensity in the $n = 0$ diffraction peak during an ideal row-by-row growth. The simulation assumes that the terrace width distribution obeys a gaussian law centered at 20.2 Å with a mean square deviation of 2.4 Å, as obtained from a statistical study of STM topographs [44]. The intensity in the $n = 0$ peak is assumed to come exclusively from the step-edge and all the step-edge contributions are supposed to add coherently. During the deposition, the incoming atoms are supposed to diffuse immediately to the step-edge and are incorporated in a single incomplete row at the same time. The flux to the step depends on the width of the terrace, as no interlayer exchange is assumed. Thus not all the rows are completed at the same coverage. The defect density in the incomplete row is modeled by a “sine-squared” function, being minimal for complete rows and maximal for half complete rows. The intensity coming from a step-edge is set equal to 1 minus the defect density. The simulation in figure 8.8 is obtained by adding the intensities coming from terraces of different size weighted by their statistical occurrence on the surface. It shows (thick solid line) that after only 2 rows, the completion of the rows on the different terraces is already desynchronized and no further maxima are observable. This corresponds fairly well to a Ag deposition measurement at 300 K at grazing incidence (thin solid line). The model illustrates that row-by-row growth may continue to higher coverages than indicated by the observed oscillations. STM observations made by P. Gambardella *et al.* on this system [123] showed the smooth step edge of the Ag islands at half a monolayer coverage, which tends to confirm this fact for Ag on Pt(997). The simulation forecast, near monolayer completion, a resynchronization of the row completion (thick dashed line) which is not observed in the measurements. This may indicate that the end of the monolayer formation does not take place according to a row-by-row growth, at least for the two last rows.

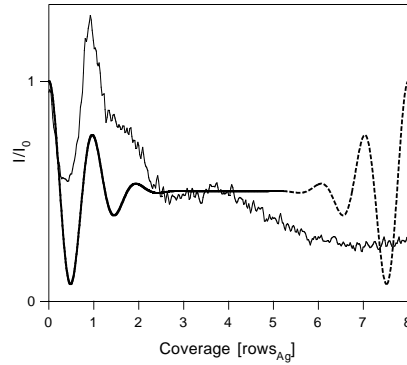


Figure 8.8: Simulation of the He intensity in the $n = 0$ peak (thick line) and comparison with a measured Ag deposition curve on Pt(997) (thin line). $\theta_i = \theta_f = 85.0^\circ$, $\lambda = 0.89 \text{ \AA}$, Ag flux = $3 \times 10^{-3} \text{ ML/s}$.

Temperature dependence. The behavior of the submonolayer deposition in the $n = 0$ peak has been investigated as a function of temperature. The scattering geometry is very grazing ($\theta_i = \theta_f = 85.0^\circ$) to increase the step sensitivity.

Figure 8.9 presents the Ag deposition curves obtained in $n = 0$ for temperatures between 150 and 700 K. The focus is on the first two rows. In a large temperature range ($200 \leq T \leq 450 \text{ K}$), no important change can be observed. In this temperature range, the growth is dominated by thermodynamics. The Ag atom mobility is sufficiently large to allow Ag atoms to diffuse to the step without nucleation of islands on the terrace. The mobility along the step is sufficiently large as well to allow row growth.

At lower temperature ($T = 150 \text{ K}$), the second row shoulder is no more present. The coverage of the first row peak still corresponds to a single row but its shape is less peaked than at higher temperature, probably due to a reduced adatom mobility which gives rise to a disordered step decoration already during the end of the first row growth.

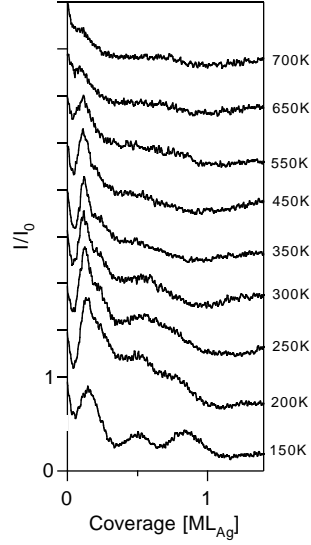


Figure 8.9: Ag deposition on $n = 0$ as a function of temperature. Flux= 3×10^{-3} ML/s, $\theta_i = \theta_f = 85.0^\circ$, $\lambda = 0.89 \text{ \AA}$.

Half-monolayer reflectivity maximum. During Ag deposition on Pt(997) and Pt(779), a reflectivity maximum is observed in $n = 0$ at about half a monolayer (see figure 8.10) in most of the employed geometries. A similar feature is observed for other adsorbates like Co and Cu. It is thus a general phenomenon. The temperature range in which this reflectivity maximum occurs has not been well established for Ag, as most of the measurements have been performed at 300 K. More systematic measurements as a function of temperature have been performed on Co and Cu, which show that there is a defined temperature range in which the reflectivity maximum occurs. It is however not the purpose of this section to discuss the thermodynamics of this phenomenon, but rather to try to give a plausible explanation.

To explain the origin of this reflectivity maximum, we will first proceed by elimination.

1. The coverage at which the reflectivity maximum takes place is independent of the scattering geometry. This indicates that the reflectivity maximum is not an artefact due to interference but originates from a certain ordered structure on the surface.
2. The reflectivity maximum occurs for both Pt(997) and Pt(779). Therefore, the

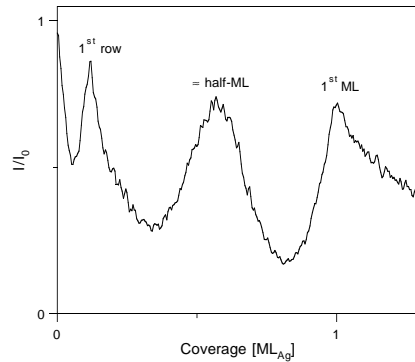


Figure 8.10: Ag deposition curve in $n = 0$ at 300 K showing the occurrence of a reflectivity maximum at about half a monolayer on Pt(997). $\theta_i = \theta_f = 82.7^\circ$, $\lambda = 1.05\text{\AA}$, Flux= 3×10^{-3} ML/s.

reflectivity maximum cannot be due to the formation of triangular islands growing from the step, the origin of which would be different diffusion barriers along the (111) and (100)-facet steps. A difference in mobility could explain the occurrence of this pattern on Pt(997) or Pt(779) but not on both surfaces.

3. The reflectivity maximum does not come from a highly disordered structure, which would increase the He intensity in all angular directions. This is excluded by a deposition measurement performed at a scattering geometry off the $n = 0$ diffraction peak monitoring the background intensity, which does not exhibit any reflectivity maximum at half a monolayer.

These preliminary considerations indicate that the reflectivity maximum is linked to a certain structure on the surface. As the intensity is maximal for this particular structure, a possible explanation is an increased order in the step for this structure with respect to the situation immediately before and after its occurrence. The reason for this higher step ordering could be an interaction with the Pt step in front of the growing Ag step or a strain field on the terrace coming from a reconstruction of the Pt substrate. However, a more reasonable explanation is to consider the evolution of the terrace width distribution during the growth of the first monolayer. Several assumptions, which will be discussed later, have to be made first:

- perfect row-by-row growth takes place .
- Ag atoms deposited on the Pt part of a terrace cannot diffuse down the descending Pt or Ag step and stick to the ascending step.
- Ag atoms deposited on the Ag covered part of a terrace cannot cross the Pt-Ag step interface and are incorporated in the lower Ag step. The allowed diffusion processes are symbolized in the inset of figure 8.11.

The result of such a step-flow growth is a narrowing of the terrace width distribution at half a monolayer because it links two adjacent terraces acting as a smoothing function on the terrace width distribution.

A calculation performed over 1000 terraces distributed randomly over the surface and obeying a gaussian law centered at 8.33 rows with a mean square deviation of 1.5 rows is shown in figure 8.11. This calculation takes into account the assumptions given above and gives the mean square deviation of the terrace width distribution during the growth of a Ag monolayer (for code see Appendix B). The narrowing of the terrace width distribution at half a monolayer is well reproduced.

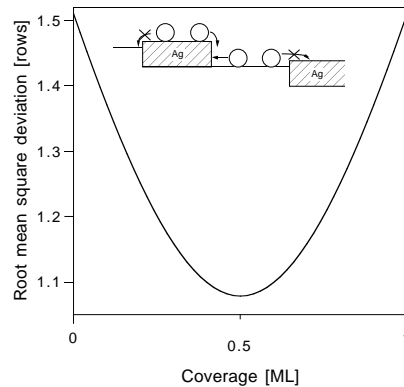


Figure 8.11: Root mean square deviation of the terrace width distribution during the perfect row-by-row growth of a Ag monolayer according to the model described in text. Inset: allowed and forbidden processes for Ag atom diffusion at the step.

As the terrace width distribution induces a broadening of a diffraction peak which is not in ideal condition, a narrowing of this distribution will reduce this broadening and the maximum intensity of the peak will increase, if we moreover suppose that the integrated

intensity of the peak remains constant. This argumentation applies particularly for $n = 0$ which is by definition not in ideal condition.

We now discuss the assumptions made in the growth model. A perfect row-by-row growth during the monolayer deposition has not yet been excluded by the deposition measurements in the $n = 0$ order. The large barrier for Ag atoms to cross the Pt-Ag step interface has already been observed for Ag on Pt(111) [115]. The step edge barrier for Ag atoms to descend the Pt step has been equally observed and estimated to 30 meV [115]. This last assumption is however not absolutely necessary as after the deposition of the first Ag row, the next Ag atoms have to cross the Pt-Ag interface, which is excluded.

If the origin of the reflectivity maximum is correctly identified, its occurrence gives information on the growth and on the mass transport between the terraces, confirming the previous observations of Röder *et al.* [115]. Its exact position, which is in fact 0.57 ML for Ag but closer to 0.5 ML for Co, may give additional information on the diffusion processes on the surface.

8.4.2 Alloying and demixing processes

A) Alloying

At high temperature, Ag can no more be considered to diffuse and grow phase separated on the Pt substrate. On Pt(111), a submonolayer amount of Ag is known to alloy into the first Pt layer for substrate temperatures above 620 K according to Röder *et al.* [116]. Ag on Pt(997) exhibits the same behavior as can be seen from the experiment shown in figure 8.12. In the experiment, the Pt(997) surface is covered with 30% of a monolayer Ag at 300 K and then slowly annealed to 900 K and cooled back to 300 K. The He intensity in the $n = -3$ diffraction peak is monitored during these ramps (full symbols).

The heating rate is slow (0.2 K/s) and the system may be considered in quasi-equilibrium during the measurement. At the beginning of the annealing, the He intensity decreases due to the Debye-Waller factor until around 500 K where a slope change occurs. It corresponds to the onset of the alloying. The intensity loss is due to the formation of Ag clusters in the Pt surface, which act as defects diffusely scattering a part of the He intensity. The intensity loss remains after cooling, because the alloy is stable. The measurement is similar to the measurement performed by Becker *et al.* on Pt(111) [114] and gives a similar alloying temperature range from 500 to 600 K.

Deposition curves above the alloying temperature taken in the $n = 0$ diffraction peak provide information on the initial stage of alloying. In figure 8.9, one can see that above 550 K, the second row shoulder has disappeared and the first row peak progressively vanishes as well. The intensity in the first row peak decreases probably because of the disordering of the first Ag row with thermal agitation. If the Ag atoms would diffuse into the Pt terrace, no first row peak would occur. In section 5.3.3, we demonstrated

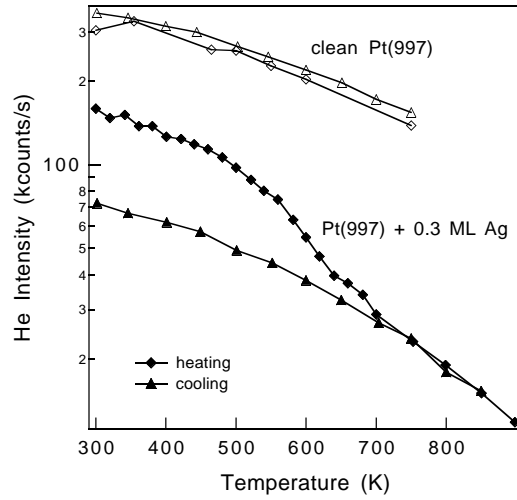


Figure 8.12: He intensity in the $n = -3$ diffraction peak vs temperature, for Pt(997) covered with 0.3 ML Ag (full symbols) and clean Pt(997) (open symbols). $\phi_i = 52.8^\circ$. $\lambda = 0.92\text{\AA}$.

that a proceeding Pt step exhibits no oscillations. The presence of the first row peak at a coverage of ~ 0.12 ML at temperatures much higher than the alloying temperature indicates thus that no alloying occurs for the first row and that alloying does not occur on the terrace but takes place via the step, as has been observed on Pt(111) by Röder *et al.* [116]. The fact that the first row peak does not undergo a significant shift with the temperature increase indicates that a Ag row always floats at the Pt step and that the rest of the Ag deposited above the alloying temperature may alloy via the step in the Pt terrace. The alloying thus does not take place for a coverage smaller than one row.

B) Demixing

A demixing process upon monolayer completion has been observed by STM by Röder *et al.* [116] for Ag on Pt(111), resulting from the tendency of Ag to avoid embedding under the Ag layer. On Pt(997) and Pt(779), an evidence of this process during deposition above the alloying temperature is obtained from the deposition curves in $n = -2$. Figure 8.13 shows the Ag deposition curve at 600 K in the $n = -2$ ideal condition. One can see the occurrence of a steep intensity increase (spike) beginning at 0.93 ML and ending at 1.0 ML. A smaller but similar feature is still visible at 500 K in figure 8.2. This feature is

attributed to the demixing process which takes place at the monolayer completion, as it is absent for temperatures significantly lower than the measured alloying temperature.

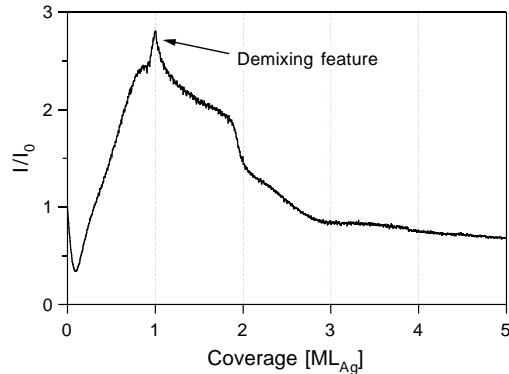


Figure 8.13: He intensity during Ag deposition in $n = -2$ ideal at 600 K. $\phi_i = 66.7^\circ$. $\lambda = 0.90\text{\AA}$.

The demixing is accompanied by a minimum of the defect density which explains the intensity gain. To explain the discontinuity of the intensity at about 0.93 ML, it is necessary to suppose that the Ag-Pt alloy, at this temperature, is confined to a thin stripe at the Ag-Pt step interface. The width of this stripe grows with time as the alloying is an activated process. The presence of a confined alloy is suggested by the large He intensity in the peak very similar to the intensity at 300 K deposition. If an alloy was covering the entire terrace, its roughness should decrease substantially the He intensity which is not observed. The employed flux is such that the Ag layer grows more quickly than the alloy. When the Ag step encounters the alloy stripe, it induces the demixing which gives rise to the intensity increase. Deposition curves measured at 600 K for different fluxes (4×10^{-3} to 1×10^{-3}), show that the size of the demixing feature in the He signal depends only on the coverage and not on the flux, suggesting that the demixing process is much faster than the deposition.

At 700 K, the deposition curve (see figure 8.2) does not exhibit a resolved demixing feature. The reason for this is probably that the alloying proceeds faster and the growing Ag step encounters the alloy sooner than at 600 K. The He intensity increase accompanying the demixing sets thus in after a coverage smaller than 0.8 ML. The consequence of this increase is that the demixing feature is no more resolved.

The occurrence of the demixing feature in $n = -2$ gives an indirect evidence of the

alloying which allows to determine more precisely the alloying temperature than the measurements performed in $n = -3$. A small demixing feature at 500 K on Pt(997) indicates that alloying already starts at this temperature. We therefore consider $T=500 \pm 20$ K as being the alloying temperature for Pt(997). This value is significantly smaller than the value of 620 K obtained from STM studies on Pt(111) [116]. The reason is not clear but tends to be related more to the technique than to the different investigated substrates. The measurement performed in $n = -3$ during alloying of 0.3 ML Ag on Pt(997) gives indeed a result similar to the measurement performed by Becker *et al.* on Pt(111) [114], indicating that both substrates have the same alloying temperature with Ag. An explanation for the discrepancy might be that, the alloy observed by TEAS at low temperature is metastable and reversible upon cooling. Therefore, it could not be observed by STM, which takes pictures of static systems after cooling at lower temperature, while TEAS probes the dynamics of the process.

The reason why the demixing process is visible in $n = -2$ and not in the other diffraction orders is not clear. One would expect to see demixing for all orders except $n = 0$. One may argue based on the particular shape of the deposition curves in $n = -2$. The shape is much less peaked than for $n = -1$ and $n = -3$. It is thus easier to resolve the steep increase accompanying the last stage of the demixing in $n = -2$.

C) Comparison: Pt(997) and Pt(779)

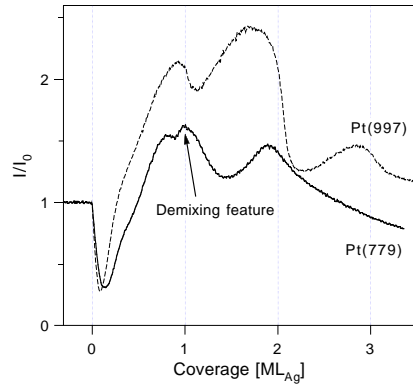


Figure 8.14: Deposition curves of Ag in $n = -2$ ideal at 400 K: a) on Pt(779) (solid line), $\phi_i = \phi_f = 64.4^\circ$. $\lambda = 0.98$ Å. Ag flux = 4×10^{-3} ML/s. b) on Pt(997) (dashed line), $\phi_i = \phi_f = 66.7^\circ$. $\lambda = 0.90$ Å. Ag flux = 3×10^{-3} ML/s.

Whereas the Ag growth does not seem to be affected by the step structure of the substrate, the alloying process depends on it. Alloying takes place on Pt(779) at lower temperature than on Pt(997). Figure 8.14 shows Ag deposition curves performed in $n = -2$ at 400 K on Pt(779) and Pt(997). One can see the typical demixing shoulder near monolayer completion on Pt(779), while it does not occur for Pt(997). This demonstrates that alloying occurs on Pt(779) at least 100 K below the alloying temperature on Pt(997). This is probably due to the less densely packed structure of the (100) step of Pt(779) compared to the (111) step of Pt(997), which makes the Ag incorporation more favorable.

8.5 Summary

The Ag growth on Pt(997) has been studied in detail. Below the alloying temperature, the growth proceeds in a row-by-row fashion until at least the second row. We showed that the desynchronization of the row completion on terraces with different sizes hinders the observation of the probably continued formation of ordered rows. The multilayer deposition proceeds layer-by-layer for any temperature until the third layer. Further deposition at intermediate temperature leads to a faceted surface, while at low deposition temperature layer-by-layer growth continues. This behavior is probably associated with an increased step-edge barrier for Ag atoms to descend the 7th row. The increase may be due to the unfavorable site, near the Pt step edge, that a Ag atom has to occupy to complete the monolayer.

The extreme sensitivity of TEAS for the surface changes gives rise to a large number of features in the He-signal. A He intensity reflectivity maximum during Ag deposition in $n = 0$ occurs near half a monolayer. This reflectivity maximum is probably due to the narrowing of the terrace width distribution during the Ag layer growth. If this interpretation is correct, the occurrence of this reflectivity maximum indicates that the row-by-row growth may proceed until at least the fourth row and maybe further.

Growth was expected to be different on Pt(779) due to the different step structure, which should favor row-by-row growth. The mobility along the (100)-facet step of Pt(779) is indeed larger than along the (111)-facet step of Pt(997) [120]. However, no difference is observed, which can be related to the step structure. The average terrace width on Pt(779) (7.7 rows) and Pt(997) (8.33 rows), which produces a compressive and tensile stress respectively during deposition of the 8th row, could explain the difference of the Ag deposition curves in the different diffraction peaks near monolayer completion.

The structure of the step becomes important when deposition takes place at higher temperature. Alloying starts at a lower temperature on Pt(779) than on Pt(997). The alloying energy barrier is lower for Pt(779), which is comprehensible from the fact that the step is less densely packed than on Pt(997).

Alloying has been studied mostly on Pt(997). A He intensity measurement in $n = -3$

for Pt(997) + 0.3 ML Ag as a function of temperature, similar to the measurement performed by Becker *et al.* on Pt(111) [114], gives a similar temperature range of 500-600 K for the Ag alloying on Pt(997). The alloying is found to be a slow process, which is not in equilibrium during deposition at least below 700 K. The alloy is then confined in a stripe near the Ag-Pt step interface, which grows farther inside the terrace with time. Deposition measurements in $n = 0$ have shown that alloying occurs at the step and not directly on the terrace. They also suggest that a Ag row always floats at the step and no alloying occurs below first row coverage. Demixing features in the deposition curves in $n = -2$ give access to the demixing process which occurs during monolayer completion and give precise information on the alloying transition temperature. On Pt(997), alloying is found to occur around 500 K.

Chapter 9

Silver-Cobalt metal sandwiches on Pt(997)

9.1 Introduction

The magnetism of low-dimensional structures is currently a topic of substantial interest. This interest is motivated by applications in the magneto-optical storage devices. Layered magnetic structures are able to provide large anisotropic perpendicular magnetization usable to store information [124–127]. The morphology of the grown layer appears to be an important factor for the remanent magnetization.

In this chapter, we study layered structures of magnetic and non magnetic elements. We investigate the stability of a multilayer structure formed by one monolayer of Co and one monolayer of Ag on Pt(997) as a function of temperature. The objective is to learn more about the interactions between the three elements: Co, Ag, and Pt. To which extent, can Ag hinder the tendency of Co to diffuse into bulk Pt [128,129] ? Is Ag able to stabilize a Co monolayer? We will try to answer these questions in this chapter. The possible use of the Pt(997) surface as a template for creating a one-dimensional superlattice of alternated magnetic and non-magnetic rows requires this preliminary knowledge. To help in the interpretation of the results, the simpler systems formed by a monolayer (Co or Ag) on Pt(997) will be first studied and the multilayer results will then be discussed on this basis.

This study has been performed by means of TEAS, which presents the necessary sensitivity. In fact, the sensitivity to surface modifications is sometimes disturbingly high, because TEAS is sensitive to even minute changes (morphology, chemical composition) at the surface as shown in the preceding chapter. On the other hand, the deposition curves and the diffraction spectra cannot provide chemical information on the system, which is important in this study and requires the use of Auger spectroscopy (AES).

9.2 Experimental

The Pt(997) surface is prepared according to the usual procedure (see section 3.3), by repeated cycles of Ar ion sputtering at 750 K and annealing at 900 K. The obtained surface is clean within the Auger spectrometer sensitivity. The clean Pt(997) crystal presented a small amount of (111) facets which could not be removed completely for the measurements performed in this chapter. They appear as a peak on the right side of the $n = -3$ diffraction peak in the diffraction patterns. Ag and Co are deposited from a UHV-evaporator with a typical flux of 3×10^{-3} ML/s.

Ag and Co monolayer deposition is controlled by monitoring the He scattering intensity in the $n = -3$ diffraction peak during deposition. To reduce Co diffusion into the Pt substrate, Co is deposited at 250 K, while Ag, when deposited first, is deposited at 400 K to provide an ordered layer.

Information on the ordering of the system with temperature is obtained by monitoring the He intensity in the $n = -3$ diffraction peak during temperature ramps. The chosen diffraction peak is set in non-ideal geometry in order to obtain a peak of about 1° width. The purpose is to minimize the effect of the unavoidable thermal drift of the sample holder on the He intensity. A typical drift of 0.05° of the sample polar angle would lead to an intensity loss of 50% for a peak in ideal condition, whereas it is negligible for a 1° width peak. The particularly large temperature range used in this study (250 to 800 K) motivates this precaution, which was not necessary in the experiments performed in the preceding chapters.

Additional information on the layer morphology is obtained by recording the diffraction pattern around the $n = -3$ peak at certain temperatures where changes take place. This allows to determine more precisely in which proportion the intensity changes can be attributed to a defect density variation or an interference modification.

Complementary Auger spectra taken for certain temperatures are used to determine the surface composition during the temperature ramps. The low energy Auger electron peaks of Pt (43 and 64 eV) and Co (53 eV) are of particular interest because of their high surface sensitivity. No change of intensity is observed in the Ag Auger electron peaks, which are more energetic (around 400 eV) and probe deeper atomic layers, because Ag does not leave the first two layers (see chapter 8).

9.3 Results and discussion

9.3.1 Reference systems: 1 ML Co on Pt(997) and 1 ML Ag on Pt(997)

A) 1 ML Ag on Pt(997)

The complete Ag monolayer undergoes no modifications below desorption temperature. It remains above the Pt substrate and there is no alloying or bulk diffusion. This result is deduced from the He diffraction patterns taken at 400 K after deposition and after annealing at 800 K (figure 9.1). No change is visible neither in the absolute nor in the relative intensity of the peaks. Auger spectra taken before and after annealing exhibit no Ag coverage change. This result is in accordance with observations made for Ag on Pt(111) [116].

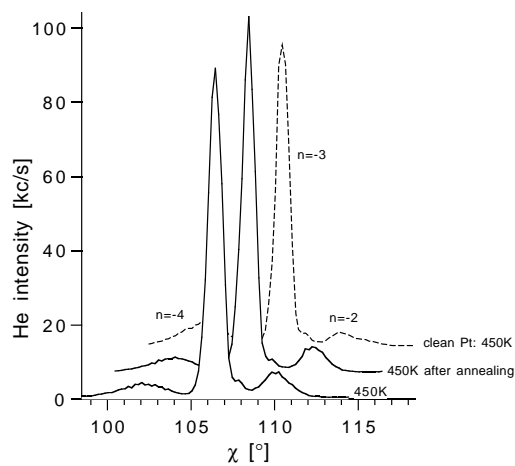


Figure 9.1: He diffraction pattern of Pt(997) covered with 1 ML Ag at 450 K after deposition and after annealing for 5 minutes at 800 K (solid line). Dashed line: reference pattern of clean Pt(997) at 450K. $\phi_i = 54.0^\circ$, $\lambda = 1.02\text{\AA}$.

B) 1 ML Co on Pt(997)

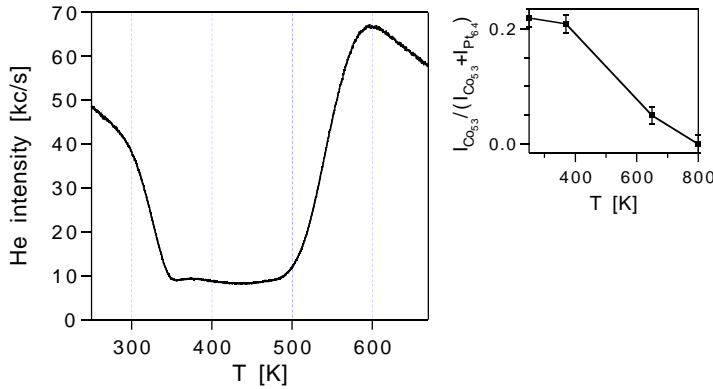


Figure 9.2: He intensity in the $n = -3$ diffraction peak as a function of temperature for Pt(997) covered with 1 ML Co. $\phi_i = 54.0^\circ$, $\chi = 106.4^\circ$, $\lambda = 1.02 \text{ \AA}$. Inset: relative intensity of the Co Auger peak (53 meV) during heating.

Figure 9.2 shows the intensity in the $n = -3$ diffraction peak during heating of a Pt(997) surface covered with a Co monolayer. The heating rate is 8 K/min. The inset in figure 9.2 presents the relative intensity of the Co Auger peak during the heating of the system and figure 9.3 presents a series of diffraction patterns around $n = -3$ taken at certain temperatures.

The Co monolayer is not stable on the Pt(997) surface. Heating of the system induces an important surface disordering around 320 K indicated by the steep decrease in the $n = -3$ peak intensity in figure 9.2 and confirmed by the He diffraction pattern at 375 K (see figure 9.3). An Auger spectrum at 370 K shows, however, no significant Co loss from the surface (see inset in figure 9.2). Diffusion into the bulk is marked by the sudden increase of intensity around 550 K. Above 600 K, the He intensity has almost completely recovered, if we correct for the Debye-Waller factor of the clean Pt(997) surface. This indicates that the first layer is quite flat and only contains a small fraction of Co atoms. Co has diffused under the first layer but is not far from the surface, probably in the second or third layer, as the Co low energy Auger peak is still clearly visible. This is in accordance with previous LEED and AES studies on Pt(111) [128, 129]. The Co bulk diffusion into Pt is a slow process on a time scale of minutes at the employed temperatures. The intensity decay in the $n = -3$ order during heating above 600 K is mainly due to

the Debye-Waller factor as it is reversible with cooling. After annealing at 800 K for 5 minutes, the He diffraction pattern still exhibits small distortions due to the underlying Co (see figure 9.3). The Pt Auger spectrum does not completely recover the intensity of a clean Pt substrate indicating that Co is near the surface.

9.3.2 Multilayer systems

The behavior of single monolayers of Co and Ag on Pt(997) is thus quite complementary: the Ag monolayer tends to stay above the sample surface while the Co monolayer tends

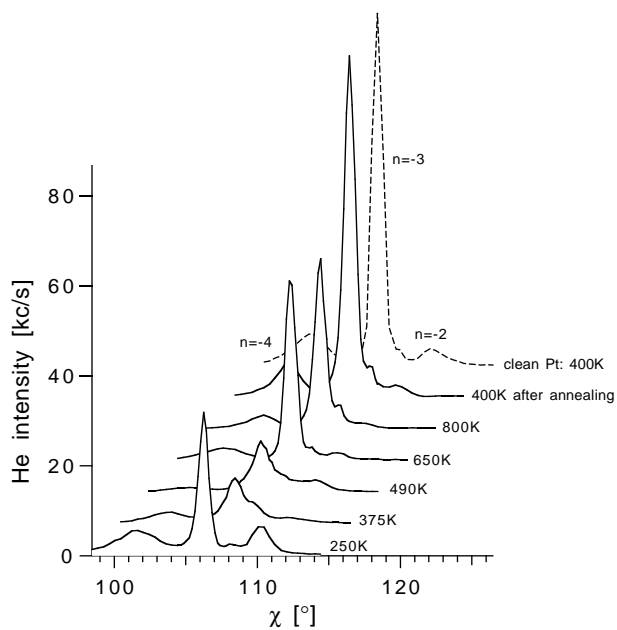


Figure 9.3: Diffraction pattern of Pt(997) + 1 ML Co around the $n = -3$ order for different temperatures (solid line). Dashed line: reference pattern of clean Pt(997) at 400 K. $\phi_i = 54.0^\circ$, $\lambda = 1.02\text{\AA}$.

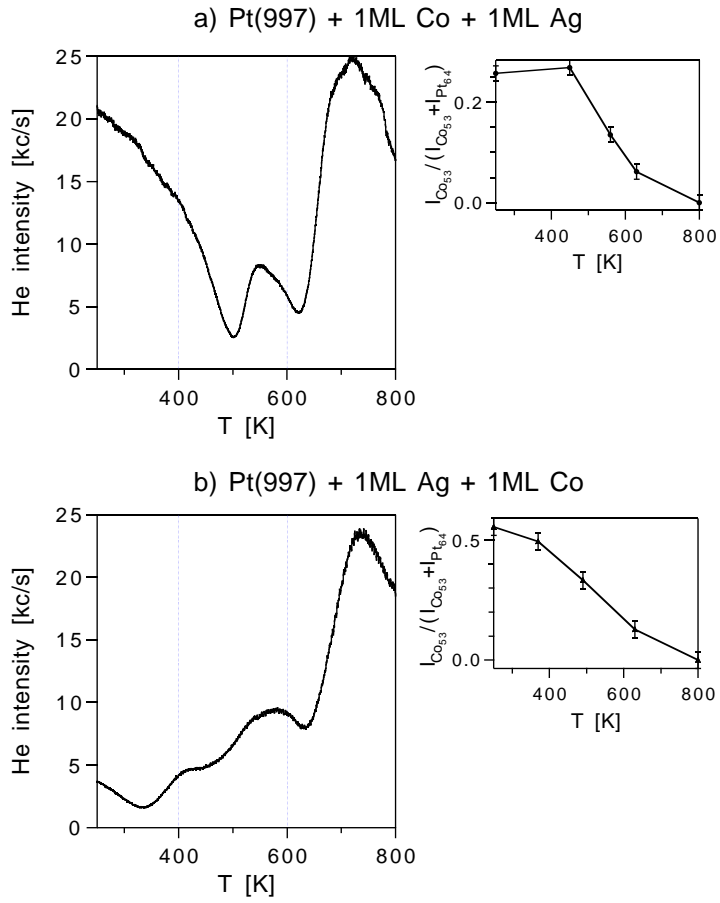


Figure 9.4: He intensity in the $n = -3$ diffraction peak as a function of temperature for Pt(997) covered a) with 1 ML Ag on top of 1 ML Co and b) with 1 ML Co on top of 1 ML Ag. $\phi_i = 54.0^\circ$, $\chi = 106.4^\circ$, $\lambda = 1.02 \text{ \AA}$. Insets: Relative intensity of the Co Auger peak (53 meV) as a function of increasing temperature for the two systems.

to alloy in the Pt substrate. In a layered structure formed with these two elements, we may expect that these tendencies still prevail, but will be modified by the presence of the corresponding other element. The stacking sequence in which the Co and Ag monolayers are deposited on the surface is expected to lead to different behaviors of the system, as different interfaces are formed.

Figure 9.4 shows the variation of the He intensity in the $n = -3$ diffraction peak during heating of the both multilayer systems: (a) Pt(997) + 1 ML Co + 1 ML Ag and (b) Pt(997) + 1 ML Ag + 1 ML Co. The heating rate is 8 K/min. The insets on the right side of figure 9.4 show the relative intensity of the Co Auger peak at 53 meV as a function of temperature. Figures 9.5 and 9.6 show two series of He diffraction patterns of the systems taken around the $n = -3$ order at certain temperatures, providing information on the distribution of the scattered He intensity.

The two systems exhibit different behaviors during heating, which will be discussed in the following sections.

A) 1 ML Ag on top of 1 ML Co on Pt(997)

The He intensity in the $n = -3$ diffraction peak as a function of temperature (see figure 9.4 a) is characterized by a large initial value (at 250 K) which slowly decreases until about 400 K. The He intensity decrease becomes steeper from 400 K until about 500 K and significantly increases after heating above 700 K, reaching a value comparable to a Pt(997) surface covered with a Ag monolayer.

The Ag layer delays the surface disordering which occurs for a single Co monolayer above 300 K. At 400 K, neither the He diffraction pattern nor the Auger spectrum exhibit significant differences compared to the situation at 250 K (see 9.4 a and figure 9.5). The constant Co peak in AES suggests that no Co-Ag alloy forms.

For temperatures above 400 K, the surface becomes more disordered, which is indicated by the He intensity decrease in all diffraction peaks. The disordering is most likely connected with an alloying of Co with the Pt substrate as the Auger spectrum at 560 K shows a decrease of the Co low energy Auger line. The observation indicates that no substantial amounts of Co diffuse into the Ag layer. Around 650 K, Co diffuses into the Pt substrate, which is marked by the steep He intensity increase in the $n = -3$ peak (see figure 9.4 a). This process takes place about 100 K after the same process for a single Co layer on Pt(997).

Annealing to higher temperatures induces a further decay of the Co amount in the topmost layers. The He diffraction pattern (figure 9.5) after 5 minutes annealing at 800 K exhibits the same shape as in the case of a single Ag monolayer on Pt(997) (figure 9.1) indicating that the Ag layer remains above the Pt surface.

The local intensity maximum observed around 550 K in $n = -3$ might be due to a displacement of the form factor and does not indicate a substantial change in disordering.

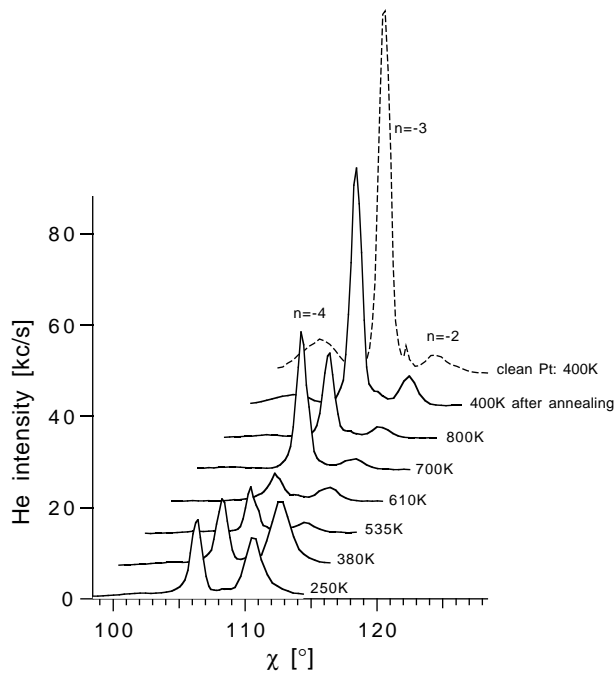


Figure 9.5: Diffraction pattern of Pt(997) + 1 ML Co + 1 ML Ag around the $n = -3$ order for different temperatures (continuous line). Dashed line: reference pattern of clean Pt(997) at 400 K. $\phi_i = 54.0^\circ$, $\lambda = 1.02\text{\AA}$.

One can see in figure 9.5 that, after deposition at 250 K, the $n = -2$ peak receives an intensity comparable to the one in $n = -3$. The form factor maximum is thus shifted towards larger scattering angles. At 535 K, near the local intensity maximum in $n = -3$, the intensity is principally in the $n = -3$ peak and the form factor has thus shifted back towards smaller scattering angles.

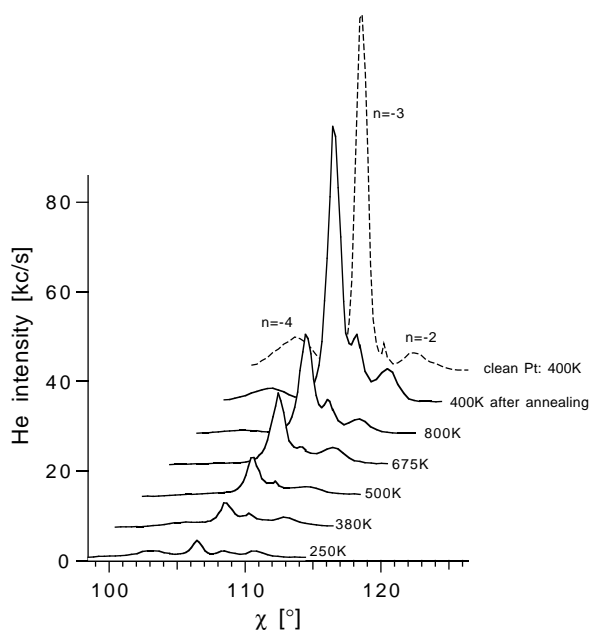


Figure 9.6: He diffraction pattern of Pt(997) + 1 ML Ag + 1 ML Co around the $n = -3$ order for different temperatures (solid line). Dashed line: reference pattern of clean Pt(997) at 400 K. $\phi_i = 54.0^\circ$, $\lambda = 1.02\text{\AA}$.

B) 1 ML Co on top of 1 ML Ag on Pt(997)

The He intensity in the $n = -3$ diffraction peak as a function of temperature (see figure 9.4 b) is characterized by a small initial value (at 250 K) which increases during heating, reaching a value comparable to a Pt(997) surface covered with a Ag monolayer above 700 K.

After deposition of Co on top of the Ag layer, the surface is very disordered as indicated by a very small He intensity in $n = -3$ (figure 9.4 b) and in the other diffraction orders (see figure 9.6). Evaluation of the Co Auger line for this system asserts that a substantial part

of the Co is still on the Ag layer. The disordering is probably due to partial incorporation of Co atoms into the Ag layer during deposition, as observed for Co deposition on top of 2 Ag monolayers on Pt(111) [130].

Heating the multilayer might first induce a complete inversion of the Ag and Co stacking. The continuous decrease of the Co Auger line (see inset in figure 9.4 b) within increasing temperature shows that the incorporation begins already at low temperature and even at the deposition (250 K). The Co Auger line at 500 K exhibits a similar intensity as at 250 K for the 1 ML Co + 1 ML Ag system. One may assume that at this temperature the stacking of the Ag-Co layers becomes inverted, although the actual position of the Co atoms may not be confined to a single layer. The layer inversion is corroborated by the observation that the intensity variations in the $n = -3$ peak (figure 9.4 b) at temperatures above 550 K are very similar to the case of the 1 ML Ag on top of 1 ML Co system (figure 9.4 a). Further heating finally leads to diffusion of Co into the bulk, which is indicated as in the previous case by a steep He intensity increase around 680 K (figure 9.4 b). This temperature is again about 100 K larger than the value for a single Co monolayer.

The large amount of disorder at the surface after deposition of the Co monolayer on top of Ag is similar to the behavior reported by Kingetsu [131] during the growth of Pt-Ag-Co sandwiches. The large lattice mismatch between Co and Ag may be one reason for this. Thermodynamic arguments may also be proposed: the large Co surface energy might be responsible for the disorder, as a large interface energy is necessary to force the 2D-growth. The Ag-Co interface energy is probably not sufficient to stabilize a Co 2D-layer, while the Pt-Co interface energy can. In comparison, the Ag surface energy [132, 133] is about two times smaller than that of Co, and Ag tends to form a floating 2D-layer at the surface.

9.4 Summary

Heating experiments have shown that Co always diffuses into the bulk Pt substrate. The deposition of a Ag layer on top of Co, however, stabilizes the Co layer, increasing the temperature of the bulk diffusion as well as the occurrence temperature of surface disordering. Co deposited on top of Ag is shown to give rise to a disordered surface already during deposition at 250 K. This behavior is not well suited in order to grow a 1D-superlattice. The possible creation of such a structure will thus be related to the finding of other elements exhibiting preferentially the behavior of Ag.

Chapter 10

Design of a new Diffractive Analysis Spectrometer (DAS)

10.1 Introduction

As explained in section 3.1, the DAS spectrometry is a promising method to overcome the limits of energy resolution encountered by the TOF method. This concept has been implemented in our experimental installation. So far, however, energy analysis has not been efficiently performed with the original setup. This is related to problems with the rigidity of the analyzer crystal holder and to the limited number of motorized degrees of freedom for analyzer crystal adjustment. Moreover, the available energy range is rather small in the original setup. To overcome these limitations, a new DAS spectrometer has been designed. The DAS spectrometer is not yet installed. Tests have however been performed under atmospheric pressure, that demonstrate the absolute positioning accuracy of this spectrometer.

In section 10.2, the design of the new DAS spectrometer is presented. In section 10.3, its operation is described and an estimation of the available energy resolution with the new configuration is given.

10.2 New experimental setup

The new experimental setup is represented in side and top views in figures 10.1 and 10.2 respectively. A schematic representation containing the important setup dimensions is given in figure 10.3. The difference with the original setup of chapter 3 resides in the analysis-detection unit. The two other modules (source and sample chamber) are unchanged. The available scattering angles are as well unchanged, as the modifications do not concern the Megatorque rotary table.

Figure 10.1: Side-view of the He-surface spectrometer equipped with the new DAS spectrometer.

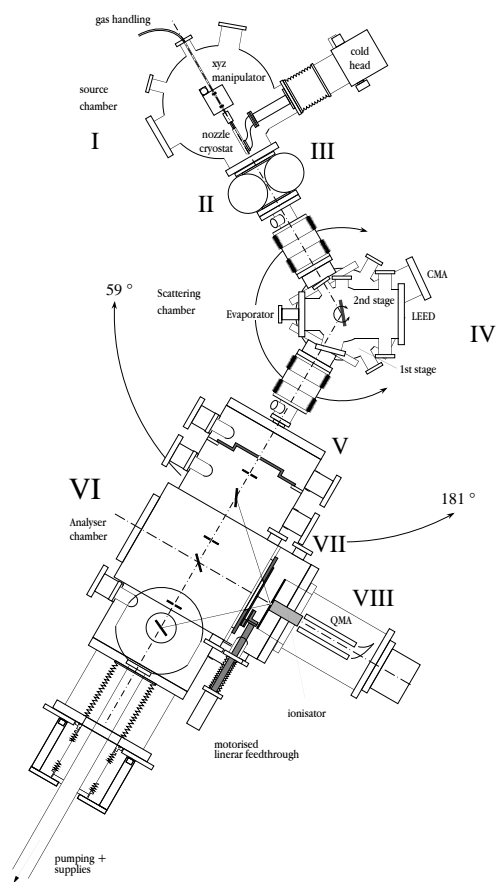


Figure 10.2: Top-view of the He-surface spectrometer equipped with the new DAS spectrometer.

Figure 10.3: Schematic sketch of the TEAS instrument equipped with the new DAS spectrometer.

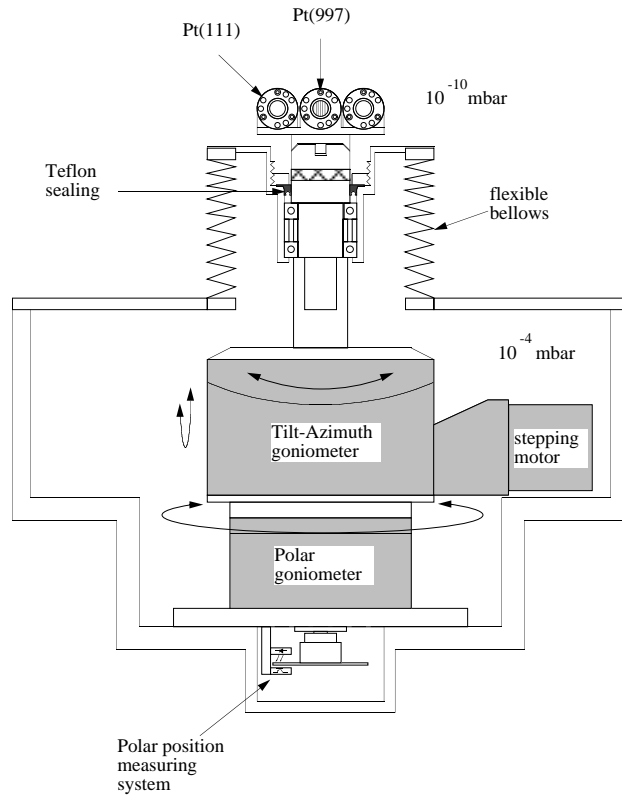


Figure 10.4: Side-view of the analyzer angular positioning system ("the bell").

flexible bellows. The absolute position of the polar angle is controlled by a commercial rotary position measuring system (ERO 1251 from Heidenhain), with a precision of better than 0.001° . This device has already been used successfully in the original DAS spectrometer [134]. The absolute positioning of the tilt and azimuth angles is less crucial to the resolution of the apparatus, because no large corrections are expected to be necessary during an energy scan. The positions of these axes are thus measured by counting the steps of the stepping motors. Preliminary measurements have shown that the positional reproducibility is better than 0.01° and thus sufficient. A photo-interruptor locates a reference position for each goniometer movement. This allows to recalibrate the absolute value of the angles if they have been lost.

The bell is fixed at the end of a rigid tube, that has multiple functions: it is the mechanical link between the bell and the rest of the sample holder, it allows the pumping of the bell, and it provides the feedthroughs for the thermocouples and for the supply of the stepping motors, the positioning devices, and the crystal heating. A UHV airtight bellows, welded to the tube at one end, and to the main chamber at the other, follows the xyz movements of the sample holder. As this bellows is relatively large (160 mm diameter), the force of the atmospheric pressure would be about 160 kg. This force would then be transferred to the linear translational stages and could damage them. To reduce this force, a compensator (figure 10.5) has been mounted outside the chamber. It is composed of two small bellows surrounding a tube. Its function is to allow the volume inside the large bellows to be pumped by a roughing pump. A shaft sealing between the compensator and the tube achieves the hermeticity during the movement in the z direction, while the x and y displacements are followed by the deformation of the compensator. This system reduces the force on the linear motion devices to 25 kg, which is acceptable.

For measurements in which no energy analysis is necessary, the presence of the analyzer crystal is rather a disadvantage, as it results in a substantial loss of intensity. A flat surface specularly deflecting the scattered beams into the detector would be a better choice. For this reason, the sample holder can be equipped with up to three samples. The central mount is reserved to the vicinal analyzer crystal (e.g. Pt(997)), that must be positioned on the rotation axis of the goniometers, while the lateral mounts are available for flat surfaces (e.g. Pt(111)) or a fluorescent screen (see figure 10.4).

With the installation of the new DAS spectrometer, the detector part will also be modified. As the time resolution of the detector is no more important in a DAS spectrometer, it is possible to increase the detection efficiency. During my diploma thesis [135], I have built and tested an electron ionisation detector working in the following manner: the ionisation part is modified according to the Stern-Pirani principle; *i.e.* the ionisation volume is hermetically closed. Only one small aperture allows the entry of the neutral beam, which is trapped in the volume, and an other small aperture allows the exit of the ions. By choosing the size of these apertures correctly, it is possible to significantly increase

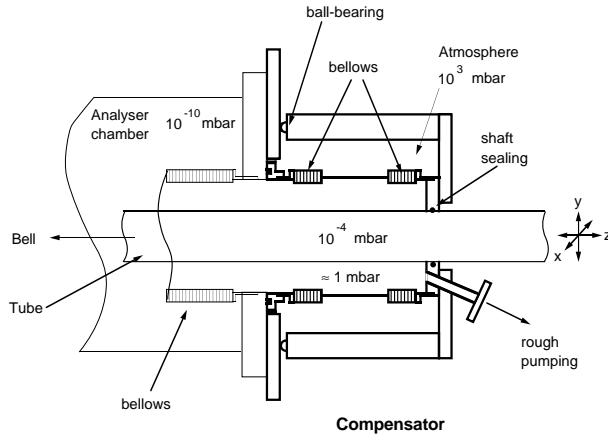


Figure 10.5: Schematic sketch of the compensator.

the ionisation probability of a He atom. The detector reaches a detection efficiency near 10^{-4} . The time resolution (originally $5 \mu\text{s}$) is largely reduced to 5 ms, which however is still negligible compared to typical intensity integration times of 1 s.

10.3 Operation of the new DAS spectrometer

10.3.1 Energy analysis

The geometric scheme of the new DAS spectrometer is sketched in figure 10.6. Only the z and polar degrees of freedom are represented. The other degrees of freedom (y , z , tilt and azimuth) are only meant to be small corrections. The range of z is $\pm 250 \text{ mm}$. The zero position is defined as being just in front of the detector entrance. The range of the polar angle (Θ) is $0 - 270^\circ$. The angular zero reference is taken for the crystal parallel to the beam.

The selected energy is a function of z and Θ , and for the same energy there exists *a priori* an infinity of possible (z , Θ) doublets. However z and Θ have to be linked. This link is forced by the finite terrace width distribution of the analyzer crystal. The effect of this distribution is to broaden the diffraction peaks with the increasing distance from the ideal condition (see [40]). As this broadening induces a substantial loss of energy resolution, it has to be avoided. Therefore, the (z , Θ) doublet must be such that the

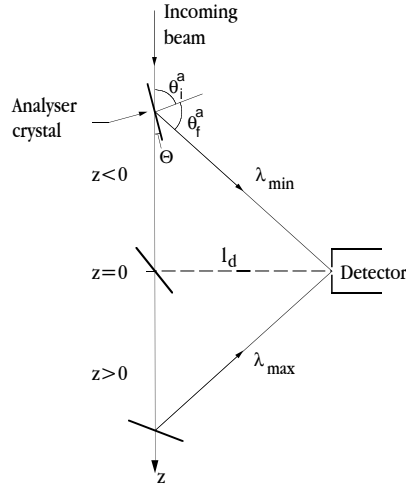


Figure 10.6: Scheme of the DAS.

diffraction peak for the selected energy is in the ideal condition. This is expressed by $\theta_i^a - \alpha = \theta_f^a + \alpha$.

If l_d is the distance between the detector entrance and the z -axis, geometric considerations show that:

$$\frac{z}{l_d} = \tan \left(\theta_i^a + \theta_f^a - \frac{\pi}{2} \right) \quad (10.1)$$

By introducing the ideal condition in these formulas, we find a relation between z and $\Phi = (\theta_i^a + \theta_f^a)/2$ as defined in section 3.3.2.

$$\Phi = \frac{\pi}{4} - \frac{1}{2} \arctan \left(\frac{z}{l_d} \right) \quad (10.2)$$

From $\Theta = \frac{\pi}{2} - \theta_i^a$, we obtain Θ as a function of z :

$$\Theta = \frac{\pi}{4} - \alpha + \arctan \left(\frac{z}{l_d} \right) \quad (10.3)$$

From eq. 3.7, the selected wavelength corresponding to the geometry can be induced:

$$\lambda = \frac{2h}{n} \cos \left(\frac{\pi}{4} - \frac{1}{2} \arctan \left(\frac{z}{l_d} \right) \right). \quad (10.4)$$

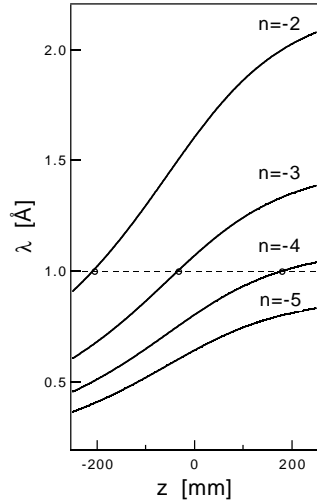


Figure 10.7: Available wavelengths as a function of z for $n = -2$ to -5 , calculated with eq. 10.4. The dashed line shows that a given wavelength (here 1 \AA) can be selected with several geometries depending on the diffraction order n .

One can note that the solution of the last equation is not unique as it depends on the diffraction order n . It may constitute a problem for the absolute wavelength determination. However, it is generally possible to select the same wavelength in at least two different geometries corresponding to two different n (see figure 10.7). This leads to the unique determination of the wavelength. The wavelength range which can be unambiguously analyzed by the diffraction grating, without overlapping of wavelengths, is called the free spectral range. It depends on the diffraction order n according to the formula 10.5 [136]:

$$(\Delta\lambda)_{fsr} = \lambda/n \quad (10.5)$$

10.3.2 Energy resolution

Different contributions determine the energy resolution of a TEAS apparatus. The nature of the contributions depends on the method used for the energy analysis. In a TOF

spectrometer, the resolution limit is determined by the time spread of the He-atoms at the detector. The different contributions are thus mainly the shutter function of the beam chopper, the finite length of the ionisation region, the length of the flight path and the energy spread of the primary beam. In a DAS spectrometer the resolution limit lies in the wavelength spread of the He-atoms at the detector. It is mainly determined by the size of the beam, the finite size of the detector aperture, the positioning precision of the analyzer crystal, the mosaic spread of the analyzer crystal and the energy spread of the primary beam.

One can note that the energy spread contribution is common for both methods. This contribution is inherent to the source and is only in rare cases lower than $\Delta E/E = 1.4\%$ in absence of a separate monochromatization system. An increase of the stagnation pressure inside the nozzle could narrow the energy distribution but would cause a huge increase of the gas load in the nozzle chamber, which would necessitate the use of a very powerful pump. The energy spread contribution is thus not characteristic of the energy analysis method and can be omitted in the further discussion concerning the intrinsic energy resolution of the new DAS spectrometer.

The first contribution to consider is the precision of the positioning. It introduces an uncertainty in the energy determination. From a Taylor expansion of eq. 10.4, one can calculate that an error in the z position of $5 \mu\text{m}$ corresponds to a relative error on the energy $\Delta E/E = 2 \cdot \Delta z/\lambda$ of about 0.002% . The value is even smaller for an error of 0.001° in Θ . The available precision of positioning is thus not the limitation for the energy resolution.

The mosaic spread of the analyzer crystal is the second contribution to consider. A homogeneous mosaic spread of the analyzer surface broadens the diffraction peaks and therefore reduces the energy resolution. However, a careful preparation of the crystal may reduce the mosaic spread to values smaller than 0.006° [137], which gives a contribution of 0.2% to the energy resolution [40]. The mosaic spread is a contribution to take into account but is presently not an essential limitation for the energy resolution.

The resolution limitation resides in the size of the beam and the aperture size of the detector. The effect of these contributions depends on the performed experiment and a simple expression of the energy resolution does not exist. In the next sections, we consider two experiments that give in some way the lower and upper limits for the energy resolution of the spectrometer. The first one is the direct beam energy analysis. This case minimizes the beam size effect and constitutes approximately the lower limit of the resolution. The second case is the worst case imaginable: it analyses the energy of the beams scattered from a surface, which is assumed to radiate a diffuse and completely polychromatic beam from its entire illuminated area.

A) Direct beam analysis

The setup is schematically sketched in figure 10.8, with the essential dimensions for the calculations. The diaphragm determining the beam divergence is d_m of figure 10.3 and the detector aperture size is d_d .

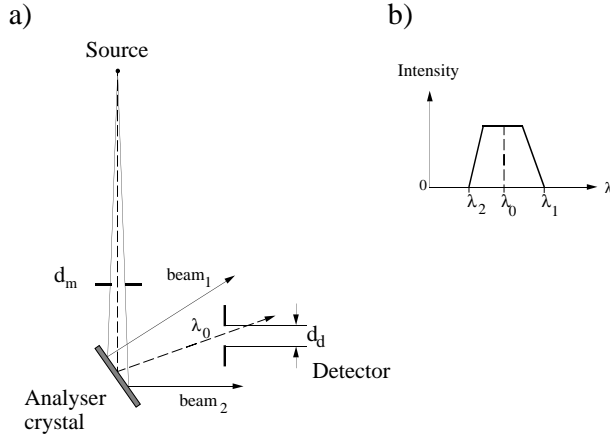


Figure 10.8: a) Schematic setup for direct beam energy analysis. b) Expected intensity profile during a wavelength-scan for a monochromatic beam. beam₁ and beam₂ are the trajectories limiting the diffracted beam.

The beam is supposed to be perfectly monochromatic with a wavelength λ_0 . Due to the finite divergence of the beam, the diffracted beam has a certain size at the detector entrance. During a wavelength-scan of the spectrometer according to the procedure described in section 10.3.1, the intensity in the detector is recorded as a function of the selected wavelength (figure 10.8 b). Thus the perfectly monochromatic beam displays a certain apparent wavelength distribution (λ_1 to λ_2) which is the wavelength resolution of the experiment. In a reasonable approximation, the energy resolution can be defined as:

$$\frac{\Delta E}{E} = 2 \cdot \frac{\Delta \lambda}{\lambda} = 2 \cdot \frac{\lambda_1 - \lambda_2}{\lambda_0} \quad (10.6)$$

The diffraction properties of the Pt(997) surface combined with simple geometric considerations allow the determination of the limit wavelengths and then the energy resolution. Figure 10.9 shows the energy resolution obtained for typical dimensions of the setup. It is slightly below 1%, and depends on the selected wavelength and the diffraction order. It

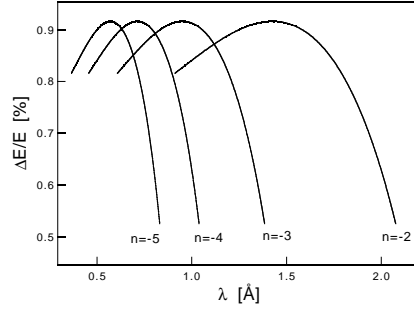


Figure 10.9: a) Intrinsic energy resolution of the new DAS spectrometer as a function of the selected wavelength, in the case of direct beam energy analysis. $n = -5$ to -2 , $d_d = 0.1$ mm, $d_m = 0.1$ mm.

exhibits a maximum (worst resolution), the origin of which is purely geometric: for each n , the maximum corresponds approximately to $z=0$, i.e. the position where the detector entrance is “seen” by the analyzer crystal under the largest solid angle. To improve the resolution further, it is necessary to reduce the size of the diaphragm d_m and the size of the detector aperture d_d . It is planned to do so by introducing additional slits mounted on micrometer linear feedthroughs.

Expression (10.6) is a useful tool to study the dependence of the energy resolution on diaphragm sizes and wavelength. However, it is not the only possible expression, as it depends on the definition of energy resolution. To illustrate this point, let us consider the above experiment from the point of view developed by Comsa in [21] and refined later [55]. This approach is different from the one discussed above as it assumes a gaussian beam profile. The schematic sketch of the experiment is given in figure 10.10, including the dimensions necessary for the calculation.

Neglecting the primary beam energy spread and the sample mosaic, the origin of the diffracted beam angular size at the detector entrance is purely geometric. It is given by the formula 10.7:

$$\Delta_g \theta_f = \sqrt{\left(\frac{\cos(\theta_i^a)}{\cos(\theta_f^a)} \delta_s + \frac{\cos(\theta_f^a) l_s}{\cos(\theta_i^a) l_d} \delta_s \right)^2 + \left(\frac{d_d}{l_d} \right)^2} \quad (10.7)$$

To be able to distinguish between two wavelengths different by $\Delta\lambda$, it is necessary that the angular separation performed by the analyzer crystal is larger or equal to the diffracted beam angular aperture. The angular separation for a Pt(997) surface is obtained by

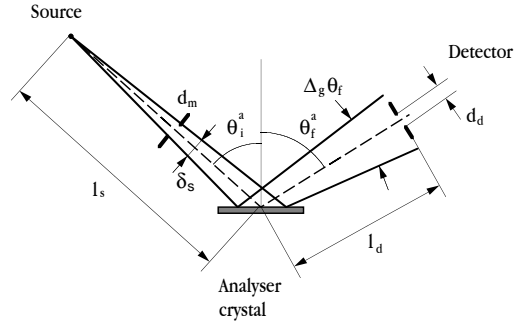


Figure 10.10: Schematic setup of the direct beam analysis experiment.

Taylor expansion of the 1D-Bragg equation 3.1.

$$\Delta_{sep}\theta_f = \frac{n}{d \cos(\theta_f^a)} \Delta\lambda \quad (10.8)$$

The energy resolution can be induced by equating 10.7 with 10.8:

$$\frac{\Delta E}{E} = 2 \cdot \frac{\Delta\lambda}{\lambda} = \frac{d \cos(\theta_f^a)}{n\lambda} \Delta_g\theta_f \quad (10.9)$$

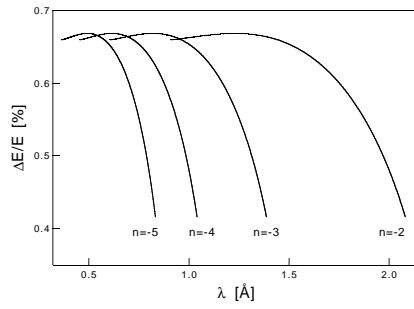


Figure 10.11: Energy resolution obtained with eq. 10.9. $d_m = 0.1 \text{ mm}$, $d_d = 0.1 \text{ mm}$, $n = -2$ to -5 .

Figure 10.11 shows the intrinsic energy resolution of the spectrometer obtained with Comsas approach for the same diaphragm sizes as before. It is slightly better than with the

first approach. This comes from the different criteria used in the definition of the energy resolution. The first approach uses a criterion more drastic than the one by Comsas, as it assumes that, to be resolved, two wavelengths must absolutely not overlap.

Both criteria are somewhat arbitrary and there is no reason to choose one rather than the other. Both approaches give a same order of magnitude estimate, usable for the optimization of the setup parameters.

B) Polychromatic scattering

The situation of a complete surface scattering experiment is now treated. There is *a priori* no information about the inelastic scattering processes occurring at the surface. Therefore, the worst case has to be considered. Each illuminated point of the surface is assumed to reemit in all directions a polychromatic beam. It is possible to give a reasonable estimate of the energy resolution, similarly to the case of direct beam analysis.

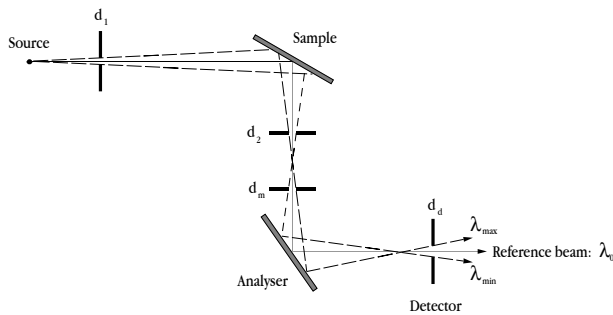


Figure 10.12: Sketch of the double scattering experiment. Each point of the sample surface hit by the incident beam is assumed to reemit a polychromatic beam in all directions. The analyzer crystal is supposed to be perfect and $\theta_i^s = \theta_f^s = 45^\circ$ is assumed.

Figure 10.12 represents the geometry of the experiment. The analyzer crystal geometry selects the wavelength λ_0 . However, different wavelengths can also enter the detector. The trajectories of the extreme wavelengths λ_{max} and λ_{min} able to enter the detector are sketched. The energy resolution can again be defined as:

$$\frac{\Delta E}{E} = 2 \cdot \frac{\Delta \lambda}{\lambda} = 2 \cdot \frac{\lambda_{max} - \lambda_{min}}{\lambda_0} \quad (10.10)$$

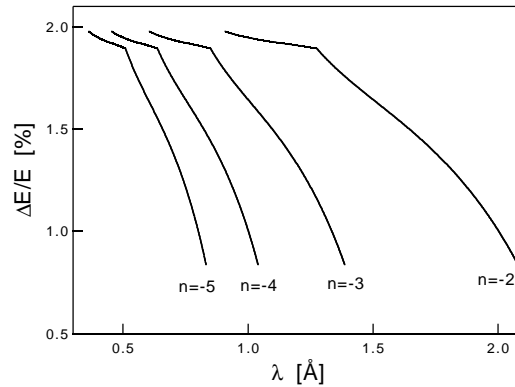


Figure 10.13: Energy resolution for the double scattering experiment. $d_d = 0.1$ mm, $d_m = 0.1$ mm, $d_2 = 0.1$ and $d_1 = 0.15$ mm. $n = -2$ to -5 .

The extreme wavelengths and then the energy resolution can be calculated in an exact way from geometric considerations as before. The computer code can be found in Appendix C. For the calculation, the incidence (θ_i^s) and exit (θ_f^s) angles at the sample are fixed to 45° . Figure 10.13 shows typical results for the same diaphragm sizes d_d and d_m as in the previous case. The discontinuity of the curves is due to the specific geometry of the setup: the size of the sample area which can reemit beams into the detector is determined by the diaphragms d_2 and d_m . However, as the distance between d_2 and d_m is not fixed (d_m moves with the analyzer crystal), this size is not constant during a scan. In particular, when the diaphragms are far enough from each other, the sample area “seen” by the analyzer is smaller than the effective area illuminated by the primary beam (left branches in the curves in figure 10.13).

Energy resolutions between 0.8 and 1.8 % are obtained for this worst case. The “real” resolution of the DAS spectrometer is, however, expected to be much better, approaching the energy resolution obtained for direct beam analysis.

10.3.3 Energy calibration

An absolute determination of the selected energy is obviously necessary. Even if the setup is mechanically aligned as well as possible so that Θ and z are known with a good precision, the remaining error will still be unacceptably large. The final calibration of the spectrometer must thus be made *in situ*.

This corresponds to solving a problem with three unknowns: Θ_0 and z_0 (the initial values of Θ and z) and λ (the energy of the primary beam). All the relative changes of Θ and z are measured with high accuracy. The procedure presented here takes advantage of the properties of the Pt(997) diffraction pattern. It requires to find two geometries (i.e. two (z, Θ) doublets), so that the diffraction condition for the direct beam is ideal (see chapter 3). The ideal condition is known to be reached when the width of the Θ -scan performed for a fixed z has a minimum value. The precision for finding an ideal condition depends on the slope of the λ vs z curve (see figure 10.7). For $n = -3$, the precision is about 0.05° in Θ , which corresponds to an error of about 0.5% in the absolute determination of λ . This absolute error does however not modify the energy resolution discussed above, which is a relative value. In ideal condition, it is known that: $\theta_i^a - \alpha = \theta_f^a + \alpha = \Phi$ and $\cos(\Phi) = \frac{n\lambda}{2h}$.

From this equation for two different n , it is possible to eliminate λ and determine Θ_0 . Then λ can be determined and finally z_0 can be deduced from inverting eq. 10.4. One may object that the n values are also unknown. In principle they are, but in fact a knowledge of the approximate geometry and the approximate wavelength is sufficient to determine them.

Two ideal conditions are thus sufficient to calibrate the spectrometer. It is indeed possible for about every wavelength of the primary beam as can be seen in figure 10.7.

10.4 Summary

The concept and realization of a new DAS spectrometer has been described in this chapter. This spectrometer works with a Pt(997) vicinal surface as a diffraction grating for the He matter waves. Its energy resolution is predicted to be smaller than $\sim 1\%$, which is the technological limitation of usual TOF spectrometers. The calibration of the DAS spectrometer is possible with a good accuracy, taking advantage of the “ideal” conditions of diffraction on Pt(997). The new spectrometer will be mounted on the rest of the experimental set-up in the next months, which will allow studies of inelastic processes at surfaces.

Chapter 11

Outlook

The present thesis deals with growth of rare gas and metallic layers at vicinal surfaces. It focuses on the effect of the step as an energy potential well for the adsorbates, which gives rise to the particular row-by-row growth mode observed for the elements (Xe, Kr, Ag, and Co) deposited on the studied vicinal surfaces (Pt(997) and Pt(779)).

The present work demonstrates that it is possible to create, in a controlled manner, a regular array of monatomic wires for a wide variety of elements including Co. The magnetic properties of such a structure is of fundamental interest [2] and deserves to be studied. In this perspective, mounting of a SMOKE (Surface Magneto-Optic Kerr Effect) apparatus on the TEAS instrument may be an interesting extension of the set-up.

The precise calibration of the coverage by grazing incidence TEAS gives the possibility to grow 1D-superlattices on the Pt(997) vicinal surface, although the growth cannot be monitored after two rows. For this purpose, a triple evaporator has been mounted on the sample chamber to deposit rows of different elements successively on the surface. The realization of such a superlattice will, however, be related to the finding of elements (if possible magnetic) which do not alloy, as Co and Pt do. In addition, it would be convenient to find vicinal surfaces (or a way to prepare them) with narrower terrace width distributions than the Pt(997) and Pt(779) surfaces. A look at Si vicinal surfaces might be interesting in this perspective.

Theoretical efforts, in order to reproduce the He diffraction pattern of Pt(997) and in particular the shift observed between the form factor maximum and the diffraction peaks in ideal condition, could lead to a better understanding of helium-surface interactions at vicinal surfaces.

The mounting of the new DAS spectrometer will give access to the inelastic processes at surfaces. Its good energy resolution coupled to the wide accessible angular range of the instrument are promising for the future studies. In particular, surface phonons at the vicinal surfaces might present interesting results. Theoretical calculations performed on the dynamics of a confined Xe monolayer on Pt(997) [138, 139] give different localized

vibration modes depending on the structure of the monolayer. This difference could help to elucidate the discrepancy between the theoretical and experimental structures of Xe/Pt(997) evoked in chapter 6. Finally, for bare metal vicinal surfaces, the study of the vibration modes localized at the step might provide insight to the electronic redistribution at step edges [140].

Appendix A

In this appendix, we will model the He intensity in the $n = 0$ diffraction peak as a function of temperature, in the case where a single row of rare gas atoms is adsorbed at the step of a Pt(997) surface. The purpose of this model is to infer the excess binding energy in the row with respect to the rest of the terrace sites.

The starting situation is sketched in figure A.1. We consider a single terrace. It is composed of n_s step sites and n_t terrace sites. The adsorption energy in the step sites is supposed to be larger than the adsorption energy in the terrace sites by a quantity ΔE . The terrace sites are assumed energetically equivalent. We deposit on this terrace the amount of atoms necessary to form a full row, i.e. n_s atoms.

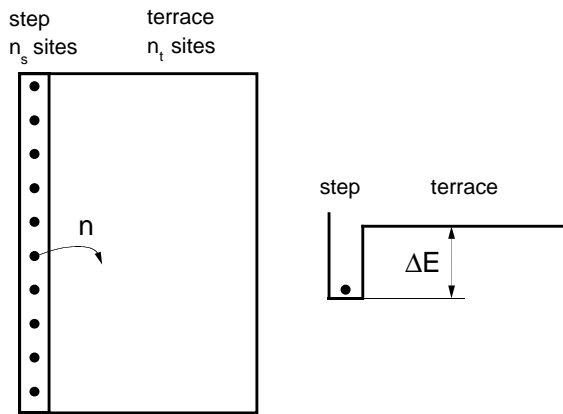


Figure A.1: Sketch of the system and energy diagram.

In equilibrium at finite temperature, the step sites are not completely occupied. It is convenient to call n the number of unoccupied sites at the step. The first stage of the

model is to determine the vacancy ratio (n/n_s) of the step sites at a given temperature T . Therefore, we use statistical thermodynamics. We have to minimize the free energy F of the system with respect to n :

$$\frac{\partial F}{\partial n} = \frac{\partial(E - TS)}{\partial n} = 0 \quad (\text{A.1})$$

where E is the energy of the system and S is its entropy.

The energy of the system is equal to $(n - n_s) \cdot \Delta E$ if we assume that the energy in a terrace site is equal to zero.

The entropy is found by combinatory analysis. We call W the number of possible equivalent combinations to place $n_s - n$ atoms at the step and n atoms on the terrace. W is given by:

$$W = \frac{n_s!}{n! (n_s - n)!} \cdot \frac{n_t!}{(n_t - n)! n!} \quad (\text{A.2})$$

From elementary statistical thermodynamics:

$$S = k_B \ln W \quad (\text{A.3})$$

where k_B is the Boltzmann constant.

We can thus rewrite eq. A.1:

$$\frac{\partial W}{\partial n} = \beta \cdot \Delta E \quad (\text{A.4})$$

where $\beta = 1/k_B T$.

Using the Stirling formula to approximate the logarithm of a factorial when its argument is very large, we obtain from eq. A.4:

$$\frac{n^2}{(n_s - n)(n_t - n)} = e^{-\beta \Delta E} \quad (\text{A.5})$$

The vacancy ratio at the step, n/n_s , can be inferred:

$$\frac{n}{n_s} = \frac{-(n_s + n_t) + \sqrt{4(e^{\beta \Delta E} - 1) n_s n_t + (n_s + n_t)^2}}{2n_s (e^{\beta \Delta E} - 1)} \quad (\text{A.6})$$

In the following discussion, it is convenient to redefine the vacancy ratio at the step and to call it defect coverage at the step $\Theta_{step} = n/n_s$.

The second stage of the model is to relate the defect density coverage to the intensity in the $n = 0$ peak. To do so, it is necessary to make several assumptions:

- The intensity in the $n = 0$ diffraction peak originates exclusively from a stripe of width d at the step (see figure A.2).

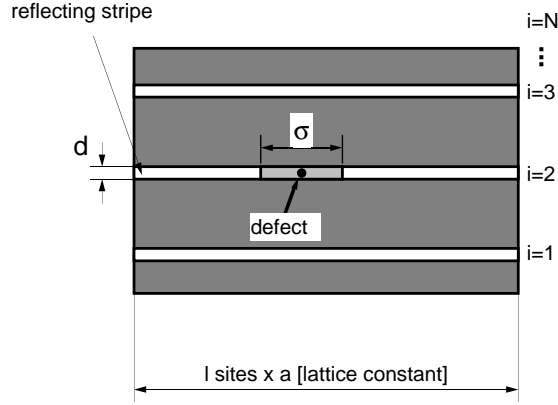


Figure A.2: Scheme of the reflective surface.

- A defect at the step kills the reflectivity for a stripe of length σ , its diffuse scattering linear section.

The scheme of the reflective surface is shown in figure A.2. The total reflective area in absence of defect at the step, i.e at $T = 0$, is given by $d \times l \times a \times N$. A coverage density at the step Θ_{step} decreases the reflective area of a quantity $d \times \sigma \times \Theta_{step} \times l \times N$. The last formula implicitly assumes that the defect areas do not overlap, which is correct at low temperature.

The intensity in the $n = 0$ peak is obtained by:

$$I(\theta_{step}) = I_0 \cdot \left(\frac{d \cdot N \cdot l \cdot a - d \cdot \sigma \cdot \Theta_{step} \cdot l \cdot N}{d \cdot N \cdot l \cdot a} \right) = I_0 \cdot \left(1 - \Theta_{step} \cdot \frac{\sigma}{a} \right) \quad (\text{A.7})$$

where θ_{step} , given by eq. A.6, contains the temperature dependence of the intensity.

In the case where the diffuse scattering sections of the defects overlap, it is possible to generalize the previous formula:

$$I(\Theta_{step}) = I_0 \cdot \left(1 - \Theta_{step} \cdot \frac{\sigma}{a} \right)^{\frac{a}{\sigma}} \quad (\text{A.8})$$

This formula contains two independent parameters to fit the data of chapter 4 and 7: ΔE and σ . The most interesting parameter is of course the excess binding energy at the step ΔE .

Appendix B

This software is written for the program Matlab. It calculates the root mean square deviation of the terrace width distribution of a Pt(997) surface during Ag adsorption, making the assumptions of chapter 8.

```
nbsteps=1000;
stddev=1.5;
Nnom=8.33;

nbrows=Nnom+stddev*randn(nbsteps,1);
std(nbrows)
counter=0;
counterfinal=50;
[s1,s2]=size(nbrows);
nbrowsPt=nbrows;
nbrowsauxPt=nbrows;
nbrowsAg=ones(s1,s2)-1;
nbrowsauxAg=ones(s1,s2)-1;
deviation=[std(nbrows)];
Agcover=0;
dAgcoverage=1/counterfinal;
while counter<counterfinal,
for i=1:(nbsteps-1),
nbrowsauxPt(i)=nbrowsPt(i)-dAgcoverage*nbrows(i);
nbrowsauxAg(i)=nbrowsAg(i)+dAgcoverage*nbrows(i+1);
end;
nbrowsauxPt(nbsteps)=nbrowsPt(nbsteps)-dAgcoverage*nbrows(nbsteps);
nbrowsauxAg(nbsteps)=nbrowsAg(nbsteps)+dAgcoverage*nbrows(1);
nbrowsPt=nbrowsauxPt;
nbrowsAg=nbrowsauxAg;
```

```
terrwidth=nbrowsPt+nbrowsAg;
deviation=[deviation,std(terrwidth)];
counter=counter+1;
end;
coverage=(0:1:counterfinal)/counterfinal;
plot(coverage,deviation);
```

Appendix C

This software is written for the program Matlab. It calculates the energy resolution in the case of a double scattering experiment with a sample reemitting a polychromatic beam in all directions from all the points of its illuminated area (see chapter 10).

Geometrical parameters (generally in mm)

```
D=20.02;
d1=0.15;
lbdia=188;
deltas=d1/lbdia;
z=-250:1:250;
ls=750;
lsd2=530;
ld2dm=320+z;
ldma=80;
lsdm=lsd2+ld2dm;
ldneutre=270;
dm=0.1;
d2=0.1;
dd=0.1;
dr=pi/180;
tis=45*dr;
tfs=45*dr;
alpha=6.45*dr;
ti=(pi/4-1/2*atan(z/ldneutre))+alpha;
tf=ti-2*alpha;
```

Illuminated area on the sample

```
asmax=ls*sin(deltas/2)./cos(tis-deltas/2);
asmin=ls*sin(deltas/2)./cos(tis+deltas/2);
```

```

xsmax=asmax*cos(tfs);
ysmax=asmax*sin(tfs);
xsmin=asmin*cos(tfs);
ysmin=asmin*sin(tfs);

```

a) First approach: the diaphragms d2 and dm limit the areas of the sample ‘‘seen’’ from the analyser

Illuminated area on the analyser

```

xamax=((d2+dm)*(ld2dm+ldma)-d2*ld2dm)/(2*ld2dm-(d2+dm)*tan(ti));
yamax=xamax.*tan(ti);
xamin=((d2+dm)*(ld2dm+ldma)-d2*ld2dm)/(2*ld2dm+(d2+dm)*tan(ti));
yamin=xamin.*tan(ti);

```

Calculation of the incidence and diffraction angles of the limit trajectories on the analyser.

```

alphamax=atan((d2+dm)/(2*ld2dm));
timax=ti+alphamax;
alphamin=atan((d2+dm)/(2*ld2dm));
timin=ti-alphamin;

```

```

betaref=abs(pi/2-(ti+tf));
betamax=abs(betaref-atan(abs(z+yamax+dd/2)/(ldneutre-xamax)));
tfmax=tf-betamax;
betamin=abs(betaref-atan(abs(z-yamin-dd/2)/(ldneutre+xamin)));
tfmin=tf+betamin;

```

Calculation of the limit wavelengths and resolution

```

n=-2;
lambdamax2=D/n*(sin(tfmax)-sin(timax));
lambdamin2=D/n*(sin(tfmin)-sin(timin));
lambdaref2=D/n*(sin(tf)-sin(ti));
n=-3;
lambdamax3=D/n*(sin(tfmax)-sin(timax));
lambdamin3=D/n*(sin(tfmin)-sin(timin));
lambdaref3=D/n*(sin(tf)-sin(ti));
n=-4;
lambdamax4=D/n*(sin(tfmax)-sin(timax));
lambdamin4=D/n*(sin(tfmin)-sin(timin));

```



```

lambdaref4=D/n*(sin(tf)-sin(ti));
n=-5;
lambdamax5=D/n*(sin(tfmax)-sin(timax));
lambdamin5=D/n*(sin(tfmin)-sin(timin));
lambdaref5=D/n*(sin(tf)-sin(ti));
resoldia2=2*100*(lambdamax2-lambdamin2)./lambdaref2;
resoldia3=2*100*(lambdamax3-lambdamin3)./lambdaref3;
resoldia4=2*100*(lambdamax4-lambdamin4)./lambdaref4;
resoldia5=2*100*(lambdamax5-lambdamin5)./lambdaref5;

```

Second approach: the illuminated area on the sample limits the resolution.

Illuminated area on the analyser

```

xamax=(asmax*(cos(tfs)*ldma+sin(tfs)*dm/2)+dm/2*(lsdm+ldma))./. . .
(asmax*(sin(tfs)-cos(tfs)*tan(ti))+lsdm-dm/2*tan(ti));
yamax=xamax.*tan(ti);
xamin=(asmin*(cos(tfs)*ldma-sin(tfs)*dm/2)+dm/2*(lsdm+ldma))./. . .
(asmin*(-sin(tfs)+cos(tfs)*tan(ti))+lsdm+dm/2*tan(ti));
yamin=xamin.*tan(ti);

```

Calculation of the incidence and diffraction angles of the limit trajectories on the analyser.

```

alphamax=atan((xsmax+dm/2)./(lsdm+yymax));
timax=ti+alphamax;
alphamin=atan((xsmin+dm/2)./(lsdm-ysmin));
timin=ti-alphamin;

```

```

betaref=abs(pi/2-(ti+tf));
betamax=abs(betaref-atan(abs(z+yamax+dd/2)./(ldneutre-xamax)));
tfmax=tf-betamax;
betamin=abs(betaref-atan(abs(z-yamin-dd/2)./(ldneutre+xamin)));
tfmin=tf+betamin;

```

Calculation of the limit wavelengths and resolution

```

n=-2;
lambdamax2=D/n*(sin(tfmax)-sin(timax));
lambdamin2=D/n*(sin(tfmin)-sin(timin));
lambdaref2=D/n*(sin(tf)-sin(ti));

```

```

n=-3;
lambdamax3=D/n*(sin(tfmax)-sin(timax));
lambdamin3=D/n*(sin(tfmin)-sin(timin));
lambdaref3=D/n*(sin(tf)-sin(ti));
n=-4;
lambdamax4=D/n*(sin(tfmax)-sin(timax));
lambdamin4=D/n*(sin(tfmin)-sin(timin));
lambdaref4=D/n*(sin(tf)-sin(ti));
n=-5;
lambdamax5=D/n*(sin(tfmax)-sin(timax));
lambdamin5=D/n*(sin(tfmin)-sin(timin));
lambdaref5=D/n*(sin(tf)-sin(ti));

resoltache2=2*100*(lambdamax2-lambdamin2)./lambdaref2;
resoltache3=2*100*(lambdamax3-lambdamin3)./lambdaref3;
resoltache4=2*100*(lambdamax4-lambdamin4)./lambdaref4;
resoltache5=2*100*(lambdamax5-lambdamin5)./lambdaref5;

```

Final resolution obtained by minimization of both approaches.

```

resol2=min(resoldia2,resoltache2);
resol3=min(resoldia3,resoltache3);
resol4=min(resoldia4,resoltache4);
resol5=min(resoldia5,resoltache5);

```

References

- [1] J. Simonds, *Physics Today* **48**, 26 (1995).
- [2] J. Shen, R. Shomski, M. Klaua, H. Jenniches, S. Manoharan, and J. Kirschner, *Phys. Rev. B* **56**, 2340 (1997).
- [3] M. Crommie, C. Lutz, and D. Eigler, *Science* **262**, 218 (1993).
- [4] P. Avouris, *Accounts Chem. Res.* **28**, 95 (1995).
- [5] H. Röder, E. Hahn, H. Brune, J. Bucher, and K. Kern, *Nature* **366**, 141 (1993).
- [6] J. Bucher, E. Hahn, P. Fernandez, C. Massobrio, and K. Kern, *Europhys. Lett.* **27**, 473 (1994).
- [7] H. Brune, *Surf. Sci. Rep.* **31**, 121 (1998).
- [8] W. Kossel, *Akad. Wiss.* **1927**, 135 (1927).
- [9] D. Woodruff and T. Delchar, *Modern Techniques of Surface Science* (Cambridge Univ. Press, Cambridge, 1994).
- [10] G. Binnig, H. Rohrer, C. Gerber, and E. Weibel, *Phys. Rev. Lett.* **49**, 57 (1982).
- [11] G. Binnig, C. Quate, and C. Gerber, *Phys. Rev. Lett.* **56**, 930 (1986).
- [12] R. Feenstra, J. Stroscio, J. Tersoff, and A. Fein, *Phys. Rev. Lett.* **58**, 1192 (1987).
- [13] R. Hamers, R. Tromp, and J. Demuth, *Phys. Rev. Lett.* **56**, 1972 (1986).
- [14] S. Gwo, A. Smith, and C. Shih, *J. Vac. Sci. Technol. A* **11**, 1644 (1993).
- [15] E. Müller, *Z. Physik* **131**, 136 (1951).
- [16] E. Hulpke, *Springer Series in Surface Sciences 27* (Springer-Verlag, Berlin-Heidelberg, 1992).

- [17] B. Poelsema and G. Comsa, *Springer Tracts in Modern Physics, Vol. 115* (Springer-Verlag, Berlin-Heidelberg, 1989).
- [18] T. Engel and K. Rieder, *Springer Tracts in Modern Physics, Vol. 91* (Springer-Verlag, Berlin-Heidelberg, 1982).
- [19] K. Kern, R. David, R. Palmer, and G. Comsa, *Surf. Sci.* **175**, 669 (1986).
- [20] K. Rieder and T. Engel, *Phys. Rev. Lett.* **43**, 373 (1979).
- [21] G. Comsa, *Surf. Sci.* **81**, 57 (1979).
- [22] L. Gomez, S. Bourgeat, J. Ibanez, and M. Salmeron, *Phys. Rev. B* **31**, 2551 (1985).
- [23] J. de Miguel, A. Cebollada, M. Gallego, J. Ferron, and S. Ferrer, *J. Cryst. Growth* **88**, 442 (1988).
- [24] R. Kunkel, B. Poelsema, L. Verheij, and G. Comsa, *Phys. Rev. Lett.* **65**, 733 (1990).
- [25] A. Zangwill, *Physics at surfaces* (Cambridge University Press, Cambridge, 1988).
- [26] B. Poelsema, R. Kunkel, N. Nagel, A. Becker, G. Rosenfeld, L. Verheij, and G. Comsa, *Appl. Phys. A* **53**, 369 (1991).
- [27] K. Kern, R. David, R. Palmer, and G. Comsa, *Phys. Rev. Lett.* **56**, 620 (1986).
- [28] K. Yonehama and L. Schmidt, *Surf. Sci.* **25**, 238 (1971).
- [29] J. Lapujoulade, J. Perreau, and A. Kara, *Surf. Sci.* **129**, 59 (1983).
- [30] J. Toennies, *Springer Series in Surface Science 21* (Springer-Verlag, Berlin-Heidelberg, 1991).
- [31] A. Kantrowitz and J. Grey, *Rev. Sci. Instrum.* **22**, 328 (1951).
- [32] J. Toennies and K. Winkelmann, *J. Chem. Phys.* **66**, 3965 (1977).
- [33] K. Kuhnke, K. Kern, R. David, and G. Comsa, *Rev. Sci. Instrum.* **65**, 3458 (1994).
- [34] R. David, K. Kern, P. Zeppenfeld, and G. Comsa, *Rev. Sci. Instrum.* **57**, 2771 (1986).
- [35] G. Comsa, R. David, and B. Schumacher, *Rev. Sci. Instrum.* **52**, 789 (1981).
- [36] L. Verheij and P. Zeppenfeld, *Rev. Sci. Instrum.* **58**, 2138 (1987).
- [37] D.-M. Smiglies and J. Toennies, *Rev. Sci. Instrum.* **59**, 2185 (1988).

- [38] K. Kuhnke, E. Hahn, R. David, P. Zeppenfeld, and K. Kern, *Surf. Sci.* **27**, 118 (1992).
- [39] V. Marsico, Ph.D. thesis, Ecole Polytechnique Fédérale de Lausanne, 1995.
- [40] H. Schief, Ph.D. thesis, Ecole Polytechnique Fédérale de Lausanne, 1995.
- [41] K. Kern, R. David, and G. Comsa, *Rev. Sci. Instrum.* **56**, 369 (1986).
- [42] G. Mechttersheimer, Ph.D. thesis, Universität Bonn, 1981.
- [43] E. Hahn, Diploma thesis, Universität Bonn, 1990.
- [44] E. Hahn, H. Schief, V. Marsico, A. Fricke, and K. Kern, *Phys.Rev. Lett.* **72**, 3378 (1994).
- [45] N. Bartelt, T. Einstein, and E. Williams, *Surf. Sci. Lett.* **240**, 591 (1990).
- [46] E. Williams and N. Bartelt, *Science* **251**, 393 (1991).
- [47] G. Comsa, G. Mechttersheimer, B. Poelsema, and S. Tomoda, *Surf. Sci.* **89**, 123 (1979).
- [48] H. Hoinkes and H. Wilsch, in *Springer Series in Surface Sciences 27* (Springer-Verlag, Berlin-Heidelberg, 1992), Chap. 7.
- [49] J. Harris, A. Liebsch, G. Comsa, G. Mechttersheimer, B. Poelsema, and S. Tomoda, *Surf. Sci.* **118**, 279 (1982).
- [50] N. Ashcroft and N. Mermin, *Solid State Physics* (HRW, Orlando, Florida, 1987).
- [51] J. Manson, in *Springer Series in Surface Sciences 27* (Springer-Verlag, Berlin-Heidelberg, 1992), Chap. 8.
- [52] A. Levi and H. Suhl, *Surf. Sci.* **88**, 221 (1979).
- [53] V. Bortolani, V. Celli, A. Franchini, J. Idioldi, G. Santoro, K. Kern, B. Poelsema, and G. Comsa, *Surf. Sci.* **208**, 1 (1989).
- [54] N. Garcia, V. Celli, and F. Goodmann, *Phys. Rev. B* **19**, 634 (1979).
- [55] K. Kuhnke, Ph.D. thesis, Universität Bonn, 1991.
- [56] R. Smoluchowski, *Phys. Rev.* **60**, 661 (1941).
- [57] M. Ladd and R. Palmer, *Structure Determination by X-ray Crystallography* (Plenum Press, New York and London, 1977).

- [58] E. Preuss, B. Krahl-Urban, and R. Butz, *Laue Atlas* (Bertelsmann Universitätverlag, 1974).
- [59] J. Harris, B. Joyce, and P. Dobson, *Surf. Sci. Lett.* **103**, 90 (1981).
- [60] E. Vlieg, A. D. van der Gon, J. V. der Veen, J. MacDonald, and C. Norris, *Phys. Rev. Lett.* **61**, 2241 (1988).
- [61] G. Bassett, *Phil. Mag.* **3**, 1042 (1958).
- [62] H. Bethge, *Surf. Sci.* **3**, 33 (1964).
- [63] H. Röder, H. Brune, J.-P. Bucher, and K. Kern, *Surf. Sci.* **298**, 121 (1993).
- [64] P. Petroff, A. Gossard, and W. Wiegmann, *Appl. Phys. Lett.* **45**, 620 (1984).
- [65] Y. Mo and F. Himpsel, *Phys. Rev. B* **50**, 7868 (1994).
- [66] J. Merikoski, J. Timonen, and K. Kaski, *Phys. Rev. B* **50**, 7925 (1994).
- [67] K. Kern, R. David, P. Zeppenfeld, and G. Comsa, *Surf. Sci.* **195**, 353 (1988).
- [68] H. Brune, H. Röder, C. Boragno, and K. Kern, *Phys. Rev. B* **49**, 2997 (1994).
- [69] P. Zeppenfeld, S. Horch, and G. Comsa, *Phys. Rev. Lett.* **73**, 1259 (1994).
- [70] R. Miranda, S. Daiser, K. Wandelt, and G. Ertl, *Surf. Sci.* **131**, 61 (1983).
- [71] B. Cathrine, D. Fargues, M. Alnot, and J. Ehrhardt, *Surf. Sci.* **259**, 162 (1991).
- [72] B. Poelsema, G. Mechttersheimer, and G. Comsa, *Surf. Sci.* **111**, 519 (1981).
- [73] H. Schief, V. Marsico, K. Kuhnke, and K. Kern, *Surf. Sci.* **364**, 631 (1996).
- [74] J. Lapujoulade, Y. Lejay, and N. Papanicolaou, *Surf. Sci.* **90**, 133 (1979).
- [75] *Phase Transitions in Surface Films*, edited by J. Dash and J. Ruvalds (Plenum, New-York, 1980); *Phase Transitions in Surface Films 2*, edited by H. Taub *et al.* (Plenum, New-York, 1991); *Kinetics of Ordering and Growth at Surfaces*, edited by M.G. Lagally (Plenum, New-York, 1990).
- [76] M. Bienfait, *Surf. Sci.* **162**, 411 (1985).
- [77] J. Lapujoulade, in *Interactions of Atoms and Molecules with Solid Surfaces*, edited by V. Bortolani, N. March, and M. Tosi (Plenum, New York, 1990), p. 381; K. Wandelt, *Surf. Sci.* **251/252**, 387 (1991).

- [78] K. Kern, R. David, R. Palmer, and G. Comsa, Phys. Rev. Lett. **56**, 620 (1986).
- [79] B. Poelsema, A. Becker, G. Rosenfeld, R. Kunkel, N. Nagel, K. Verheij, and G. Comsa, Surf. Sci. **272**, 269 (1992).
- [80] P. Trischberger, H. Dröge, S. Gokhale, J. Henk, H.-P. Steinrück, W. Widdra, and D. Menzel, Surf. Sci. **377-379**, 155 (1997).
- [81] S. Horch, P. Zeppenfeld, and G. Comsa, Appl. Phys. A **60**, 147 (1995).
- [82] J. Tully, Surf. Sci. **226**, 461 (1981).
- [83] J. Gottlieb and L. Bruch, Phys. Rev. B **44**, 5750 (1991).
- [84] J. Black and P. Bopp, Phys. Rev. B **34**, 7410 (1986).
- [85] J. Black and R. Janzen, Phys. Rev. B **39**, 6238 (1989).
- [86] J. Black and R. Janzen, Surf. Sci. **217**, 199 (1989).
- [87] C. Arumainayagam, R. Madix, M. McMaster, V. Suzawa, and J. Tully, Surf. Sci. **226**, 180 (1990).
- [88] D. Bethune, J. Barker, and C. Rettner, J. Chem. Phys. **92**, 6847 (1990).
- [89] J. Barker and C. Rettner, J. Chem. Phys. **97**, 5844 (1992).
- [90] J. Müller, Phys. Rev. Lett. **65**, 3021 (1990).
- [91] R. Aziz and M. Slaman, Mol. Phys. **57**, 826 (1986).
- [92] J. Barker, in *Rare Gas Solids*, edited by M. Klein and J. Venables (Academic, London, 1976).
- [93] L. Bruch, Surf. Sci. **125**, 194 (1983), and references therein.
- [94] C. Ramseyer, C. Girardet, P. Zeppenfeld, J. Goerge, M. Büchel, and G. Comsa, Surf. Sci. **313**, 251 (1994).
- [95] P. Zeppenfeld, M. Büchel, R. David, G. Comsa, C. Ramseyer, and C. Girardet, Phys. Rev. B **50**, 14667 (1994).
- [96] R. Schuster and S. Völkening (unpublished).
- [97] S. Sinha, *Ordering in Two Dimensions* (Elsevier, New York, 1980).
- [98] E. Moog and M. Webb, Surf. Sci. **148**, 338 (1984).

- [99] K. Kern, R. David, R. Palmer, and G. Comsa, *Appl. Phys. A* **41**, 91 (1986).
- [100] W. D'Amico, J. Bohr, D. Moncton, and D. Gibbs, *Phys. Rev. B* **41**, 4368 (1990).
- [101] B. Poelsema, L. Verheij, and G. Comsa, *Surf. Sci.* **152**, 851 (1985).
- [102] A. Novaco and J. McTague, *Phys. Rev. Lett.* **38**, 1286 (1977).
- [103] L. Bruch and J. Venables, *Surf. Sci.* **148**, 167 (1984).
- [104] S. Sharma, S. O'Shea, and W. Meath, *Phys. Rev. B* **40**, 6356 (1989).
- [105] B. Hall, D. Mills, P. Zeppenfeld, K. Kern, U. Becher, and G. Comsa, *Phys. Rev. B* **40**, 6326 (1989).
- [106] J. Gottlieb, *Phys. Rev. B* **42**, 5377 (1990).
- [107] K. Kern and G. Comsa, in *Advances in Chemical Physics LXXVI*, edited by K. Lawley (John Wiley and Sons Ltd., 1989).
- [108] P. Zeppenfeld, Diploma thesis, Universität Bonn, 1986.
- [109] P. Zepenfeld, Ph.D. thesis, Universität Bonn, 1989.
- [110] K. Kern, P. Zeppenfeld, R. David, R. Palmer, and G. Comsa, *Phys. Rev. Lett.* **57**, 3187 (1986).
- [111] K. Kern, P. Zeppenfeld, R. David, and G. Comsa, *Phys. Rev. Lett.* **59**, 79 (1987).
- [112] L. Landau and E. Lifchitz, *Physique statistique* (MIR, Moscou, 1967).
- [113] C. Leming and G. Pollack, *Phys. Rev. B* **2**, 3323 (1970).
- [114] A. Becker, G. Rosenfeld, B. Poelsema, and G. Comsa, *Phys. Rev. Lett.* **70**, 477 (1993).
- [115] H. Röder, K. Bromann, H. Brune, and K. Kern, *Surf. Sci.* **376**, 13 (1997).
- [116] H. Röder, R. Schuster, H. Brune, and K. Kern, *Phys. Rev. Lett.* **71**, 2086 (1993).
- [117] R. Schwoebel and E. Shipsey, *J. Appl. Phys.* **37**, 3682 (1966).
- [118] G. Ehrlich and F. Hudda, *J. Chem. Phys.* **44**, 1039 (1966).
- [119] R. Schwoebel, *J. Appl. Phys.* **40**, 614 (1969).
- [120] T. Michely, M. Hohage, M. Bott, and G. Comsa, *Phys. Rev. Lett.* **70**, 3943 (1993).

- [121] M. Kalf, G. Comsa, and M. Michely, *Phys. Rev. Lett.* **81**, 1255 (1998).
- [122] P. Feibelmann, *Phys. Rev. Lett.* **81**, 168 (1998).
- [123] P. Gambardella, M. Blanc, K. Kuhnke, and K. Kern (unpublished).
- [124] P. Carcia, A. Meinhald, and A. Suna, *Appl. Phys. Lett.* **47**, 178 (1985).
- [125] W. Zeper, F. Greidanus, P. Carcia, and C. Fincher, *J. Appl. Phys.* **65**, 4971 (1989).
- [126] W. Zeper, H. van Kesteren, B. Jacobs, J. Spruit, and P. Carcia, *J. Appl. Phys.* **70**, 2264 (1991).
- [127] N. McGee, M. Johnson, J. de Vries, and J. aan de Stegge, *J. Appl. Phys.* **73**, 3418 (1993).
- [128] A. Atrei, U. Bardi, M. Galeotti, G. Roviida, M. Torrini, and E. Zanazzi, *Surf. Sci.* **339**, 323 (1995).
- [129] P. Grütter and U. Dürig, *Phys. Rev. B* **49**, 2021 (1994).
- [130] H. Brune, private communication.
- [131] T. Kingetsu, *J. Appl. Phys.* **76**, 4267 (1994).
- [132] A. Miedema, *Z. Metallkde* **69**, 287 (1978), and references therein.
- [133] M. Methfessel, D. Hennig, and M. Scheffler, *Phys. Rev. B* **46**, 4816 (1992).
- [134] H. Schief, V. Marsico, and K. Kern, *Rev. Sci. Instrum.* **67**, 2026 (1996).
- [135] M. Blanc, Diploma thesis, EPFL, 1995.
- [136] E. Hecht, *Optics* (Addison-Wesley, Reading, Massachusetts, 1987).
- [137] A. Sandy, S. Mochrie, D. Zehner, G. Grübel, K. Huang, and D. Gibbs, *Phys. Rev. Lett.* **68**, 2192 (1992).
- [138] V. Pouthier, C. Ramseyer, and C. Girardet, *Surf. Sci.* **382**, 349 (1997).
- [139] V. Pouthier, C. Ramseyer, and C. Girardet, submitted.
- [140] A. Lock, J. Toennies, and G. Witte, *J. El. Spectr. Rel. Phen.* **54**, 309 (1990).

Curriculum Vitae

Nom: **Martial Blanc**
Adresse: Av. Pierre de Savoie 48
CH-1400 Yverdon-les-Bains
Date de naissance: 27 août 1971
Nationalité: Suisse (Origine: Brenles/VD)

Formation

1978-1987 Scolarité obligatoire à Yverdon-les-Bains.
1987-1990 Gymnase du Belvédère à Lausanne,
en section latin-grec-mathématiques.
1990-1995 Ecole Polytechnique Fédérale de Lausanne en section physique.
1995-1998 Thèse à l'Institut de Physique Expérimentale de l'EPFL.

Diplômes

1990 Maturité fédérale Type A
mars 1995 Diplôme d'ingénieur physicien EPF

Acknowledgements-Remerciements

J'aimerais en premier lieu remercier le Professeur Klaus Kern, pour m'avoir donné la possibilité d'effectuer ce travail dans son groupe et m'avoir dirigé au cours de cette thèse.

J'aimerais ensuite remercier tous ceux qui ont pris part à ce projet et en particulier Vittorio Marsico, mon moniteur sur cette "manip" compliquée, dont les idées furent foisonnantes bien que parfois entachées d'un soupçon d'utopie. Merci aussi à Klaus Kuhnke pour son support théorique durant cette thèse, ainsi que pour les corrections de ce manuscrit, qui ont nécessité beaucoup d'acharnement de sa part. Merci encore à mes camarades de laboratoire Pietro Gambardella et Samuel Sarbach, à qui je souhaite plein succès pour la suite.

Merci à M. V. Pouthier, au Dr C. Ramseyer et au Prof. C. Girardet, du Laboratoire de Physique Moléculaire de l'Université de Franche-Comté à Besançon, pour la fructueuse collaboration qui a permis de donner naissance au chapitre 6 de cette thèse.

Je tiens à remercier Max Epple et Gork-Bjørn Fischer, mes collègues de bureau durant une bonne partie de cette thèse, qui ont contribué à instaurer une bonne ambiance dans notre bureau. Un merci spécial à Max pour ses cours d'allemand accélérés.

Merci à tous les doctorants, postdocs et autres pour leur camaraderie et les discussions enrichissantes que nous avons eues.

Finalement, un grand merci à toute l'équipe du secrétariat de l'atelier mécanique et d'électronique de l'Institut de Physique Expérimentale, pour leur grand soutien et leur disponibilité tout au long de ce travail.